Structural relaxation processes in pure amorphous silicon

Leonardus Bimo Bayu Aji

A thesis submitted for the degree of

Doctor of Philosophy
The Australian National University

August 2014

Australian
National
University

Declaration

This thesis is an account of research undertaken between March 2010 and May 2014 at the Department of Electronic Materials Engineering, Research School of Physics and Engineering, College of Physical and Mathematical Sciences, The Australian National University, Canberra, Australia.

Except where acknowledged in the customary manner, the material presented in this thesis is, to the best of my knowledge, original and has not been submitted in whole or part for a degree in any university.

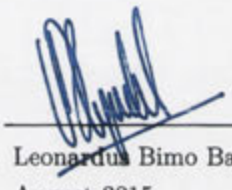

Leonardus Bimo Bayu Aji
August 2015

Acknowledgements

The time spent in writing a doctoral thesis provides a rather unique opportunity to look back and gain a new perspective on several years of work. In doing so, I feel the need to thank the many people that have contributed in different ways to the realization of this work.

I wish to express my sincerest gratitude to Dr. Jodie E. Bradby and Prof. Jim S. Williams, for generously providing scientific feedback on the research, while still permitting me to continuously improve my skills and allowing the progressive development of my autonomy. I also thank them for their persistent support, and for being gifted with a firm enthusiasm and a solid optimism which really helped to transform even the hard work into an enjoyable experience. I am really indebted for being given an invaluable contribution to this work and, even more, to my formation as a young researcher.

It is a pleasure to work with Dr. Bianca Haberl. I thank her for her outstanding ability to suggest, and provide useful inputs for the possible directions in this research work. I am grateful for having her closely following my research, thus allowing me to benefit from her very extensive experience and knowledge. I thank Dr. Simon Ruffell, who had been exceedingly generous in sharing his time in plenty to stimulate scientific discussions during my first frustrating year as a student.

This research is also not possible without many sources of practical and technical assistance and so I would like to express my sincerest gratitude to Dr. Brett Johnson from the University of Melbourne. Dr. Kidane Belay, who has always been exceedingly generous in sharing his time in plenty on ion beam discussions, and whose experimental support has been always at hand. Dr. Helmut Karl from the Universität of Augsburg, Germany for the use of secondary ion mass spectroscopy (SIMS). Alana Treasure from the University of Canberra for the use of Raman system. The indentation group for making it such an enjoyable group to conduct research in.

I wish to spend also a few words on the colleagues who have shared with me the PhD experience. I thank Lachlan Smillie who offered me very detailed and useful comments, suggestions, and corrections on the thesis and Wenjie Yang for carefully proofreading my English. Sherman Wong for the lithography process. Many thanks to Thomas Bierschenk, Keng Chan, Hao-Feng Lu, Vincent Supratman, Ian Yesaya Wenas, Clara Teniswood, Thien Tuan Tran and Xiao Fu for their friendship and for helping me in times of trouble.

I wish this to be an occasion to thank my family. Among the many reasons that I could choose to motivate my gratitude, I would like to mention their everlasting support throughout the years.

Last but not least, I thank Yusia. You have been at my side and believed in me during these years, and your enduring love is a privilege that I really hope to deserve. This thesis is dedicated to you because I regard every achievement in our lives as a success of the two of us.

Abstract

Amorphous solids, particularly amorphous silicon (a-Si), have become the material of choice for a wide range of technological applications from photovoltaics to fiber optics. Taking into consideration that a-Si is also an excellent model of a covalently bonded continuous random network (CRN), this material has been a very active topic of investigation for several decades, frequently crossing the border between physics and materials science. A fundamental understanding of its structure and properties is a prerequisite to improve the utilization of a-Si for the technological use, and may also aid the understanding of many other disordered materials.

Studies of a-Si indicate that the structure and properties of a-Si are critically dependent on the method of formation and thermal history. There are three main formation methods; condensation from vapor, quenching from a melt, and solid state amorphization. Amorphous silicon prepared by a solid state amorphization, such as ion implantation and indentation, results in a pure, uniform and voidless structure, whereas vapor deposition and rapid quenching are found to result in less homogeneous structures which can contain voids, nanocrystals, and impurities. The presence of these microstructures may significantly alter the properties of a-Si. Therefore, only a-Si prepared by solid state amorphization can be considered as an *ideal* amorphous material for the study of its structural properties.

When ion-implanted a-Si is thermally annealed, the structure evolves towards a lower energy states through a reduction in the bond-angle distortion and defect removal. The covalent network after annealing is relaxed. This process is known as structural relaxation or short-range ordering. There are three current models to explain the mechanism of structural relaxation process. One model interprets the structural relaxation as being caused predominantly by the rearrangement of Si bonds, as reflected by a reduction in the bond-angle distortion. This can occur with minimum contributions of, or completely without defect removal. A second model interprets the structural relaxation process as a defect removal process accompanied by a reduction in the bond-angle distortion. Alternatively, a third model, treats the structural relaxation process as a dissolution of paracrystals. Notwithstanding many years of research and widely accessible experimental techniques, the structural properties of ion-implanted a-Si and its relaxation mechanism remain poorly understood and are indeed the subject of lively debate.

The focus of many existing studies on the structural relaxation of a-Si has been on two

distinct states, as-prepared or as-implanted (unrelaxed) a-Si and fully relaxed a-Si, rather than the structural relaxation process itself. This thesis addresses this issue by looking at the transition from unrelaxed to fully relaxed state which may provide insight into the nature of the structural relaxation process.

In this present study, the thermally-induced behavior of three forms of a-Si (ion-implanted, pressure-induced, and re-irradiated fully relaxed a-Si) from as-prepared to relaxed states are studied using various techniques. Raman spectroscopy is used to characterize a-Si as it is sensitive to fluctuation in the vibrational density of states of an amorphous structure. Other techniques, such as indentation, electrical conductivity, and calorimetry are also employed. All these techniques have proven to be useful characterization probes of defects in such an amorphous structure.

Analysis of Raman spectra from all three forms of a-Si show a local (bond-angle) ordering of the structure with thermal annealing approaching a continuous random network (as close as experimentally possible) in the fully relaxed structure. In contrast to some previously reported studies, the bond-angle reduction only changes slightly at the early stages of annealing, and it begins to change significantly at temperatures above 250°C.

Indentation tests show that the deformation mechanism of ion-implanted a-Si is extremely sensitive to the state (relaxed or unrelaxed) of the network. Under certain indentation conditions, unrelaxed a-Si deforms plastically but relaxed a-Si undergoes a pressure-induced phase transformation. These two different deformation mechanisms are related to the presence of defects in the structure. Thermal annealing reduces the defect concentration in the network through defect interactions, and results in the formation of a more rigid (fourfold-coordinated, covalently-bonded) network. This increases the ability of the network to inhibit plastic flow under an applied stress, and thus promotes phase transformation. The transition of the deformation mechanism from plastic to phase transformation occurs at the annealing temperature before the bond-angle distortion reaches its minimum value.

Both Raman spectra analysis and indentation test show that the presence of structural impurities, i.e., in-diffused hydrogen upon annealing, does not contribute significantly to the local (bond-angle) ordering of the structure and the deformation mechanisms of ion-implanted a-Si.

Electrical conductivity measurements of ion-implanted a-Si show that the number of dangling bonds decreases with temperature. This phenomenon is observed in an annealing interval from 25 to 250°C, before the bond-angle ordering begins and just before the transition of the deformation mechanism occurs.

Evidence of thermally-induced short-range ordering is also observed in differential scanning calorimetry measurements. These measurements show heat releases during low temperature annealing, that is predominately due to defect annealing from the structure, and also heat releases due to rearrangement of the the network during high temperature annealing.

Finally, the results from all studies, Raman spectroscopy, indentation, electrical measurements and calorimetry, are brought together to develop a new model for structural relaxation in ion-implanted a-Si. Broadly, it is found that there are two main steps in structural relaxation: defect (dangling bond) removal as a dominant mechanism at low temperatures up to 250°C, which is accompanied by significant heat release, and a reduction in bond-angle distortion at higher temperatures, where the amount of heat release is smaller. In terms of existing models, the current findings are consistent with elements of the previous defect/lattice strain models but differ in that a more distinct separation of defect removal and reduction in strain (bond-angle distortion) is found in the present study. There is no evidence in the current study to support the paracrystalline model.

Publications

1. **L. B. Bayu Aji**, S. Ruffell, B. Haberl, J. E. Bradby, and J. S. Williams. Correlation of indentation-induced phase transformations with the degree of relaxation of ion-implanted amorphous silicon. J. Mater. Res. **28**, 1056-1060 (2013).
2. B. Haberl, **L. B. Bayu Aji**, J. S. Williams, and J. E. Bradby. The indentation hardness of silicon measured by instrumented indentation: What does it mean?. J. Mater. Res. **27**, 3066-3072 (2012).

Manuscript:

1. **L. B. Bayu Aji**, B. Haberl, S. Wong, J. S. Williams, and J. E. Bradby. Evidence for a two-step process in the structural relaxation of amorphous silicon. *to be submitted to* Physical Review Letters.
2. S. Wong, B. Haberl, **L. B. Bayu Aji**, J. S. Williams, and J. E. Bradby. Formation of Si-III/XII regions for device application. *to be submitted to* Applied Physics Letters.
3. **L. B. Bayu Aji**, B. Haberl, T. Li, J. S. Williams, and J. E. Bradby. A framework for the influence of nanostructure and impurities on the phase-change behavior of amorphous silicon. *to be submitted to* Journal of Applied Physics.
4. **L. B. Bayu Aji**, B. C. Johnson, B. Haberl, J. S. Williams, and J. E. Bradby. Structural disorder of amorphous silicon formed by various methods. *to be submitted to* Journal of Materials Research.

Contents

List of Figures

List of Tables

1 Introduction

1.1 Background

Amorphous materials are an important class of materials used for wide range of applications from art to optoelectronics [1]. Glasses are an example of an amorphous material. Since the Roman empire, glass has been used for its decorative qualities, such as stained windows, jewellery, and sculpture [1–3], and much later served as the enclosure for vacuum and cathode-ray tubes, and fiber optics.

In the present day, amorphous materials are also used in data-storage technology [4], and coating for drill bits, artificial heart valves and razor blades [5,6]. Amorphous silicon in its hydrogenated form (a-Si:H) played a key role in the further development of transistors [7] and in photovoltaic energy conversion [8].

The use of amorphous materials by our technological society has been increasing for some time. Over the last few decades, there has been a dramatic improvement in the production capability of amorphous materials. This has led to lower manufacturing costs and increased scientific and technological interest on this important class of solids.

In order to describe the characteristic properties of amorphous covalent solids, Zachariasen [9] proposed the continuous random network (CRN) model for glasses. In this model, the atomic arrangement is characterized by an extended three dimensional network that lacks of symmetry and periodicity. Thus, the principal difference between a crystal network and a glass (amorphous) network is the lack of long-range order characteristic of a crystal in an amorphous network. However, due to the nature of the chemical bonding covalent amorphous networks typically maintains some short-range order at the atomic

length scale [10,11]. Therefore, the theoretical approach to describe amorphous networks emphasizes on the local chemical bonding of the atoms, known as short-range order, rather than on the long-range order that is commonly used to describe a crystalline materials.

The structure of amorphous silicon (a-Si) has attracted particular interest as it is considered to be an ideal model of amorphous tetrahedrally bonded materials [12–16]. Therefore, understanding the properties of a-Si may offer insight into the fundamental properties of many other types of covalent disordered materials.

The structure of a-Si has been understood in terms of two main models: that of a CRN and the more recent paracrystalline model. These two models of a-Si will now be discussed below in some details.

1.1.1 Continuous random network model

Amorphous silicon was first described as a CRN over 40 years ago by Polk in 1971 [12]. This model, as shown in Fig. 1.1, was constructed from tetrahedral units consisting of a small, central atom with a coordination number of four. This model aims to explain only *ideal* a-Si, i.e. with no hydrogen or other impurities. The density of this model, as constructed, was found to be 5% less than the crystal. This was calculated by measuring the distance of three six member in the *boat* configuration and comparing it with a crystalline array with the same mean neighbor distance. The calculated density agrees well with the electron diffraction data obtained in 1969 by Moss and Graczyk [17]. Furthermore, the structure on the short-range scale also correlates well with the electron diffraction experimental data [18,19].

However, Polk's model does not necessarily apply to all a-Si networks. Indeed, a high-energy x-ray diffraction studies of ion-implanted a-Si by Laaziri *et al.* [15] shows that as-implanted a-Si has a coordination number less than four. This result suggests that a-Si in the as-prepared state is not fully coordinated, and could be better described as a *defective* CRN.

The structure and properties of a-Si are dependent on the preparation conditions. Amorphous silicon prepared by the vacuum deposition technique, for example, differs from that obtained by ion implantation. Amorphous silicon produced by ion implantation results in a uniform, pure (without impurities), and voidless amorphous network, whereas a-Si formed by deposition is less uniform and contains voids [20], because the latter evolves from numerous nucleation sites. The properties of a-Si depend not only on the preparation conditions, but also on so-called thermal history. For example, when a-Si formed by ion implantation is thermally annealed, the Si-Si network undergoes structural relaxation or short-range ordering to a form that is closer to an ideal CRN [14,21]. Structural relaxation or short-range ordering process in a-Si has been reported by many authors [14,15,21–26], and this will now be reviewed.

The phenomena of short-range ordering was first observed by Hubler *et al.* [22] in

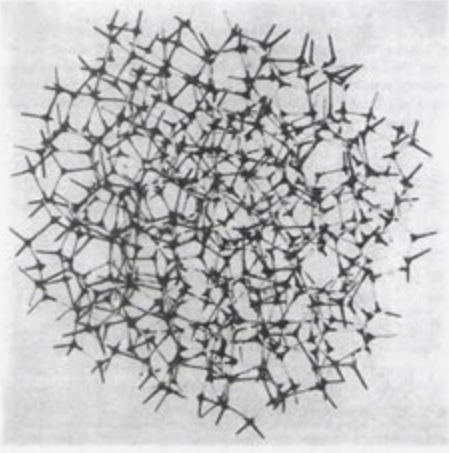

Figure 1.1: Photograph of a continuous random network model using actual *balls* and *sticks* constructed by Polk [12].

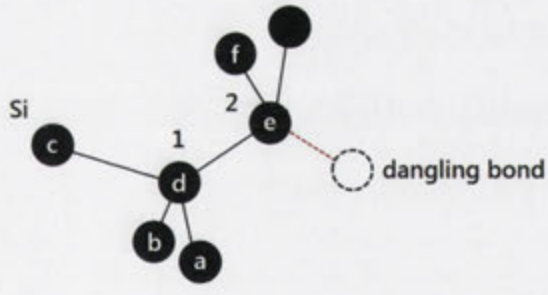

Figure 1.2: Schematic of two tetrahedra with a common bond. The second tetrahedron has a missing silicon atom, thus creating a dangling bond. The bond-angle, is defined by the angle made by atoms labeled: a-d-b; and the dihedral-angle: c-d-e-f

non-hydrogenated a-Si using infrared dielectric property measurements. In that study, the sample's infrared properties were characterized by measuring the intensity of light, reflected from or transmitted through the sample. The authors observed a reduction in the refractive index from 1.12 to 1.08 and band absorption from 5 to 1 after annealing the sample at 500°C for 2 hours. The reduction in the refractive index and band absorption was suggested to be caused by a re-ordering of the amorphous structure to a CRN which reduces the average polarizability per bond [27,28].

In addition to infrared indices of refraction, annealing-induced relaxation also affects other optical properties, such as the width of the Raman transverse optical band. Raman spectroscopy analysis of different forms of a-Si prepared by both chemical vapor deposition and ion implantation show a narrowing in the width of the Raman transverse optical band upon annealing [14,23–26]. The narrowing in the width of the Raman transverse optical band is suggested to be related to the change of the optical constant (refractive index and band absorption) in the previous infrared reflection studies [22,27,28].

A correlation function between pairs of atoms, and the radial distribution function (RDF), obtained from a diffraction study of ion-implanted a-Si also showed that upon annealing at 600°C the coordination number of a-Si increases from 3.79 to 3.88 [15]. This also provides additional support for the interpretation that a-Si in the as-prepared state is a *defective* CRN.

Evidence of thermally-induced structural relaxation in ion-implanted a-Si was also observed in a differential scanning calorimetry (DSC) measurement by Donovan *et al.* [29]. The authors measured a total heat release of 11.9 kJ mol^{-1} during heating from 530 to 720°C (40 K min^{-1}). This heat was due to crystallization. Roorda *et al.* [21], using the same technique, also observed that a-Si releases a considerable amount of heat upon crystallization. However, in addition to the heat of crystallization of 11.7 kJ mol^{-1}, the authors also found a low-temperature (at temperatures below crystallization) heat release of 3.7 kJ mol^{-1}. This heat release was consistently observed at temperatures below the crystallization threshold. Since this low-temperature heat release is related to the narrowing of the transverse optical width, Roorda *et al.* [21] attributed this effect to short-range ordering. In response to this result, Donovan *et al.* [30] repeated their earlier DSC measurement in order to investigate the low-temperature heat release previously observed by Roorda *et al.* [21] in their DSC measurement. In addition to the new proposed value of the heat of crystallization of 13.4 kJ mol^{-1}, Donovan *et al.* reported a slightly higher low-temperature heat release of 5.1 kJ mol^{-1}. This low-temperature heat release is the most direct and strong evidence for the model that a-Si undergoes structural changes below the crystallization threshold temperature.

Regardless of preparation conditions [14,15,21–26,30], it is clear that a-Si in the as-prepared state is a *defective* CRN and approaches a CRN through short-range ordering upon annealing.

Due to the lack of techniques available to quantify order on the medium-range (1 to 4

nm) scale (MRO), most of the early structural and properties studies of a-Si were focused solely on the short-range scale. This raises a question whether MRO also exists in a-Si. In covalent amorphous solids, MRO is defined by the connection of tetrahedral units in the network [31]. This type of connection is specified by the dihedral-angle, as indicated by c-d-e-f in Fig 1.2.

Today, the refinement of microscopy analysis techniques allowing several types of characteristic structural ordering, including MRO, to be identified and their origins elucidated.

1.1.2 Paracrystalline model

Fluctuation electron microscopy (FEM) has been commonly used to study the existence of MRO in amorphous tetrahedrally bonded materials [16, 32–38]. This technique measures the variance in the diffracted intensity normalized with respect to the average intensity, in contrast to traditional measurements by diffraction techniques. It has been mathematically proven that FEM is sensitive to the three- and four-body correlation functions [39, 40].

Gibson et al. [32], using FEM, observed a reduction in medium-range order of deposited amorphous germanium (a-Ge) upon annealing at 350°C for 15 min. The short-range ordering toward a CRN was assumed to coincide with an increase in medium-range order, although there was no experimental data to support this idea. Thus, the result obtained by Gibson *et al.* [32] suggests that the opposite has occurred; the high degree of MRO observed in as-deposited a-Ge is not consistent with the CRN model and a granular structure was instead proposed for this state.

In order to account for the high degree of MRO observed in such amorphous solids, the *paracrystalline* model [41] was proposed. This model attempts to explain the origin of disordered structure in low temperature vacuum-deposited amorphous semiconductor materials.

The existence of MRO in amorphous silicon has thus been extensively studied [16, 34–38]. These studies revealed that a-Si in the as-prepared form contains a significant medium-range order on the length scale of 1-2 nm. Cheng *et al.* [35, 42] first described the medium-range order in ion-implanted a-Si. In that study a significant reduction in the MRO was observed upon annealing. On this basis, Cheng *et al.* suggested that as-implanted a-Si is paracrystalline. Therein, the proposed paracrystalline network for ion-implanted a-Si is primarily due to the fact that such a-Si is originated from an anisotropic single crystal, and becomes a randomly oriented fine-grained crystalline material surrounded by a fully amorphous network. The origin of such paracrystals in ion-implanted a-Si was explained according to an energy spike mechanism for ion implantation [43, 44]. This paracrystalline model remains a topic of much debate in the literature [45] as will be explained in more detail in later sections.

In summary, there are two distinct models for ion-implanted a-Si: an imperfect CRN and a paracrystalline network. On annealing, both of these models approach the structure

of an *ideal* CRN. In this thesis, the pure forms of a-Si are studied with focus on the a-Si prepared by ion-implantation. The effect of annealing-induced relaxation on the structure and properties of pure a-Si will now be reviewed and its mechanism of structural relaxation will be introduced in more detail.

1.2 Annealing-induced short-range ordering

It is now widely accepted that the structure of ion-implanted a-Si undergoes an extensive restructuring or relaxation toward the lowest free energy state upon annealing [14]. The covalent network after annealing is relaxed [14]. This process is irreversible and results in modification of the optical [22,27,28], vibrational [23,26,46], mechanical [47], and electrical [48,49] properties of the material. It is also observed that these properties are influenced by the impurity content, such as hydrogen [50,51]. Hydrogen is known to interact with defects, thus reducing the mid-gap dangling bond density in the network, which results in improvement of the electrical (transport) properties of a-Si. Furthermore, removal of dangling bonds from the a-Si matrix can also reduce the Si-Si network strain [51].

The effect of thermal annealing on the properties of ion-implanted a-Si has been extensively studied by Raman spectroscopy, indentation, and electrical conductivity measurements. This will be summarized below.

1.2.1 The local bonding parameters

Tsu *et al.* [23] demonstrated the capability of Raman spectroscopy to distinguish the difference in the spectra of a-Si annealed at different temperatures. A narrowing in the linewidth of the TO band, Γ(TO), a shift in the position of the transverse acoustic band, ω(TA), and optical band, ω(TO), to lower and higher wavenumbers, respectively, and a pronounced increase in the intensity ratio of transverse acoustic to optical band, I(TA)/I(TO) were observed due to annealing.

The increase of ω(TO) and corresponding decrease of ω(TA) with increasing order in the structure is quite fundamental. Since the TO and TA bands in a-Si basically arise from phonons near the zone boundaries, the separation of ω(TO) and ω(TA) is due to the presence of two atoms per unit cell in c-Si. Meek [52] showed that the TO band depends on both the topology and the bond-angle distribution of the network. This bond-angle distribution is affected by bond-stretching motions, which are sensitive to the arrangement of the bonds around each atom. The TA band, on the other hand, depends more directly on the topology of the network and has been linked to the bending modes and thus to the vibration of the entire tetrahedron within the network [53]. Therefore, the relative intensity of TA to TO band can be used as a measure of the structural order on the intermediate-range scale (beyond second neighbors). It is expected that Γ(TO) and I(TA)/I(TO) decrease, while the effect on Γ(TA) is minimal with increasing order.

To further investigate the *degree* of relaxation, Beeman *et al.* [25] proposed a simple experimental method to extract a structural parameter (bond-angle distortion, $\Delta\theta$) from the Raman spectrum. Based on that model, Γ(TO) and $\Delta\theta$ are linearly correlated by an empirical formulae (see section 2.2.3 in the next chapter for details). This is a very useful quantitative measure for the *degree* of relaxation upon annealing [14, 26, 54].

The first structural relaxation study conducted on a pure form (ion-implanted) of a-Si was performed by Fortner *et al.* [54]. Raman spectra indicate that Γ(TO) decreases from 103 to 80 cm^{-1} upon annealing at 550°C. Roorda *et al.* [14] similarly reported a decrease in Γ(TO), which corresponds to a reduction in bond-angle distortion from 11.8 to 8.8° after annealing at 500°C for 45 min. In this latter study, it was also shown that ω(TO) shifted from 470 to 479 cm^{-1}.

Although Raman spectroscopy is a sensitive technique for probing changes in local bonding parameters of a-Si (by monitoring the changes in the bond-angle distortion) due to annealing, this technique is not sensitive to the defect removal process. Therefore, techniques that are more sensitive to the structural defect in a-Si, such as indentation and electrical conductivity, must also be employed.

1.2.2 Mechanical deformation mechanism

Uniaxial point loading (indentation) of c-Si results in a series of phase transformations (pt) during mechanical deformation [55]. During loading, diamond-cubic (dc) Si-I undergoes a phase transformation to a metallic Si-II phase, and further transforms to either polycrystalline phases (Si-III and Si-XII) or a-Si upon unloading [55–57]. The formation to either Si-III/Si-XII or a-Si depends on the unloading rate. Rapid unloading rate results in amorphous phase [58], while slow unloading leads to the formation of polycrystalline phases.

The difference in the deformation pathways is reflected in the indentation mechanical response, also known as the load-depth (P-h) curve, when unloaded with different rates. Changes in the material's density during a phase transition results in a characteristic event in the P-h curve. The formation of Si-III/XII during unloading results in a sudden displacement discontinuity, so-called pop-out, in the unloading segment, whereas the formation of PI a-Si results in an elbow [59]. These characteristic events are shown in Fig. 1.3.

A similar phase transformation pathways was also observed when indenting relaxed ion-implanted a-Si, suggesting that a-Si also phase transformed to a metallic phase on loading. Slow unloading rates lead to the formation of the polycrystalline phases (Si-III and Si-XII) [47] and fast pressure release rates result in amorphous phase [60]. The sequence of phase transformations is summarized in Fig. 1.4. Relaxed a-Si transforms upon loading into a high density metallic (Si-II) phase [61, 62]. Upon pressure release, the metallic Si-II phase transforms to the crystalline Si-XII and Si-III phases under a sufficiently slow

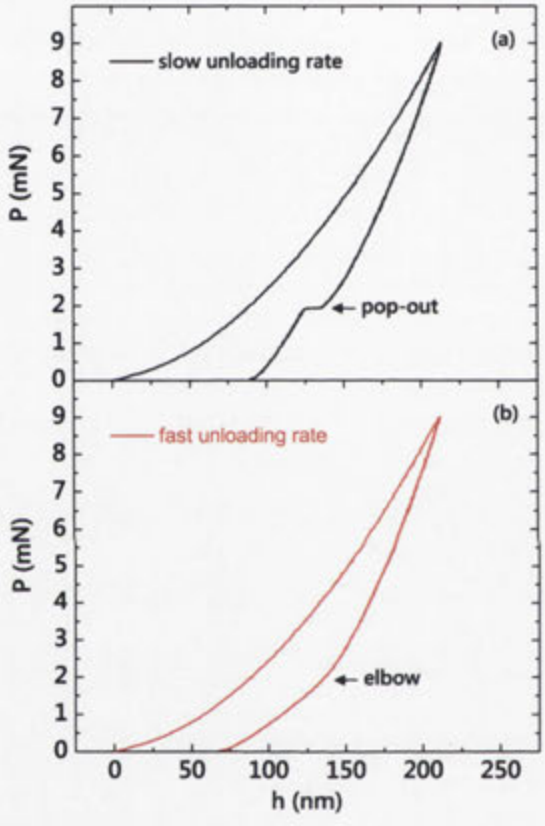

Figure 1.3: Load-depth curves of indentation of c-Si with (a) slow and (b) fast unloading rates. In the case of the slow unloading rate, the formation of Si-III/XII results in a pop-out, while formation of PI a-Si results in an elbow in the case of fast unloading.

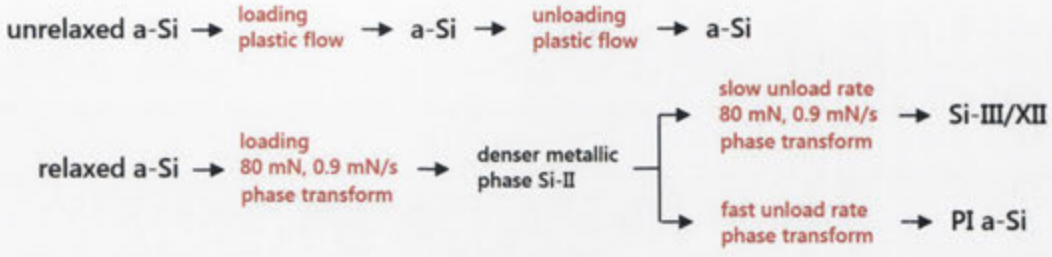

Figure 1.4: Schematic of the indentation-induced phase transformations of unrelaxed and relaxed ion-implanted a-Si.

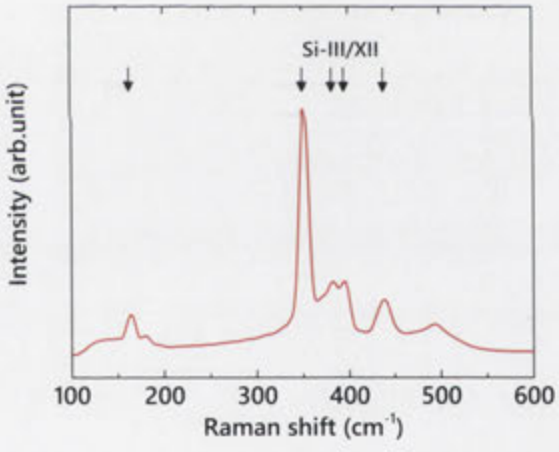

Figure 1.5: Raman spectrum of residual indent in relaxed a-Si after slow unloading rates resulting in the formation of polycrystalline phases Si-III/XII.

unloading rate. On full pressure release, the end phase is a mixture of Si-III and Si-XII. Under a fast unloading rate, on the other hand, the Si-II phase transforms into pressure induced (PI) a-Si.

Examples of Raman spectrum of a residual indents made in relaxed a-Si after slow unloading is shown in Fig. 1.5. The crystalline phases are labeled according to Ref. [63,64].

The absence of Si-III/XII during a fast unloading rate can be explained by crystalline nucleation and growth mechanisms. The transformation of Si-II phase to Si-III and Si-XII phases requires time for the generation of sufficient nucleation sites, allowing the crystallites to grow to a critical volume. It is therefore reasonable that lower unloading rates promotes the nucleation and growth of the crystalline Si-III/XII phases, while faster unloading rates do not allow sufficient nucleation times, with a-Si is the end result [60].

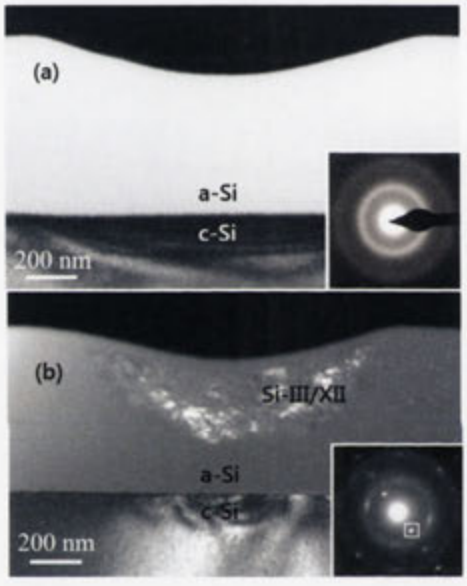

Figure 1.6: (a) A bright field cross-sectional image of a residual indent made in unrelaxed a-Si, and (b) dark field cross-sectional image of a residual indent made in relaxed a-Si as reported by Haberl *et al.* [47] SADPs of the residual indents are shown as insets in both cases.

In contrast to relaxed a-Si, unrelaxed (as-implanted) a-Si deforms solely via plastic flow [47]. Plastic deformation in ion-implanted a-Si is associated with the presence of a high density of defects and broken bonds in the network, which facilitates deformation of the material via plastic flow under stress [47]. Thus, the preferred mode of deformation in a more ordered network is phase transition.

Cross-sectional transmission electron microscopy (XTEM) images of residual indents made in as-implanted and relaxed a-Si are shown in Fig. 1.6 [47]. The image of a residual indent in as-implanted a-Si shows only amorphous material and with no evidence of crystallinity, as shown by the selected area diffraction pattern (SADP) from beneath the residual indent (inset). On the other hand, the image from the residual indent made in

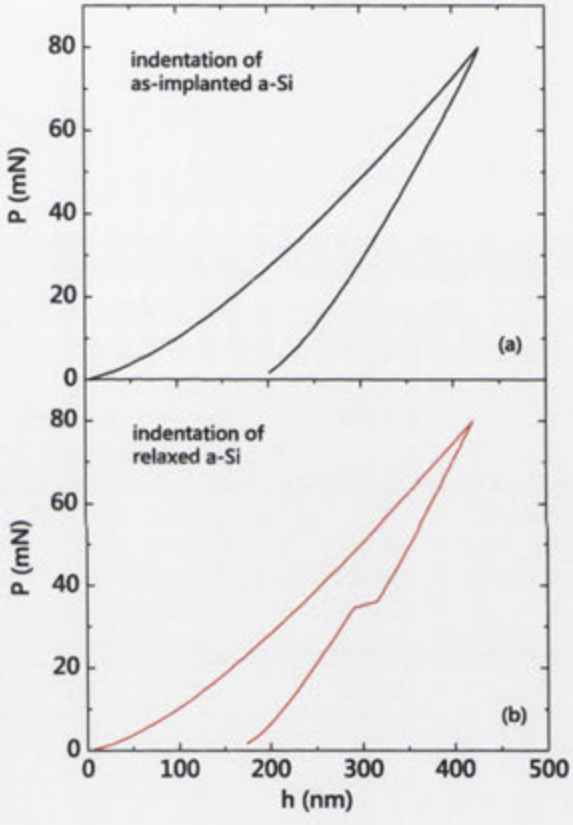

Figure 1.7: Load-depth curves of indentation performed on (a) as-implanted and (b) relaxed a-Si [65].

relaxed a-Si shows clear evidence of crystallinity. Figure 1.6(b) shows a clear indication that relaxed ion-implanted a-Si undergoes a phase transformation under indentation.

The difference in the deformation pathways of the relaxed ion-implanted a-Si, whether it forms the crystalline Si-III/XII phases or an amorphous phase upon pressure release, is also reflected in the load-depth curve. The formation of the Si-III/XII phases is characterized by the appearance of pop-outs in the unloading curve [47]. As shown in Fig. 1.7, only the load-depth curve of the relaxed ion-implanted a-Si exhibits a characteristic event in the unloading part indicating that the material deformed via phase transformation. However, under the same loading and unloading conditions, there is no such event on unloading of as-implanted a-Si. This dramatic and clear difference is indicative of the different states of as-implanted and relaxed a-Si [47,65,66]. This phase transformation behavior can hence be use to probe the *state* of ion-implanted a-Si.

1.2.3 Structural and electrical defects

Amorphous silicon formed by a highly nonequilibrium process (such as ion implantation) is known to contain a high concentration of defects [28,67]. Dangling bonds [28], and vacancy-type defects [67] have both been proposed as such defects in an amorphous network.

Polman *et al.* [68] studied the defect complexes in different structural states of ion-implanted a-Si using the fast diffusing transition metal Cu as a probe. In c-Si impurities can be trapped at defect sites in a process known as gettering [69]. In an amorphous solid the concept of defects is, obviously, more complicated. Since Cu interacts strongly with structural defects in a-Si that act as trapping sites, the density of defects produced in a-Si by ion implantation can be determined by the diffusivity and solubility of Cu in the material. In that study, three types of a-Si were studied: unannealed (as-implanted), fully relaxed (annealed at 500°C for 1 hour), and re-irradiated (of previously relaxed). All samples were further irradiated with Cu ions. The diffusion of Cu in the samples was then studied following thermal annealing at various temperatures ranging from 150 to 270°C for times between 10 min and 104 hours. The Cu concentration profiles were measured using Rutherford backscattering spectrometry (RBS). Assuming that these Cu concentrations are dependent on defect concentrations, the authors reported that the concentration of defects in the annealed a-Si was considerably lower than that in the as-implanted a-Si.

Following Polman *et al.* [68], using the same technique, Coffa *et al.* [70] measured the diffusion and solubility of Pd in a-Si. The as-implanted a-Si was irradiated with Pd ions, before being annealed at 500°C. This annealing process causes the redistribution of the Pd atoms within the a-Si layer, and anneals out a considerable fraction of the defects in the amorphous structure. The diffusion and solubility of Pd in a-Si were studied following re-irradiation of the samples with Si ions with fluences ranging from 1×10^{12} ions cm^{-2} to 5×10^{15} ions cm^{-2}. The samples were then annealed at 250°C for 36 hours to enable the redistribution of the impurity (Pd) atoms. In this case, the amount of trapped impurities

increases with increasing Si fluence. Although the defect density could not be accurately quantified on the sample annealed at various temperatures, this experimental data directly showed that annealing at 500°C reduces the number of trapping sites (and thus density of defects) in a-Si. This result is in full agreement with Polman *et al.* [68].

The number of trapping sites (and thus defect density) in a-Si can also be probed using positron annihilation spectroscopy (PAS) and free carrier lifetime measurements. These measurements are sensitive to vacancy-type defects and dangling bonds in the amorphous structure. Roorda *et al.* [48] conducted PAS and lifetime measurements on unannealed and annealed (at 150°C and 500°C) ion-implanted a-Si samples. The authors reported that the density of vacancy-type defects in the as-implanted a-Si is 1.2 at.%, and it reduces to 0.4 at.% upon annealing at 500°C for 1 hour. It is worth mentioning that these values were obtained by making some necessary assumptions that the positron diffusivity and the trapping rate of vacancy-type defects in a-Si is equal to those in c-Si. Furthermore, concurrent with the removal of vacancy-type defects by annealing, a tenfold increase in the lifetime of the free-carrier was observed, suggesting a significant reduction in the number of dangling bonds.

As previously mentioned, ion-implanted a-Si contains a high concentration of defects. These defects dominate the electronic properties of ion-implanted a-Si by introducing localized electronic defect states in the band gap [71], and thus affecting the electrical conductivity of the material. Since a removal of structural defects occurs upon annealing, the density of localized states is also reduced during the relaxation process [48]. Electrical conductivity measurements therefore provide a relatively simple method to study such defects.

A conductivity study on ultra-high vacuum electron-beam deposited a-Si was carried out by Shin *et al.* [72]. In that study the as-deposited a-Si were unrelaxed by irradiation of Si ions at room temperature. *In situ* conductivity measurements were then performed in a two-point probe configuration by applying a voltage to the sample while being annealed at various temperature for 15 min. Through combined analysis of both *in situ* and *ex situ* measurements of dynamic changes in the conductivity with annealing, they reported that the density of states of a-Si decreases from 7×10^{20} to 6×10^{19} eV^{-1} cm^{-3} upon annealing at 500°C for 15 min. Assuming that electrically active defects are representative of all defects in the ultra-high vacuum electron-beam deposited a-Si, these values then correspond to the number of defects responsible for structural relaxation.

However, the density of electronic states in a-Si is also strongly dependent on the preparation condition and quality (such as impurity content) of the material, and thus is clearly not a unique property. For example, in another conductivity study by Coffa *et al.* [49], a-Si layers were formed by low pressure chemical vapor deposition technique. The as-deposited a-Si layer was further implanted with Si ions to destroy any pre-existing crystalline nuclei. The samples were then annealed at 540°C for 1 hour. *In situ* conductivity measurements using a two probe configuration were performed during irradiation of Si and

Au ions from -196 to 527°C. The density of states at the Fermi level reduces from 5×10^{20} cm^{-3} eV^{-1} at -196°C to 5×10^{19} cm^{-3} eV^{-1} after annealing at 540°C for 1 hour. It is also observed that the defect reduction at and above room temperature is only a small portion of the phenomenon since most of the defects were already annealed out below room temperature.

Despite the different densities of defects obtained by different techniques and authors, these studies all show significant reduction in structural and electrical defects upon annealing.

1.3 Structural relaxation mechanisms for a-Si

The structure of pure relaxed a-Si is generally considered to be close to a CRN with Si atoms being almost fourfold coordinated and covalently bonded [12]. As discussed earlier, the structure of unrelaxed a-Si and structural relaxation itself is still a matter of some debate. Indeed, both experiments [14, 24, 73–75] and simulations [76, 77] have shown that the bond-angle distortion and the density of defects decrease during relaxation. However, the relative contribution of both effects on the relaxation process remains an object of some controversy.

Stolk *et al.* [75] compared carrier lifetime measurements and Raman analysis of a-Si annealed by furnace and pulsed-laser annealing. The authors reported that there is no unique correlation between defect density and bond-angle distortion in a-Si. Their experiment showed that for samples relaxed to a given intermediate value of bond-angle distortion, the density of defects is critically dependent on how that state has been reached (by furnace or pulsed-laser annealing). For a given value of bond-angle distortion the density of defects can vary by as much as a factor of 3, thus bond-angle distortion is quite independent of the density of defects. This suggested that the structural relaxation in a-Si could occur without defect removal. In their model, defects thus play a secondary role only for structural relaxation. This conclusion is further reinforced by Roura *et al.* [78], who quantified the strain energy stored in a-Si by reanalyzing the excellent calorimetry experiments carried out by Roorda *et al.* [14]. This results in the conclusion that in ion-implanted a-Si, the observed heat releases during relaxation is mainly due to the rearrangement of Si bonds, while the contribution of defect removal is smaller.

Despite the small contribution from defect removal in the relaxation process, this does not imply that defects play a secondary role in the relaxation kinetics. Presumably, as thought by Stolk *et al.* [75] the rearrangement of Si bonds to lower strain energy is mediated by a defect diffusion and removal process.

Roorda *et al.* [14], on the other hand, compared the DSC data obtained from the defect annihilation process in ion-bombarded c-Si, with identically treated relaxed a-Si. It appeared that both the kinetics and the temperature dependence of annealing of ion-bombarded relaxed a-Si cannot be distinguished from those of defect annealing in ion-

bombarded c-Si. This suggests a similarity in the physical processes that induces structural relaxation in a-Si and defect removal in c-Si. Since it is well accepted that structural relaxation of a-Si involves a reduction of the bond-angle strain [14, 25, 74, 76], thus their suggestion that defects control the structural relaxation would contradict the initial interpretation of structural relaxation [23]. It is noted, however, that Si atoms surrounding a defect have to change their position slightly to accommodate changes in the bond-angle distortion [79]. Therefore, Roorda *et al.* [21] attributed the observed heat release from the calorimetry experiments to a change in the structure (and thus reduction in the bond-angle distortion) around the collapsing defects in the network. Thus structural relaxation is a process, where defect removal is accompanied by a reduction in the bond-angle distortion.

In order to distinguish between the rearrangement of Si bonds and defect removal process in structural relaxation, Volkert [80] measured the density changes in ion-implanted a-Si during heating using wafer curvature measurements. These measurements were performed from -175 to 500°C. It was reported that during heating to 250°C, the density of the a-Si decreased by $\geqslant 0.3\%$, and then increased with further increase of temperature. This suggest that there are two different relaxation regimes. Volkert proposed that both regimes are due to defect interactions, such as broken bonds, in the network.

Further support for the defect-driven model of structural relaxation was obtained from high-energy x-ray diffraction by Laaziri *et al.* [15]. In that study, the authors performed Fourier transform analysis of the diffraction pattern, a correlation function between pairs of atoms, and the radial distribution function (RDF) of as-implanted and relaxed samples to extract their coordination number. Upon annealing at 600°C, the authors observed an increase in the coordination number from 3.79 to 3.88. The increase in coordination number was attributed to the reduction in the defect density in the amorphous structure. However, it previously has been reported that the density of a-Si remains constant upon annealing at 580°C [81]. The authors then suggested that the defect density in the a-Si is dominated by vacancy and interstitial type of defects. Hence, recombination of an equal numbers of these defects results in a constant density.

Urli *et al.* [82] applied tight-binding molecular-dynamics simulation in order to understand the increase in the coordination number during structural relaxation without affecting the density. The authors suggested that structural relaxation is facilitated by recombination of dangling bonds in the amorphous structure. Hence, an increase in the coordination number is not followed by densification. This result is in full agreement with Laaziri *et al.* [15].

Alternatively, as outlined at the start of this chapter, the pure as-implanted (unrelaxed) a-Si has also been described as paracrystalline. As detailed in section 1.1, medium-range order was observed to reduce dramatically on thermal annealing, and hence the removal of paracrystals was proposed as part of the mechanism behind relaxation [42]. Therefore, Cheng *et al.* [83] proposed that structural relaxation consists of two phases: in the first phase, short-range ordering (i.e. collapsing of defects) is takes place at low temperature.

Secondly, medium-range disordering taking place (i.e. the paracrystals collapse into a CRN), and the short-range ordering is completed. This model is somewhat controversial [45]. For example, a measurable difference in MRO is only observable at a temperature above 450°C [42]. In contrast, structural relaxation as measured by calorimetry can be observed at temperatures as low as -150°C [84]. It was also observed that the reduction in MRO persisted for 5 hours [42], during which time no measurable heat release from the samples were observed in the calorimetry experiment performed by Roorda *et al.* [21].

In addition, Cheng *et al.* [35,83] also reported a depth dependence (between the surface and deep region) of the medium-range order in the as-implanted state. This raises the possibility that the surface of the specific material in that study was not fully amorphized; it might have consisted of a pre-amorphous highly defected state, rather than the form of a-Si referred to as-implanted a-Si in most other studies. Interestingly, Cheng *et al.* [83] identified the deep region in the as-implanted sample as a highly defective CRN rather than paracrystalline, however the effect of annealing on this deep region was not investigated.

In summary, on the basis of CRN and paracrystalline understanding of a-Si, there are three models of structural relaxation mechanisms for ion-implanted a-Si. The first model interpreted the structural relaxation as being caused predominantly by the rearrangement of Si bonds, as reflected by a reduction in the bond-angle distortion, which can occur with minimum contributions of, or completely without defect removal. The second model interpreted the structural relaxation process as a defect removal process accompanied by a reduction in the bond-angle distortion, and the third model interpreted the structural relaxation process as a dissolution of paracrystals.

1.4 Motivation of this study

As outlined above, pure relaxed ion-implanted a-Si is the best representation of a covalently bonded CRN that can offer insights into the fundamental properties of many types of other disordered materials. Most of the existing studies on ion-implanted a-Si considered the unrelaxed (i.e. as-prepared or as-implanted) and fully relaxed (as close as experimentally possible to CRN) states rather than the structural relaxation process itself which may provide insight into the driving mechanisms for relaxation. This thesis uses the variation in the physical properties, deformation mechanism, electrical conductivity, and heat release over a range of relaxation states to address the driving mechanism in the structural relaxation process.

For this thesis, a-Si prepared by ion implantation is mainly studied, since this form of a-Si is known to be pure, uniform and voidless [20]. The density measurements of ion-implanted a-Si show that the density remains slightly unchanged (or decreases very slightly) after annealing to temperatures up to 580°C [80–82]. This indicates that the change in the structural properties of this form of a-Si are intrinsic to the amorphous network and different from what has been observed for deposited films [13, 85, 86]. Thus,

ion-implanted a-Si, whose properties are not likely to be influenced by structural irregularities, is an *ideal* form of amorphous material for studying the effect of annealing on its properties.

Hydrogen, introduced in a-Si by thermal diffusion, is known to reduce the Si-Si network strain. Thus, the effect of in-diffused hydrogen on the structural relaxation mechanism is investigated in depth.

1.5 Thesis structure

This thesis has the following structure. Note that the implications of the results for the broader understanding of structural relaxation of a-Si will not be discussed in depth at the end of each respective chapter. Instead all the significant results will be collated and discussed in the form of a proposed extended model of structural relaxation process in the concluding chapter (Chapter 6).

- In chapter 2, the details of the sample preparation and characterization techniques and experimental setup employed together with their underlying theories are described in detail.
- In chapter 3, local (short-range) ordering of ion-implanted, pressure-induced, and re-irradiated a-Si induced by thermal annealing is presented. The influence of in-diffused hydrogen during annealing will also be discussed. The influence of in-diffused hydrogen is investigated for a-Si formed by ion implantation only.
- In chapter 4, the mechanical behavior of ion-implanted a-Si, in terms of the ability to deform via phase transformation by spherical indentation, is presented. The effect of loading/unloading rates and in-diffused hydrogen on the ability of the a-Si to phase transform is also described.
- In chapter 5, quantification of localized electronic defect states in ion-implanted a-Si at different relaxation states, as investigated by electrical conductivity is presented.
- In chapter 6, the key results are discussed in detail. The information on the structural properties gained from the variety of techniques in conjunction with results from calorimetry is used to propose an extended model of structural relaxation process in a-Si.
- In Chapter 7, concluding remarks and some proposed future experiments are given.

2

Sample preparation and characterization techniques

This chapter discusses the experimental setup and sample preparation techniques used in this thesis. All samples were prepared from a Czochralski-grown p-doped Si (100) wafer with a resistivity of 10-20 Ω-cm, and 100 nm and 2.4 μm thick p-type silicon on insulator (SOI) wafer with a resistivity of 8.5-11.5 Ω-cm.

2.1 Sample preparation

2.1.1 Ion implantation technique

Ion implantation is a technique generally used to modify the properties of a solid by embedding atoms into a substrate in the form of ionized particles. Ion implantation was initially developed in the late 1970s as a fabrication method of bipolar transistors in Si integrated circuits [87, 88]. Moreover, ion implantation was also used for producing the p-n junction of photovoltaic devices [89]. Since then, ion implantation has been used for great variety of purposes, from industrial application such as doping of semiconductors to fundamental studies of materials, such as ion irradiation-induced amorphization in Si.

As illustrated in Fig. 2.1, the implanted ion undergoes collisions with the target atoms [90]. During each collision, the ion loses its energy through inelastic (electronic) interaction between the ion and lattice electrons, and elastic (nuclear) collision between the ion and nuclei in the solid [91] until it finally comes to rest within the solid. The elec-

tronic collisions lead to the excitation or ionization of both target atoms and incoming ions, while nuclear collisions produce phonons or displaced target atoms, among other defects such as vacancies and interstitials [92]. The accumulation of defects produced during collision cascades can eventually leads to amorphization of a crystalline solid. However, during the accumulation of these defects, dynamic annealing such as recombination of vacancies and interstitials can occur due to their high mobility at and above room temperature. Therefore it can affects the crystalline-amorphous transition. Previous studies [93–95] on the temperature dependence of the crystalline-amorphous transition have shown that the occurrence of dynamic annealing can be suppressed by performing irradiation at liquid nitrogen temperature.

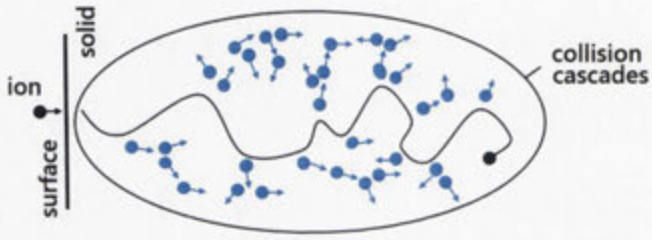

Figure 2.1: Schematic of a collision cascade caused by ion irradiation. The thick line illustrates the position of the surface, and thinner lines illustrate the ballistic collision path of the ion from beginning until it stops within the solid.

The accumulation of defects produced during irradiation is highly dependent on parameters such as temperature [93–95], ion species [97], energy [98] and fluence [99]. The distribution of these defects can be simulated using SRIM (Stopping and Range of Ions in Matter), a Monte Carlo simulation program developed by J. F. Ziegler and co-workers that is capable of performing detailed numerical calculations for individual ion-substrate interactions [100].

A basic ion implantation system consists of: an ion source to produce an ion beam, an acceleration stage known as a source bias and an Einzel lens to attain the desired energy and focus the beam, respectively, magnets to steer and filter out the desired ion species from other ionized species produced in the ion source and a target chamber [90].

In this study, irradiations were performed at the Australian National University (ANU) using a National Electrostatic Corporation (NEC) 5SDH-4 tandem accelerator (1.7 MV) as shown schematically in Fig. 2.2. A lower energy accelerator (175 kV) was also used for some parts of the work, but will not be discussed here as the principles of operation are in effect the same.

The NEC accelerator uses a SNICS-type (Source of Negative Ions by Cesium Sputtering) source. Negative ions are produced from a solid cathode in which the material to be implanted is packed as a powder into a Cu cathode. Cs vapor from a molten Cs reservoir is incident onto the surface of the ionizer while maintained at a temperature of 1100°C. Cs^+

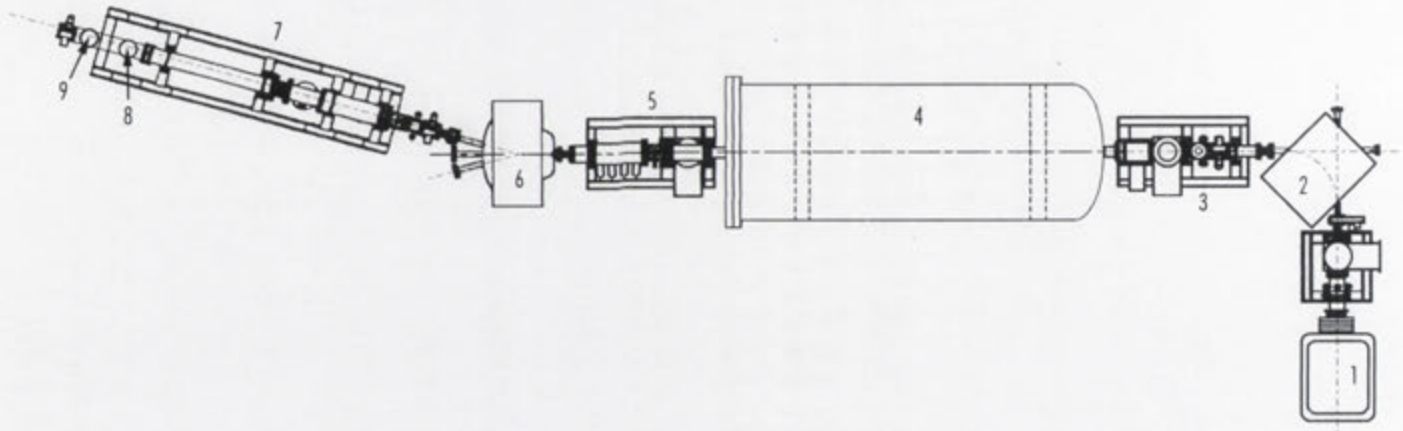

Figure 2.2: Schematic of the NEC 5SDH-4 1.7 MV tandem accelerator located at the Department of Electronic Materials Engineering at the Australian National University [96]: (1) SNICS ion source; (2) mass analyzing magnet; (3) einzel lens and steering; (4) accelerator tank and high voltage terminal; (5) quadrupole lens; (6) energy analyzing magnet; (7) ion beam rastering; (8) beam-defining apertures; and (9) target chamber.

ions are created and accelerated towards the negatively biased cathode. Atoms and ions (both positively and negatively charged) are sputtered from the cathode. Negative ions are accelerated from the cathode, then extracted and focused by an extraction potential of 10 kV and a bias potential of 65 kV.

The accelerated ions pass through the mass analyzing 90° magnet with bending radius R. The magnetic field B can be adjusted to allow the transmission of ions with mass m and charge q according to:

$$B = (2mV_o)^{1/2} R^{-1} (eq)^{-1/2} \tag{2.1}$$

where V_o is the potential of the ions, m is the mass of the ions, q is the ion charge state, and e is the electronic charge. The transmitted ions are then delivered to an Einzel lens and two $x - y$ electrostatic steerers prior injection into the accelerator tank. The accelerator tank consists of numerous equi-potential rings, separated by insulators and resistors which provide a uniform potential gradient along the tank. In the middle of the tank resides a high voltage terminal (1.7 MV maximum), positively charged by four pelletron chains. The negative ions are accelerated to the positively charged terminal and pass through the stripper (N_2) gas thereby lose electrons and and become positively charged. The resulting positive beam is accelerated with a final energy of

$$E_i = e(qV_o + (q + n)V_t) \tag{2.2}$$

where n is the final charge state, and V_t is the terminal voltage.

Following the same principle as the 90° magnet, a 15° analyzing magnet is used to select ions of the desired charge state. A quadrupole lens is used to focus the ion beam onto the target in the target chamber. The beam is rastered in the x, y direction until the desired fluence is achieved. The fluence Q can be calculated by:

$$Q = (Aeq)^{-1} \int_0^t I dt \tag{2.3}$$

where A is the implanted area and I is the beam current. The number of implanted ions is monitored by measuring the integrated current on the target.

A thin layer of carbon paste/tape was used to improve the thermal contact between the sample and the Nickel sample holder, i.e. to ensure that irradiations took place at liquid nitrogen temperature. To minimize contamination, irradiations were carried out under vacuum maintained at or below $\sim 10^{-7}$ Torr.

2.1.2 Thermal processing

Thermal processing consists of heating a wafer to a specified temperature in a variety of environments (such as N_2, Ar, N_2:H_2 forming gas, O_2, N_2O, and NH_2) for a prescribed

length of time in order to alter its properties. This process can repair damage from ion-implantation process, activate dopants, and change the physical state of films [101].

To induce a change in the structure and to activate dopants in a-Si, the present study uses two type of thermal annealing systems: a quartz tube furnace and a rapid thermal annealing system. The rapid thermal annealer (RTA) is used for short annealing times (< 30 min), and a quartz tube furnace for longer annealing times.

To investigate the effect of the two different furnace ramp-rate on the structural changes in the amorphous network, a-Si samples were annealed on both apparatuses at various temperatures for 30 min. The effect of the ramp-rate was examined by comparing the bond-angle distortion (see section 2.2.3 on details for the determination of $\Delta\theta$) obtained from samples annealed in quartz tube furnace with RTA.

T (°C)	Quartz $\Delta\theta$ (deg)	RTA $\Delta\theta$ (deg)
250	10.88±0.12	10.70±0.06
350	10.22±0.06	10.15±0.07
450	9.60±0.09	9.64±0.03
550	9.21±0.04	9.23±0.04

Table 2.1: The comparison of the bond-angle distortion obtained from samples annealed in the RTA and quartz tube furnace for 30 min.

Table 2.1 summarizes the calculated bond-angle distortion for samples annealed at various temperatures on both apparatuses. It is clear that the bond-angle distortion obtained from samples annealed in both apparatuses are equivalent within the uncertainty for each temperature. This suggests that the difference in the ramp-rate did not produce a significant effect on the bond-angle distortion.

2.1.3 Photolithography

Photolithography is a process of transferring a pattern from a photomask to the surface of a wafer using light. The basic photolithography process is illustrated in Fig. 2.3. In the first step, before applying photoresist (also called resist), the wafer is cleaned to remove any contamination, such as organic, ionic and metallic impurities from the surface. A layer of silicon dioxide (SiO_2) is deposited on the surface of the wafer to serve as a barrier layer. Photoresist coating is applied on top of the oxide layer using spin-coating machine. This method produces a uniform layer of coating resist on the wafer surface [102]. The wafer is pre-bake (soft-bake) at temperature of 90 to 100°C for 20 to 30 min to solidify the resist and to evaporate the solvent resist.

On the second step of photolitography, the wafer is exposed to UV light through a photomask. During exposure to UV light, the resist undergoes a chemical reaction and reacts differently depending on the type of the resist [102]. For positive resists, the exposed

resist becomes soluble and readily washed away by the developer, leaving the unexposed resist on the wafer as pattern of resist. Negative resists, on the other hand, have the opposite behavior of positive resists. Due to their capability of finer resolution, positive resists are often chosen over negative resists.

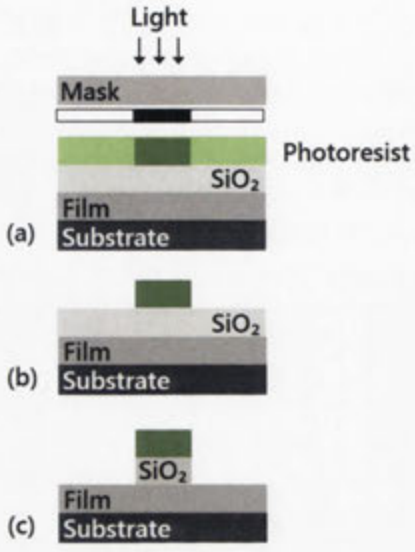

Figure 2.3: Basic photolithography process: (a) positive photoresist is applied as a thin film onto a wafer, and subsequently exposed through a mask, (b) patterns are formed when the the resist is developed, in which protecting the underneath region of the wafer from the subsequent processing, and (c) final etched pattern.

The final step, following development process, the regions of SiO_2 which no longer covered by the resist are removed by HF etching, thereby replicating the mask pattern in the oxide layer. The resulting patterned wafer is then post-bake (hard-baked) at higher temperature ($< 200°C$) for 20 to 30 min to harden the remaining resist and to remove any residual developer from the wafer. This pattern of resist can be used as a protecting layer for future processes such as ion implantation and chemical etching.

2.1.4 Details of ion-implanted sample preparation

Several different thickness of a-Si films, were prepared as required by the different characterization techniques used in the present study. A continuous a-Si films for Raman spectroscopy and indentation studies were formed by multiple irradiations of 0.08, 0.5, 1, 1.5, and 2 MeV Si ions on a Czochralski-grown p-doped Si (100) wafer. This resulted in a 2.1 μm thick amorphous layer.

A second type of sample was 800 nm thick a-Si. This sample were prepared by irradiating Si ions on a Czochralski-grown p-doped Si (100) wafer using energies of 80 and 500 keV. A fluence of 1×10^{15} ions cm^{-2} was used for each energy. These samples were used for the re-irradiation studies.

A third type of sample consisted of a 100 nm thick p-type silicon on insulator (SOI) wafer which was patterned using potholitography. These samples were then irradiated using 25, and 55 keV Si ions (on one side only) with a fluence of 1×10^{15} ions cm^{-2}. This resulted in a 100 nm thick amorphous films. These films were used for electrical conductivity measurements and defect studies.

Starting wafer	Resulting a-Si	Energy (keV)	Fluence (ions cm^{-2})
c-Si	2.1 μm	80	1×10^{15}
		500	1×10^{15}
		1000	1×10^{15}
		1500	1×10^{15}
		2000	1×10^{15}
c-Si	800 nm	500	1×10^{15}
		80	1×10^{15}
100 nm SOI	100 nm	55	1×10^{15}
		25	1×10^{15}
2.4 μm SOI	2.4 μm	2200	3×10^{15}
		1000	3×10^{15}
		500	3×10^{15}
		80	1×10^{15}

Table 2.2: Summary of the irradiation conditions used for the implantation processes. Implantations were performed at liquid nitrogen temperatures and ~7° off to the beam direction to minimize ion channeling.

A fourth type of sample was prepared by irradiating 2.4 μm thick p-type silicon on insulator (SOI) wafer with Si ions using multiple energies of 0.5, 1.0, and 2.2 MeV. A fluence of 3×10^{15} ions cm^{-2} was used for each of the energy. An additional surface implantation to a fluence of 1×10^{15} at energy of 80 keV was performed to ensure a complete amorphization to the surface. This resulted in a uniform 2.4 μm thick amorphous layer. To create a-Si membranes, the a-Si layers were separated from the substrate by removing the silicon dioxide (SiO_2) using HF etching. These membranes were used for the calorimetry studies.

All irradiations were performed at liquid nitrogen temperatures to suppress dynamic annealing effects and ~7° off to the beam direction to minimize ion channeling. The conditions used in the implantation processes are summarized in table 2.2. It should be noted that, although prepared differently, these samples have a similar unrelaxed structure as measured by Raman spectroscopy.

2.1.5 Pressure-induced amorphization

Pressure-induced (PI) amorphization has been observed for many solids such as element, compounds, and alloys. The first PI amorphization was observed on the Ga-Sb system [103]. In that study, Ga-Sb was pressurized to induce a phase transformation to a

metallic GaSb-II and then cooled to liquid nitrogen temperature. Upon pressure release and subsequent heating to room temperature the material transformed to an amorphous phase.

It was first observed by Clarke *et al.* [56] that PI amorphization also occurs in c-Si upon indentation. The formation of the amorphous phase was attributed to the fast unloading rate used, which prevented the nucleation of the crystalline phases. The formation of the PI a-Si from Si-II through rapid unloading is shown schematically in Fig. 2.4.

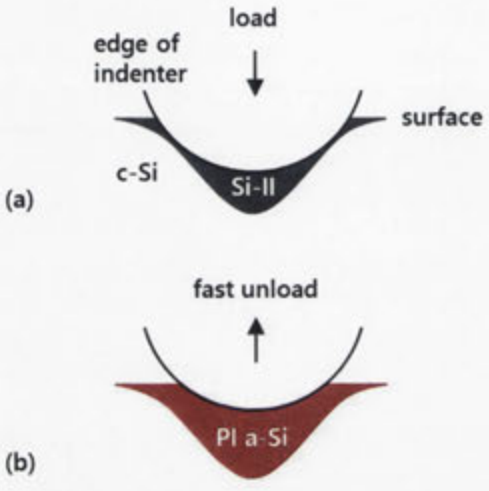

Figure 2.4: Schematic of the formation of PI a-Si through fast indentation unloading.

The PI a-Si used in this study was formed using UMIS indentation instrument with a spherical diamond indenter of 20 μm radius at room temperature. A large array of indents was created on a single crystal Cz Si(100), p doped with boron to a resistivity of 10-20 Ω cm. Loading was performed to a maximum load of 700 mN with a constant rate of ~13.5 mN s^{-1} and unloading was performed within 1 s. The loading condition used to ensure that a large volume of Si-II was created and no cracking occurred after indentation, while fast unloading guaranteed the formation of a-Si. Raman spectrocopy was used to confirm that crytalline phases were not present within each residual indent.

2.2 Characterization techniques

2.2.1 Transmission electron microscopy

A transmission electron microscopy (TEM) is powerful tool allowing a detailed visual examination of a sample in the micro to nano scale regimes. There are two common modes of imaging techniques in TEM, bright field (BF) and dark field (DF) imaging modes [104]. In BF mode, an objective aperture is inserted in the back focal plane of the objective lens. Thus only allows the direct undiffracted electron beam passes through the aperture and

interacts with the sample. In this imaging mode, thick areas of the sample will appear dark due to diffraction and/or absorption contrast, while thinner areas appear lighter. In DF mode, the objective aperture is used to select one or more diffracted beams from the sample. Thus, the image obtained in DF mode is due to scattered/diffracted electrons, and this results in an image with inverted contrast. Since this mode uses a specific Bragg diffracted electrons to image a specific area, DF images contain a very useful information, e.g. defects or particle size, of that area.

Another powerful TEM mode is electron diffraction (ED). This mode uses a collective scattering phenomenon by which electrons are elastically scattered by atoms. This phenomenon can be explained in anology to the Huygen principle. The incoming plane electron waves interact with the electron shells of the atoms. The plane electron waves generate secondary waves which are interfering either constructively or destructively. The mutual reinforcement of waves at certain scattering angle generates the diffracted beam. The diffracted beam from a set of parallel lattice planes is represented by a pair of spots in the ED pattern.

The Bragg condition for mutual reinforcement is given by:

$$n\lambda = 2dsin\theta \tag{2.4}$$

where λ is the wavelength of the electrons, and d is the interplanar distance. Given that the wavelength of the electrons is known, interplanar distance can be calculated from the ED pattern.

Electron diffraction pattern from a single crystal consists of regularly spaced spots. A series of rings in the case of a polycrystalline and diffuse rings for amorphous solid material. Thus, electron diffraction can be used to obtain information whether the sample is single crystal, polycrystalline, or amorphous.

The TEM instrument used in this study is a Phillips CM 300 operating at an accelerating voltage 300 kV. Using a Gatan's dimple grinder, cross-sectional samples were thinned to a thickness of 10 μm [105]. These samples were further thinned to electron transparency using Gatan's precision ion polishing system (PIPS).

Specimens prepared in this manner were used to examine the microstructure (i.e. to confirm amorphicity) and determine the thickness of the a-Si layer produced by ion-implantation.

2.2.2 Secondary ion mass spectroscopy

Another important characterization tool used in this thesis is secondary ion mass spectrometry (SIMS). This technique was pioneered by Benninghoven *et al.* [106]. SIMS is a surface analysis technique based on the observation: when a solid is bombarded with energetic ions (primary ions), the ions knock out charged particles (secondary ions) from

a sample surface, a process also known as sputtering. This process is illustrated in Fig. 2.5. There are various modes of SIMS analysis including depth profiling. In depth profiling mode, the composition of the elements of interest is recorded as a function of sputtering time. SIMS uses primary ions of heavy particles, such as O_2^-, O_2^+, Cs^+, or neutrals with energies in the range of 250 eV to 30 keV, to sputter off atoms and molecules from a sample surface. A fraction of these atoms and molecules are ionized (secondary ions) and can be separated according to their mass to charge ratio with a mass spectrometer. Thus, the elemental, isotopic, or molecular composition of the sample surface can be determined.

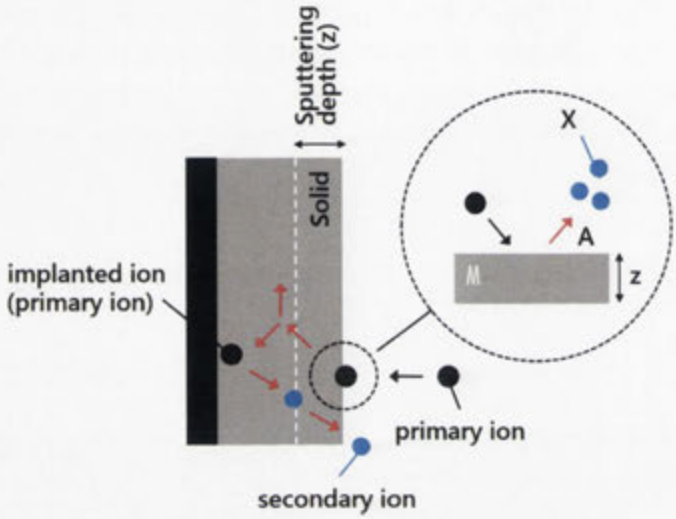

Figure 2.5: Principle of SIMS. The energetic primary ion penetrates a solid and undergoes a series of collision which the target atoms. Some of the atoms near the surface are ejected from the surface and ionized; these are secondary ions.

The fundamental SIMS equation

The sputtering yield of the secondary ions is determined by the ionization probability (α) of the detected species. This parameter is not only depend on the electronic properties of the species but also on the electronic properties of the matrix. Hence, the intensity of the detected secondary ions is not a direct measure of the concentration of the species in the sample [107]. As illustrated in Fig. 2.5, a volume of material (Az) is removed through sputtering. Thus, the volume removed by sputtering can be defined as:

$$V = Az \tag{2.5}$$

where A is the area of material being analyzed and z is the depth of the material removed. Assuming that the material contains species atom X, and all of these atoms are sputtered off. The number of sputtered atoms X is given by:

$$N_X = \rho_X(Az) \tag{2.6}$$

where ρ_X the average concentration of the atom X.

The sputtered atoms X are mostly monoatomic, but some of them are partially in the form of dimeric or higher order polymeric species Some fraction of these sputtered atoms will be ionized. If we consider the atomic positive ion X^+, the number of the detected secondary ions that are detected is thus given by:

$$N_{X^+} = (\alpha_{(X^+)}T_{(X^+)})\rho_X(Az) \tag{2.7}$$

where $\alpha_{(X^+)}$ is the ionization probability for X^+, and $T_{(X^+)}$ is the transmission coefficient of the X^+ ion. The

The product of $\alpha_{(X^+)}$ and $T_{(X^+)}$ is known as the useful ion yield $Y(X^+)$. Even though, it is not normally possible to measure $\alpha_{(X^+)}$ and $T_{(X^+)}$ independently, $T_{(X^+)}$ for example is correlated with the ratio of the detected ions X^+ to that of secondary ions X^+ ejected from the sample. This parameter can vary depending on the experimental conditions, such as mass and energy of the primary ions. However, the useful ion yield $Y(X^+)$ can be easily measured with the use of a standard. This parameter is determined by taking the ratio of detected secondary ions to sputtered atoms from an ion-implanted standard with known impurities.

Quantification of SIMS data

The standards for this study were made by implanting hydrogen into a-Si at room temperature (as detailed in section 2.1.1) to a fluence of 1.25×10^{16} ions cm^{-2} with an energy of 50 keV. These implantations were done at the Universität of Augsburg, Germany. In silicon, as simulated by SRIM, the above irradiation conditions yield a concentration of hydrogen of $\sim10^{21}$ at. cm^{-3} centered at $\sim$500 nm depth.

Figure 2.6 shows the intensity of hydrogen as a function of depth for hydrogen implanted into a-Si. The conversion of sputtering time to sputtered depth was obtained by measuring the crater depth of the analyzed area using a profilometer. The sputer rate was calculated by dividing total crater depth by total sputter time. Thus, the sputtered depth is simply the product of the multiplication of the sputter time by sputter rate.

One of the standard methods to convert count rates into concentration is by calculating the sensitivity constant S. The constant S is defined as:

$$S\int(counts/s)dt = \int(at/cm^3)dh = S\int(counts/s)(dhdt/dh) \tag{2.8}$$

by rearranging the equation, S is then given by:

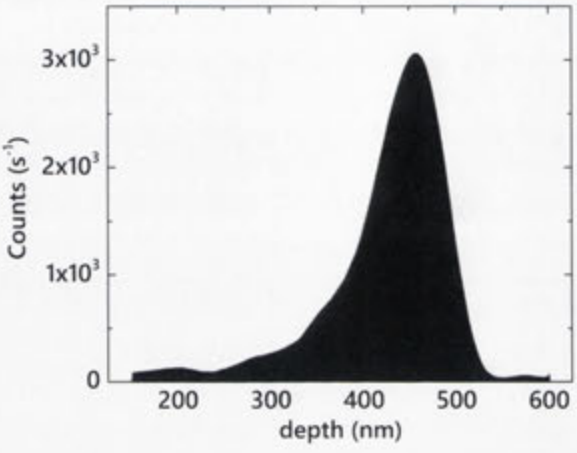

Figure 2.6: SIMS depth profile of the hydrogen ion as a function depth for hydrogen implanted into a-Si. The sample was analyzed using a 10 keV O_2^+ beam at an angle of incidence of 60° on an Atomika 4100 at the Universität of Augsburg, Germany.

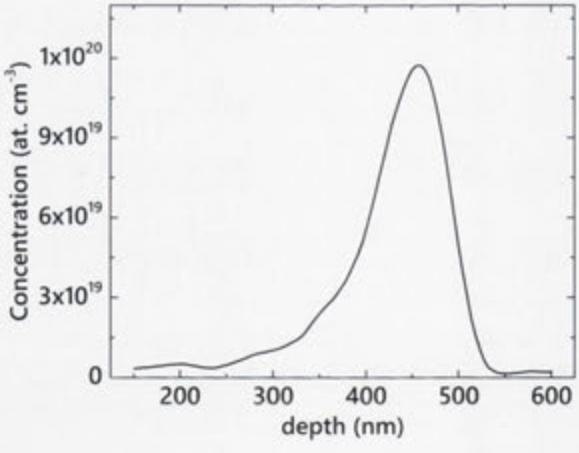

Figure 2.7: The depth profile of the hydrogen ion concentration in hydrogen implanted into a-Si.

$$S = Q/\int(counts/s)dt \tag{2.9}$$

where Q is the fluence of the implanted hydrogen and $\int(counts/s)dt$ is the number of hydrogen ions detected. The number of detected hydrogen ions can be calculated by integrating the area under the curve in Fig. 2.6. As shown in Eq. 2.9, the sensitivity constant S is the ratio of the number of hydrogen ions implanted into a-Si to the number of hydrogen ions detected. Thus, S is related to the $Y(X^+)$ factor. Most importantly, the constant S eliminates the dependencies of the measurement on sputtering yield and experimental conditions.

The concentration of hydrogen ions is then

$$C_{H^+} = S(counts/s)t(dt/dh) \tag{2.10}$$

where dh/dt is the sputter rate. The depth profile of the hydrogen ion concentration in a-Si is shown in Fig.2.7.

Experimental conditions of SIMS

The SIMS data were obtained using the Atomika 4100 instrument with 10 keV O_2^+ primary ion beam energy at a 60° angle of incidence from normal.

2.2.3 Raman spectroscopy

Raman spectroscopy is a vibrational spectroscopy technique. It is based on the scattering of a photon by the electrons of molecules or crystal atoms. As illustrated in Fig. 2.8, when the incident light interacts with a matter, photons are absorbed and scattered in several different ways. If the energy of scattered photons and molecule remain constant, these photons were elastically scattered, also know as Rayleigh scattering [108]. The Rayleigh scattering is the strongest process since most photons are scatter elastically. But if, on the other hand, the energy of scattered photons is less or greater than the incident photons, these photons were inelastically scattered. These are called Stokes and anti-Stokes scatterings. The difference between the energies of the scattered and incident photons is a direct measure of vibrational energies of the molecule. The inelastic scattering between a photon and a molecule is known as the Raman effect.

The incident photons have an electric field that is described by:

$$E = E_o cos(2\pi\vartheta_{ex}t) \tag{2.11}$$

where E_o is the power of the incident photons, and ϑ_{ex} is the frequency of the excitation energy. Interaction of the electric field of the incident photons with the molecule induces a dipole moment, $m = \alpha E$, where α is the polarizability of the molecular bond vibrations.

The proportional constant α measures the ability of the electron cloud around a molecule to be distorted. The molecule is Raman active only if the polarizability of the molecule changes during vibration.

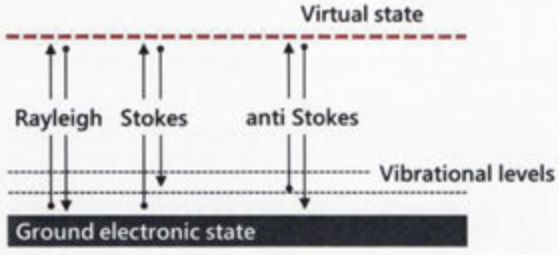

Figure 2.8: A simplified energy level diagram showing Rayleigh, Stokes and anti-Stokes energy transfer processes.

In crystalline solids, Raman scattering deals with phonons, instead of molecular vibration. The crystal symmetry determines the ability to form dipole, and this influences the polarizability of a solid [109]. Thus, only specific phonons are Raman active and only if the derivative of the polarizability with respect the normal coordinate of the vibration is nonzero, also known as the Raman selection rule. In disordered solids, the selection rule is no longer applicable, as the Brillouin zone in amorphous structure is not well defined [110]. Therefore, in disordered solids all phonons contribute to the Raman spectrum. This leads to broad bands rather than discrete spectral lines (see Fig. 2.9).

A Raman system typically consists of: a monochromatic light source (laser), collecting optics, a spectrometer to separate light according to wavelength, and a detector. A sample is illuminated with a laser in the ultraviolet, visible or near infrared range. The scattered light passes through a notch filter, whereby only Stokes and anti-Stokes signals are transmitted and sent to a detector to obtain the Raman spectrum of the sample.

Raman spectroscopy has many advantages over other analytical techniques. Typically no sample preparation is needed, non-destructive, sensitive to changes in structural properties, acquisition times are on the order of seconds, and Raman spectrum can be collected from a very small area (less than 1 μm in diameter). Therefore, Raman spectroscopy is a powerful tool for investigating residual indents, especially to detect phase transitions in silicon and amorphous silicon [66, 111].

Raman spectra of amorphous materials

As previously noted, a characteristic feature of amorphous materials is the absence of long range atomic or crystallographic correlations which are present in the crystalline material. The breakdown of selection rules allows scattering at broad range of energies. This introduces the appearance of a strong broadening of the Raman spectrum which corresponds to the disordered state of the amorphous material.

A typical Raman spectrum of a-Si is shown in Fig. 2.9(b). The Raman spectrum of a-Si consists of two main bands, at about 150 and 480 cm^{-1}. These bands are associated with TA and TO vibrational modes, respectively. Raman spectrum are highly sensitive to changes in the structural properties of the a-Si such as the dihedral-angle deviation and the bond-angle distortion ($\Delta\theta$).

The TO band is related to the bond-angle distortion, indicated by a broadening of the width of the TO band with increasing $\Delta\theta$ [46]. Beeman's linear relation [25],

$$\Gamma(TO) = 15 + 6\Delta\theta \tag{2.12}$$

where Γ(TO) is the width of the TO band in cm^{-1} and $\Delta\theta$ is in degrees, is generally used to calculate $\Delta\theta$ from the Raman spectrum. Since the lower frequency side of the TO band is overlapping with acoustic modes [112] (see Fig. 2.9(b)), Γ(TO)/2 is often used for the analysis rather than Γ(TO).

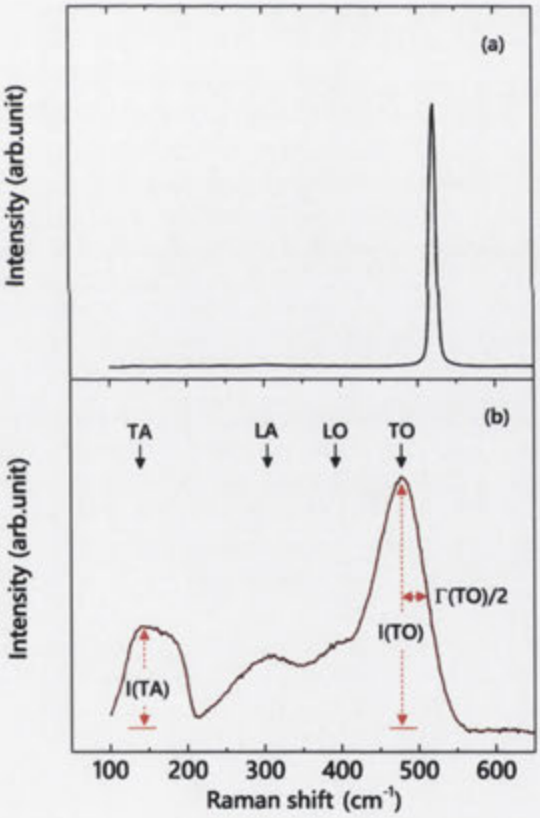

Figure 2.9: Raman spectrum of (a) c-Si, and (b) a-Si. The red solid/dash line is the smoothed curve after applying the Savitzky-Golay filter.

In order to extract the half-width of the TO band, the spectrum is smoothed by employing the Savitzky-Golay filter using the package Origin [113]. In Fig. 2.9, the smoothed curve (red solid/dash line) is shown to superimpose well on the original curve (black solid

line). The background is taken at the wavenumber of 700 cm^{-1}. The intensity of the TO band is directly determined from the smoothed curve. The $\Gamma(TO)/2$ on the high-frequency side is then defined at half of the maximum intensity.

Another interesting feature on the Raman spectrum is the location of the TO band, $\omega(TO)$. It has been suggested that $\omega(TO)$ is shifted to higher wavenumber with increasing structural order [25, 114, 115]. It should be noted, however, that the position of the TO band is also affected by residual stress. An increase in the residual stress has been reported to also shift $\omega(TO)$ towards higher wavenumber [116].

Information about dihedral-angle deviation can be extracted from the intensity of the TA band. This intensity is correlated to the fluctuation of the density of the dihedral-angle [25, 53, 54]. Therefore, a more ordered network will yield a lower TA band intensity. Previous studies [54, 117, 118] indicate that the intensity ratio of the TA to TO band is related to the bond-angle distortion, with a lower intensity ratio indicating a more ordered network. Analogous to the TO band, the intensity of the TA band is also determined after employing the Savitzky-Golay filter on the spectrum. The intensity of the TA band is determined from the maximum intensity on the low-frequency side of the TA band as this side does not overlap with optic modes [112].

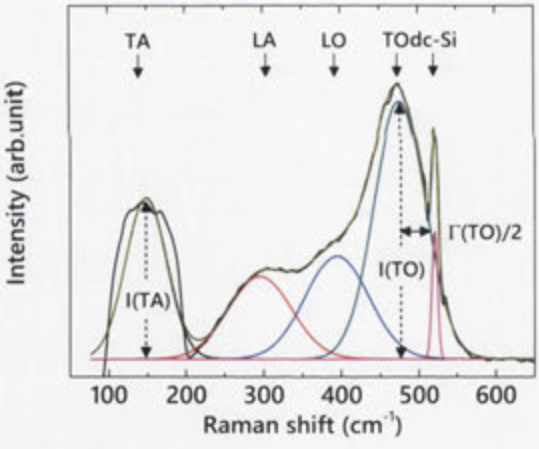

Figure 2.10: Raman spectrum from PI a-Si. The intensity of the TA and TO bands and half-width of the TO band are determined after applying the Lorentzian fit.

The same procedure, however, cannot be applied for the Raman spectrum of PI a-Si. As shown in Fig. 2.10, a dc-Si band at about 520 cm^{-1} appears in the Raman spectrum of PI a-Si. The appearance of this band is due to the Raman active volume that is deeper than the a-Si depth in the indent. In this particular case the intensity and half-width of the TO band, and the intensity of the TA band are determined after applying the Lorentzian fit function using the package Origin [113].

Experimental conditions of Raman spectroscopy

Raman spectra for a-Si films following thermal annealing and indentation (to detect end phases within the volume of the residual indents) were recorded with a Renishaw 2000 fitted with a 633 nm wavelength He-Ne laser. The recording time of a single Raman spectrum was 30 s. Repeated tests on the same area showed that the a-Si was not altered by the measurement.

2.2.4 Indentation

Indentation is conceptually a simple technique, where a sharp tip is forced down into the surface of the material. The force needed to push the tip into the sample and the resultant residual area of the indent are then combined to determine the mechanical properties of the sample. However, in this thesis indentation is used solely as a means to detect the presence (or absence) of pressure-induced phase transformation and to form pressure-induced a-Si.

Ultra micro-indentation system

Ultra micro-indentation system (UMIS) 2000 developed by the Commonwealth Scientific Industrial Research Organization (CSIRO) was used to create indents. This instrument is a force-driven device. The indenter is driven into the surface of a testing material until the resistance reaches the pre-set force. The penetration of the indenter is determined under conditions of force equilibrium at each series of force steps. The load and displacement of the indenter into the material are measured throughout a cycle of loading and unloading.

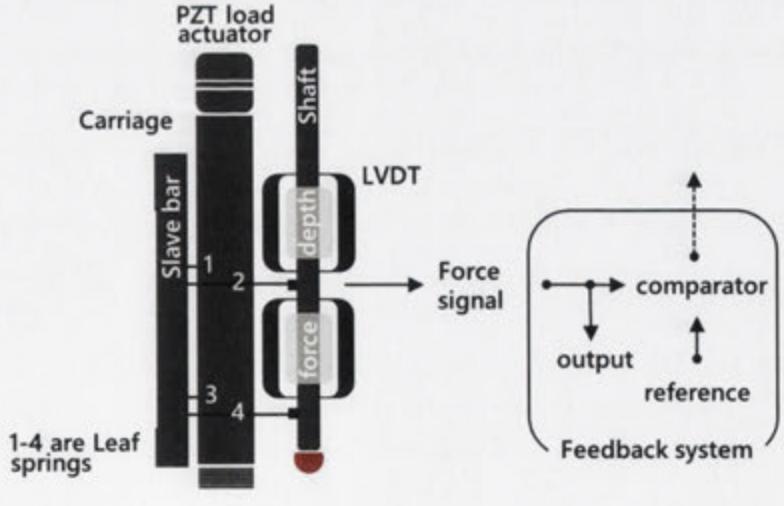

Figure 2.11: Schematic of the UMIS-2000 indentation instrument.

The schematic of the UMIS indentation instrument is shown in Fig. 2.11. An indenter is attached to a shaft supported by four leaf springs. A main carriage with leaf springs is

driven downwards by a piezo load actuator. The position of the shaft is recorded using a depth linear variable differential transformer (LVDT). When the indenter and the sample surface come into contact, the leaf springs are deflected relative to the main carriage and monitored by a force LVDT. This deflection generates an indenting force. In this point, the depth LVDT output is also zeroed to establish a reference point for the depth measurement during indentation.

In order to reduce the effect of hysteresis and non-linearity in the load actuator, the applied force in this system is controlled by a feedback loop system. The difference in output force signal and reference voltage is used to control the piezo load actuator to either expand or contract. Through the leaf springs, the expansion and contraction of the actuator apply a variable load to the indenter, and produces a stepped force on the indenter.

A continuous load-unload cycle is the standard test available on the UMIS. In this method, the indenting force is increased to a pre-set maximum force and then decreased back to the contact value. The load and unload segments can be split into a number of steps, by which the force and depth are measured in each step. The output from indentation test is a load-depth (P-h) data.

Evidence of phase transformation observed from the load-depth curve

As illustrated in Fig. 2.12, under applied stress, relaxed a-Si phase transforms into a metallic Si-II phase. Upon pressure release to a critical contact pressure, a phase transformation from Si-II to Si-III/XII commences. In the initial of unloading stage, due to the absence of the preferential nucleation sites, the transformation of Si-II phase to Si-III/XII expands slowly and gradually toward the center of the deformed zone. As a result, the volume change induced by the phase transformation is limited. Upon subsequent slow unloading, a rapid growth of high pressure phases takes place in the deformation zone causing a sudden volume expansion. Consequently, a distinct displacement continuity, a pop-out, appears in the unloading segment (refer to Fig. 1.7(b))

The pop-out event clearly confirms that phase transformation had occurred during loading. Therefore, the absence of a pop-out event suggests deformation via plastic flow rather than phase transformation. Thus, the investigation of load-displacement curves is very useful method for searching an evidence of phase transformation. This phase transformation behavior is also proven as a useful method to investigate the state of a-Si. As shown in Fig. 1.7 [65], the occurrence of a pop-out, in the P-h curve is restricted to relaxed a-Si, indicating that it deforms via phase transformation, whereas unrelaxed a-Si deforms via plastic flow. This different deformation behavior is clearly an indicative of the different states of unrelaxed and relaxed and a-Si [47, 66].

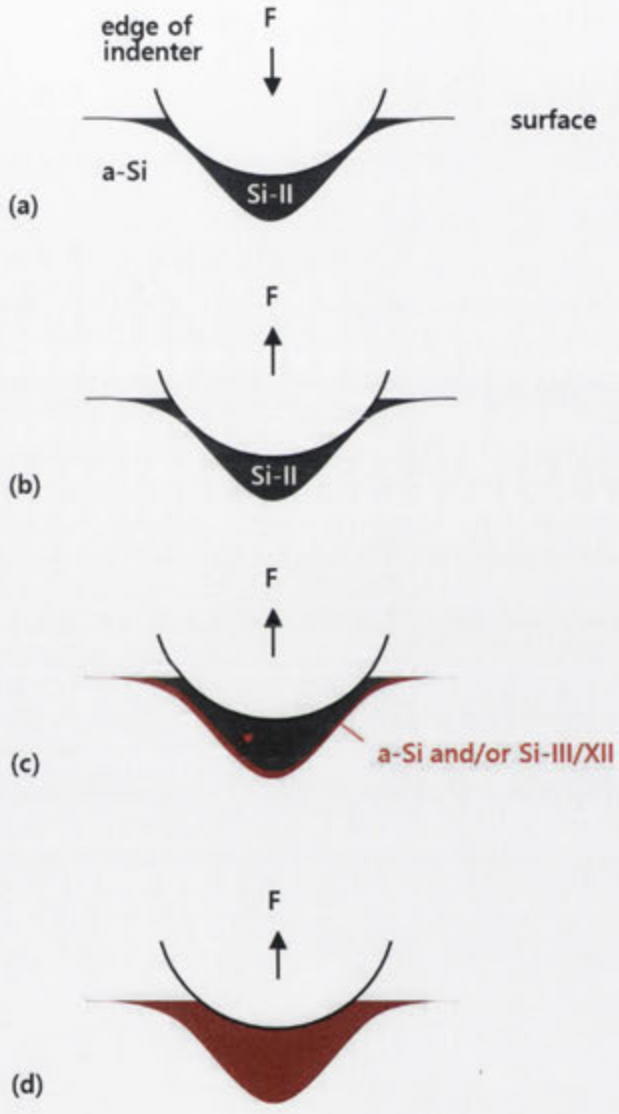

Figure 2.12: a-Si transformed into Si-II on loading. Upon slow unloading, Si-II phase transforms Si-III/XII. Rapid growth of the high pressure phases causing a sudden volume changes, and thus a pop-out appears on the unloading segment.

Experimental condition for UMIS

For the detection of phase transition versus their absence in a-Si, throughout the entire study, a 4.3 μm radius spherical diamond tip was used. The applied maximum load was 80 mN resulting in a maximum penetration depth of ~400 nm. The force was increased in 50 steps to the maximum load and then released in the same step-wise manner.

Pressure-induced a-Si was formed using a spherical diamond indenter of 20 μm radius. Loading was performed to a maximum of 700 mN with a constant rate of ~13.5 mN s^{-1} and unloading was performed within 1 s.

2.2.5 Electrical conduction

The fact that amorphous semiconductors can be doped to form either an n- or p-type extrinsic semiconductor resulted in a renewed interest in their electronic properties. As a consequence of the disorder in amorphous solids, their intrinsic localized states are found to exist within the band gap [119]. These localized electronic states, produced by defects and impurities, dominating most of the charge-related processes that occur within the material, in particularly those involving carrier transport and generation-recombination processes.

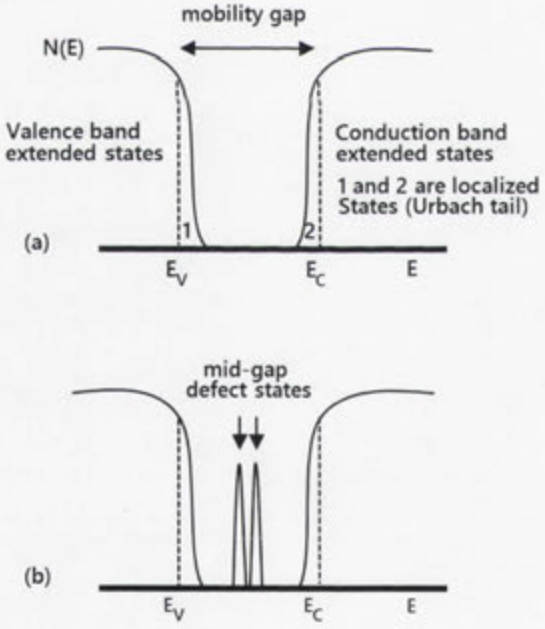

Figure 2.13: Simple band diagram of amorphous semiconductor, such as a-Si, showing valence (E_V) and conduction (E_C) bands, band tails (localized states), and mid-gap defect states [120].

Figure 2.13(a) illustrates a simplified density of states (DOS) of an amorphous semiconductor showing valence (E_V) and conduction (E_C) bands, and band tails (localized states) [120]. Structural defects arising from incomplete or dangling bonds or impurities create localized mid-gap states that pin the Fermi level, as shown in Fig. 2.13(b).

The electronic transport in amorphous semiconductors is thermally activated. Conduction cannot occur in the localized states and gap states at *zero* temperature. At finite temperature, however, thermally activated hopping transport between localized states occurs in amorphous semiconductors [119].

Nature of localized states in a-Si

It has been reported that a-Si formed via ion implantation contains a wide variety of structural defects, such as dangling bonds [28], and vacancy-type defects [67]. However, Fedders *et al.* [121] using a Bethe-lattice terminated nine atom cluster and a tight binding approach shown that the dangling-bond state is more localized compare with other defect states. This suggests that broken bonds (or dangling bonds) are possibly the dominant defect in the localized states near the Fermi level. These defects create localized states that pin the Fermi level.

Electronic transport in a-Si

The electronic transport in amorphous materials, such as a-Si, has been successfully explained by the theory of electron conduction proposed by Mott [122]. The idea is based on a model in which charge is transported by thermally-excited hopping of electrons between randomly placed potential wells (impurities). Conduction is then characterized by two different mechanisms dependent upon temperature; thermally assisted tunneling of charge carriers in the band tails or variable-range hopping in the gap states.

At sufficiently high temperatures, conductivity is predominately due to charge carriers in the localized states in the band tails. The conductivity is given by:

$$\sigma_{tail} = \sigma^{'} exp(-\Delta E/kT), \tag{2.13}$$

where $\sigma^{'}$ is the conductivity at the respective electronic energy level in the conduction mobility edge, k is the Boltzmann constant, and ΔE is the activation energy. The ΔE is the energy difference between the mobility edge and the Fermi level, E_C-E_F or E_F-E_V.

At low temperatures, conduction is predominately due to charge carriers in the gap states, and characterized by Mott's variable-range hopping relation [122]. The conductivity in the low temperature region is given by:

$$\sigma(T) = \sigma^{'} T^{-\frac{1}{2}} exp(-AT^{-\frac{1}{4}}) \tag{2.14}$$

where, the value of $\sigma^{'}$ is given by:

$$\sigma^{'} = 3e^2 v(N(E_F)/8\pi\alpha kT)^{\frac{1}{2}} \tag{2.15}$$

where e is the charge of an electron, v is the Debye frequency, 10^{13} Hz, $N(E_F)$ is the density of localized defect states at the Fermi level, and α is the extent of the wave-functions of electrons in hopping sites. The value of the parameter A has been shown by Mott to be approximately given by:

$$A^4 = T_0 = \lambda\alpha^3/kN(E_F), \tag{2.16}$$

where λ is a dimensionless constant. Taking a typical value localization of the electron wave function in hopping sites (α) in Eq. 2.15 for 10^7 cm^{-1} and for the dimensionless constant λ to be 18 (these values are assumed not to change as a function of the *degree* of relaxation), the density of localized states at the Fermi level is then given by:

$$N(E_F) = 1.86 \times 10^{26} A^{-4}. \tag{2.17}$$

Since the presence of defects such as dangling bonds in a-Si creates localized states near the Fermi level, the conduction mechanism in the low temperature region is therefore sensitive to the number of dangling bonds in the amorphous network.

Experimental details of electrical measurements

The schematic of the temperature-controlled system that is used for the electrical measurement is shown in Fig. 2.14. This system consists of four major components: a sample chamber, a heater coil, a helium cryostat to cool samples down to around 4 K, and a direct current (DC) voltage source to produce DC current.

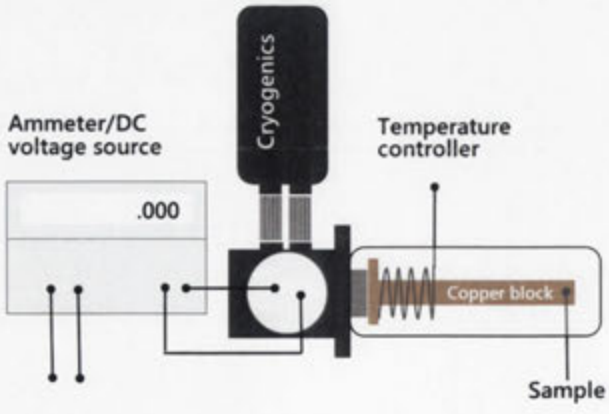

Figure 2.14: The schematic of the temperature-controlled system at the Australian National University.

The sample (detail of the device fabrication will be discussed later in section 5.2) is positioned on the sample holder in good thermal contact with the copper block heat exchanger and surrounded by a vacuum. Therein, the sample is cooled by thermal conduction through the copper block. Temperature control is achieved by a combination of helium flow control and power dissipated in an electrical heater wounded around the extended part of the copper block, regulated using a thermocouple. The temperature is monitored by a temperature sensor fitted on the heat exchanger. A direct current, produced by a DC voltage source, flows through the sample (see section 5.2).

The parameter A in Eq. 2.17 is extracted by measuring the sheet resistance of the sample from the measurement of the voltage drop across a resistor as function of temperature from 80 to 300 K using Keithley nanovoltmeter. Output from this measurement is a current-voltage characteristic or I-V curve between the electric current through the sample and the corresponding potential difference (see chapter 5 for details).

Sheet resistance

Sheet resistance is commonly used to characterize diffused or implanted semiconductor films [123]. In these films, the distribution of the charge carriers is not uniform, as a result their resistivity is a strong function of depth. Therefore, the parameter sheet resistance is often used instead of resistance, because it is independent of the film thickness.

Figure 2.15: Geometry for defining sheet resistance. The measure of current flow is parallel to the length of the conductor, as shown by the white arrow.

In a regular three-dimensional conductor, as shown schematically in Fig. 2.15, the resistance is given by:

$$R = \rho L A^{-1} = \rho L (wt)^{-1} = (\rho t^{-1}) L w^{-1} \tag{2.18}$$

where ρ is the resistivity, A is the cross-sectional area and L is the length. Since the cross-sectional area is equal to the width w times the sheet thickness t, the resistance can then be written as:

$$R = R_s L w^{-1} \tag{2.19}$$

where R_s is the sheet resistance. If the film thickness is known, the bulk resistivity ρ (in ohm cm) can thus be calculated by multiplying the sheet resistance with the film thickness

$$\rho = R_s t = (V I^{-1}) t \tag{2.20}$$

where R_s can be obtained from the current-voltage characteristic curve.

2.2.6 Calorimetry

Calorimetry is a standard technique to establish the relationship between thermal properties and structural changes in materials. Indeed, this is the only method for direct determination of the enthalpy associated with the thermal relaxation process of an amorphous network [124].

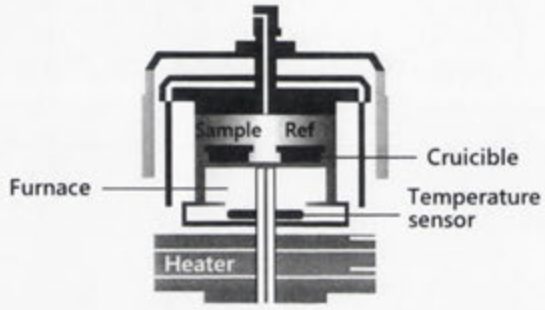

Figure 2.16: Schematic of differential scanning calorimetry.

Differential calorimetry

Among various types of calorimeters, differential scanning calorimeter (DSC) is the most appropriate for this application. The technique was developed by E. S. Watson and M. J. O'Neill in 1962 [125], and introduced commercially at the 1963 Pittsburgh Conference on Analytical Chemistry and Applied Spectroscopy. A DSC is a thermal analysis apparatus that can measure the heat quantity, which is released or absorbed by the sample as a function of temperature as the sample is heated, cooled or held isothermally at a constant temperature. The core of the measurement is based on the temperature difference between the sample and the reference material [126].

In this thesis, DSC was used to measure the heat liberated from a-Si during thermal annealing. The measurements were carried out in a Mettler Toledo DSC 1 instrument at the Australian National University (ANU). This instrument consists of a furnace, specimen crucibles, and thermocouples that measures the difference between the two heat flows from the sample and reference pans. The schematic of the DSC is shown in Fig. 2.16.

Experimental details of DSC

A pan consisting of 2.4 mg (0.0854 mmol) of a-Si powder was prepared by grinding a-Si membranes (for preparation details see section 2.1.4) inside the crucible with an applicator stick. The reference pan was loaded with c-Si powder of the same weight as the measured sample. After loading the pans, but before measurement, the calorimeter was allowed to

equilibrate at 25°C for 15 min. Scans ran from 25 to 150°C at 40 K min^{-1}, and held at the end of this temperature for 30 min to establish isothermal signal before it cooled down to 25°C. After cooling down to 25°C, without changing the sample, a second scan was taken to 250°C using the same scan rate, it was then held at 250°C for 30 min and cooled down again to 25°C before repeating the scan for higher end temperatures.

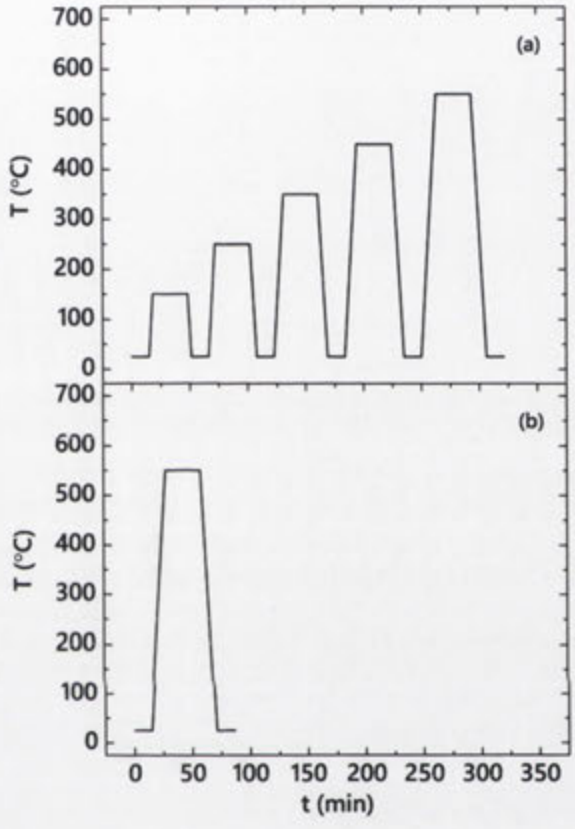

Figure 2.17: Scan method for (a) measuring the heat release from relaxation anneal and (b) determining the baseline (without changing the sample). Scan rate of 40 K min^{-1} was used for all scans.

Figure 2.17 shows the scan method of the measurement. Ideally, the heat release from the second scan corresponds to the structural changes in the sample from 150 to 250°C, while the first scan corresponds to structural changes from 25 to 150°C. Following the final measurement at 450°C, the sample was then scanned from 25 to 550°C without changing the sample to determine the baseline (see Fig. 2.17). Subtraction of the baseline from previous scans gives the heat release from the sample.

Stored enthalpy determined by scanning calorimetry

Figure 2.18 shows the dynamic and the isothermal traces from heating the sample from 25 to 150°C. A positive signal corresponds to a heat releases by the a-Si during annealing

from 25 to 150°C. The heat release is calculated by integrating the area under the curve (includes the baseline subtraction) in Fig. 2.18. This yields a heat released of 14.6 kJ mol^{-1}, which is the total heat produced by relaxation during annealing of the as-implanted sample from 25 to 150°C.

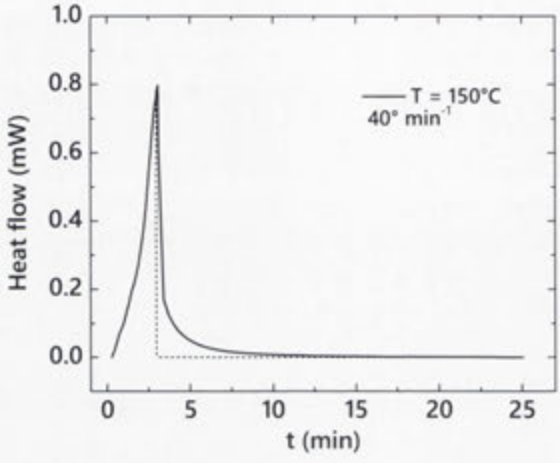

Figure 2.18: DSC curve of a-Si annealed from 25 to 150°C. Dotted lines serve to separate the dynamic and isothermal signals. Integration of the area under the curve yields a total heat released of 14.6 kJ mol^{-1}.

3

Local atomic order

3.1 Introduction

In the case of a-Si produced by ion implantation, the changes occurring in its physical structure upon annealing is referred to as structural relaxation. This process is related to defect annihilation (recombination) and short-range ordering of the network (rearrangement of the Si bonds). The latter, short-range ordering, is reflected in a decrease of the bond-angle distortion ($\Delta\theta$) as detailed in section 1.2.

On average, the bond-angle distortion for a-Si obtained by self-ion implantation has been found to be $\sim 12^{\circ}$ (as-implanted). The bond-angle distortion reduces to $\sim 9^{\circ}$ when it is thermally annealed (fully relaxed) [14, 15]. A number of studies, both experimental and theoretical have been carried out to determine the bond-angle distortion in an effort to understand the structural relaxation process. However, few studies have focused on how the bond-angle distortion changes during the relaxation process.

As previously detailed in section 2.2.3, Raman spectroscopy is a powerful tool to access the vibrational properties of materials, including amorphous films. Since this technique is sensitive to bond-angle distortion and fluctuation of the density of dihedral-angle in the amorphous structure, Raman spectroscopy has been used as a key tool for the characterization of the *degree* of order in the atomic structure of a-Si. Raman spectrum are highly sensitive to changes in the structural properties of the a-Si. For example, the bond-angle distortion can be directly extracted from the TO band in the Raman spectrum. It is also widely accepted that the width of the TO band is linearly dependent on the bond-angle distortion [25, 46, 127, 128], with a lower Γ(TO) indicating a more ordered network. Other

interesting features related to the *degree* of order in the structure of a-Si are the position of the TO band and the ratio of the intensity of the TA to TO band, by which a higher ω(TO) [25,114] and a lower I(TA)/I(TO) [54,117,118] indicate a more ordered network.

Since ion-implanted a-Si is formed through atomic collision in a highly nonequilibrium process, it is expected that the resulting structure contains a large number of structural defects. These defects act as trapping centers for impurities, such as hydrogen, oxygen, or carbon atoms upon exposure to air. Hydrogen atoms, in particular, can diffuse from the atmosphere during thermal annealing and rearrange the network via local bond switching. At a concentration below 3 at.%, hydrogen is expected to be bonded to Si in a monohydride configuration [129]. The in-diffused hydrogen eventually leads to a passivation (or saturation) of most of the dangling bonds in the network through a formation of Si-H_x bonds [130]. The formation of these Si-H_x bonds induces a local ordering, and thus reducing the average strain ($\Delta\theta$) within the network [50,51]. Indeed an earlier Raman scattering study [131] on hydrogenated a-Si (a-$Si_{1-x}H_x$) prepared by chemical vapor deposition showed that the addition of hydrogen atoms (as low as 0.4 at.%) modified the TO band of the Raman spectrum in the network. This short-range ordering appears to be similar to what is observed in a-Si during thermal annealing [46,132].

As detailed in section 2.1.5, pure a-Si can also be formed by rapid decompression during indentation experiments. Although it is easy to form a-Si via this method, the volume of the a-Si created is limited compare with ion-implanted a-Si. As a consequence, it is difficult to investigate this form of a-Si by most existing characterization techniques. For that reason, PI a-Si has not been studied extensively. Since the mechanism of the formation of PI a-Si is different to that of ion-implanted a-Si, the characterization of this form of a-Si may aid in furthering in the understanding of the structural differences in a-Si structures as prepared by different methods.

A previous study by Haberl *et al.* [133] shows that PI a-Si also undergoes structural relaxation upon annealing at 450°C for 30 min. In comparison with ion-implanted a-Si, PI a-Si is found to be significantly different to ion-implanted a-Si. Although both networks are formed by solid-state amorphization and both relaxed to a CRN, PI a-Si has less order (and thus higher bond-angle distortion and higher intensity ratio of the TA to TO band) than ion-implanted a-Si in both as-prepared and fully relaxed states. Therefore it is intriguing to consider how the short-range ordering occurs in this form of a-Si.

The aim of this chapter is to quantify the variations in the physical properties: $\Delta\theta$, ω(TO), and I(TA)/I(TO) in ion-implanted a-Si and PI a-Si induced by thermal annealing. The comparison between these two forms of a-Si is made in order to investigate whether the local ordering in PI a-Si is similar to that in ion-implanted a-Si. The effect of in-diffused hydrogen in the local ordering of ion-implanted a-Si during the structural relaxation process is also investigated in detail by removing the hydrogen rich region from the samples and then comparing the properties in the as-implanted state and after annealing at various temperatures.

As detailed in Chapter 1, the proposed paracrystalline structure for ion-implanted a-Si is primarily due to the fact that such a-Si is made from a crystal pre-cursor. It is, however, well known that re-irradiation of relaxed implanted a-Si results in similar short-range ordering characteristics as observed for the original as-implanted (unrelaxed) state [14]. It is therefore of great interest to investigate the short-range ordering in such re-irradiated a-Si with the aim to gain further insights into the possibility of a paracrystalline structure due to the crystalline starting material.

3.2 Experimental

1. Amorphization by ion implantation

A set of samples of 2.1 μm thick a-Si (for preparation details see section 2.1.4) was prepared by conducting isochronal annealing on as-implanted samples for 30 min at various temperatures using a rapid thermal annealer (RTA). Upon annealing, the changes in the structure were analyzed using Raman spectroscopy. To study the effect of in-diffused hydrogen in the local ordering, a second set of samples of 2.1 μm thick a-Si (not from the same batch) was prepared and annealed isochronally for 30 min at various temperatures. Due to the unavailability of the RTA after preparing the first set, this particular set was instead annealed using a quartz tube furnace. It is noted in section 2.1.2 that both RTA and quartz tube furnaces do not produce significant differences on the bond-angle distortion. Subsequently, the concentration of in-diffused hydrogen in the sample (H) as a result of thermal annealing was measured by performing SIMS on each annealed sample at the Universität of Augsburg, Germany (see section 2.2.2). Raman spectra from these samples were then recorded. Thereafter, these samples were chemically etched to remove the hydrogen-rich surface region (~250 nm) from the surface of the samples using a chemical etch solution (HNO_3+HF+H_2O) for 15 to 20 s. Raman spectroscopy measurements were then re-performed on these hydrogen-free samples. The conditions of the two sets of samples are summarized in table 3.1. In both cases the samples were annealed in a nitrogen environment.

In both sets of un-etched and etched samples, the acquisition time of a single Raman spectrum was 30 s. Five spectra from different locations on each sample were recorded and analyzed for each measurement. The average values are presented together with standard error.

The following parameters: $\Delta\theta$, Γ(TO), and I(TA)/I(TO) were extracted from the measurements. The bond-angle distortion was calculated using Eq. 2.12, by which Γ(TO)/2 is defined at half the maximum intensity on the high-frequency side and I(TA) is determined from the maximum intensity on the low-frequency side. The error denoted is the standard error from the five different locations on each sample.

Raman spectroscopy measurements on the as-implanted samples of set 1 and set 2 re-

veal a small difference in the Γ(TO)/2. The half-width of the TO band of the as-implanted sample on set 1 is in good agreement with other previous Raman study by Haberl [133], but set 2 yields a slight higher Γ(TO)/2 compared to the set 1. The most plausible explanation for the difference in the Γ(TO)/2 is that both sets were prepared by two separate implantation processes. Hence, a slight difference in the number of defects created during the ion implantation process might be expected from these two different sample sets. As detailed in section 2.1.1, during ion irradiation a number of defects are created, which results in disordering (and ultimately in amorphizing) the crystalline network. However, once the defects reach saturation, they re-annihilate at the expense of generating locally strained regions into the network [134]. Thus, an excess of defects will increase the overall network strain without necessarily increasing the density of defects in the network [75]. Nominally, both sets were implanted under the ideal conditions as detailed in section 2.1.4, however, these two sets of samples were not prepared from the same batch of 2.1 μm thick a-Si, i.e. they employed a slightly different beam current, sample holder, beam direction, and implantation temperature. Ion implantation is a complex and sensitive process, a small difference in the irradiation conditions could create such subtle differences and Raman measurements are sensitive to such small differences.

T (°C)	Set 1	Set 2
	RTA	Quartz Tube Furnace
no anneal	Raman	SIMS + Raman + Etch + Raman
150	Raman	-
250	Raman	SIMS + Raman + Etch + Raman
305	Raman	-
343	Raman	-
350	-	SIMS + Raman + Etch + Raman
400	Raman	-
425	Raman	-
443	Raman	-
450	-	SIMS + Raman + Etch + Raman
500	Raman	-
550	Raman	SIMS + Raman + Etch + Raman

Table 3.1: Summary of the condition of the two sets of the samples to study the effect of annealing and in-diffused hydrogen on the local ordering in ion-implanted a-Si.

Since set 2 is solely used to investigate the *relative* difference in the physical properties of a-Si due to in-diffused hydrogen, the difference in Γ/2(TO) between set 1 and set 2 is therefore not crucial as they are not directly compared with each other.

2. Amorphization by a pressure-induced structural collapse

PI a-Si was formed using the UMIS indentation instrument with a spherical diamond indenter of 20 μm radius at room temperature. On each sample, a large arrays of indents

was created on a single crystal Cz Si(100), p doped with boron to a resistivity of 10-20 Ωcm. Loading was performed to a maximum load of 700 mN with a constant rate of ~13.5 mN s^{-1} and unloading was performed within 1 s. The loading condition used to ensure that a large volume of metallic Si-II phase was created and no cracking occurred. Fast unloading guaranteed the formation of a-Si upon unloading. These samples were subjected to a series of isochronal annealing steps at various temperatures for 30 min using a quartz tube furnace in a nitrogen environment.

Upon annealing, the structural changes were analyzed by Raman spectroscopy using a x80 objective lens and an excitation wavelength of 632 nm from a He-Ne laser. The acquisition time of a single Raman spectrum was 30 s. Five spectra from five different indents on each sample were recorded and analyzed for each measurement.

The local ordering parameter $\Delta\theta$, ω(TO), and I(TA)/I(TO) were extracted from the measurements. In contrast to ion-implanted a-Si, Γ(TO), ω(TO), and I(TA)/I(TO) parameters of PI a-Si were obtained from fitting the TO and TA bands with the Lorentzian function using the package Origin [113]. The fitting procedure is discussed in detail in section 2.2.3. The bond-angle distortion was calculated using Eq. 2.12. The average values are presented together with the standard error.

3. Amorphization by re-irradiation of previously relaxed a-Si

a-Si structure	Preparation details
Crystalline precursor (X)	Implantation + annealed at 250°C, 350°C, and 450°C
CRN precursor (R)	Implantation + annealed at 450°C + Implantation + annealed at 250°C, 350°C, and 450°C

Table 3.2: Preparation details of the samples used to investigate the effect of the starting material on the relaxation process.

Two sets of samples of 800 nm thick a-Si were made using ion-implantation. The first sample set (X) was prepared by amorphizing a standard c-Si wafer using 80 and 500 keV Si ions with a fluence of 1×10^{15} (for preparation details see section 2.1.4). Isochronal annealing was conducted on the as-implanted samples for 30 min at various temperatures. The second set (R) was prepared using the previously fully relaxed (annealed at 450°C for 30 min) sample as the starting material and was irradiated under identical implantation conditions (fluence of 1×10^{15} using 80 and 500 keV Si ions). The conditions of the two sets of samples are summarized in table 3.2. Following re-irradiation, this sample set (R) was then also annealed at various temperatures for 30 min. In both cases, annealing was performed in a nitrogen environment using a quartz tube furnace. Upon annealing, the changes in the structure were analyzed using Raman spectroscopy with a 80x objective lens and an excitation wavelength of 632 nm from a He-Ne laser. The acquisition time of a single Raman spectrum was 30 s. Five spectra from different locations on each sample were

recorded and analyzed for each measurement. The average values are presented together with the standard error.

3.3 Short-range ordering of ion-implanted a-Si

Figure 3.1 shows the vibrational properties of as-implanted a-Si and a sample annealed at 550°C (only these two temperatures are shown for clarity). There is a clear decrease in the Γ(TO)/2 and an increase in I(TO) with annealing temperature. Furthermore, ω(TO), appears to shift to a higher wavenumber as has previously been observed by many authors [26, 46, 135, 136].

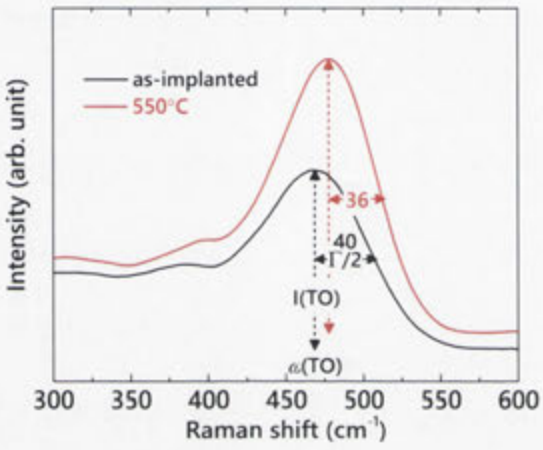

Figure 3.1: Typical TO bands for ion-implanted a-Si. The top spectrum from a sample that has been annealed at 550°C and the lower spectrum is from an as-implanted (unannealed) sample.

The change in the bond-angle distortion due to thermal annealing is analyzed by calculating the values of $\Delta\theta$ from Γ(TO)/2 measured in Fig. 3.1 (as detailed in section 2.2.3). The results are shown in Fig. 3.2 together with ω(TO) and I(TA)/I(TO). As can be seen in Fig. 3.2(a), the bond-angle distortion decreases with increasing annealing temperature suggesting that the structure becomes more ordered. Moreover, it is clear that the bond-angle distortion only changes slightly up to an annealing temperature of 300°C before it decreases progressively until it reaches ~9.3° at a temperature of 550°C. The small effect on the bond-angle distortion under low temperature annealing observed in this study suggests that the relaxation process in the low temperature regime might not be predominately due to rearrangement of the Si-Si network (which cannot be detected by Raman) but rather due to another mechanism, such as defect annihilation.

Roorda *et al.* [14] also observed a decrease in the bond-angle distortion of ~11.8° to ~8.8° upon annealing at 500°C for 45 min. It is important to note that these authors made their pure a-Si using different implantation parameters and a longer annealing time. In

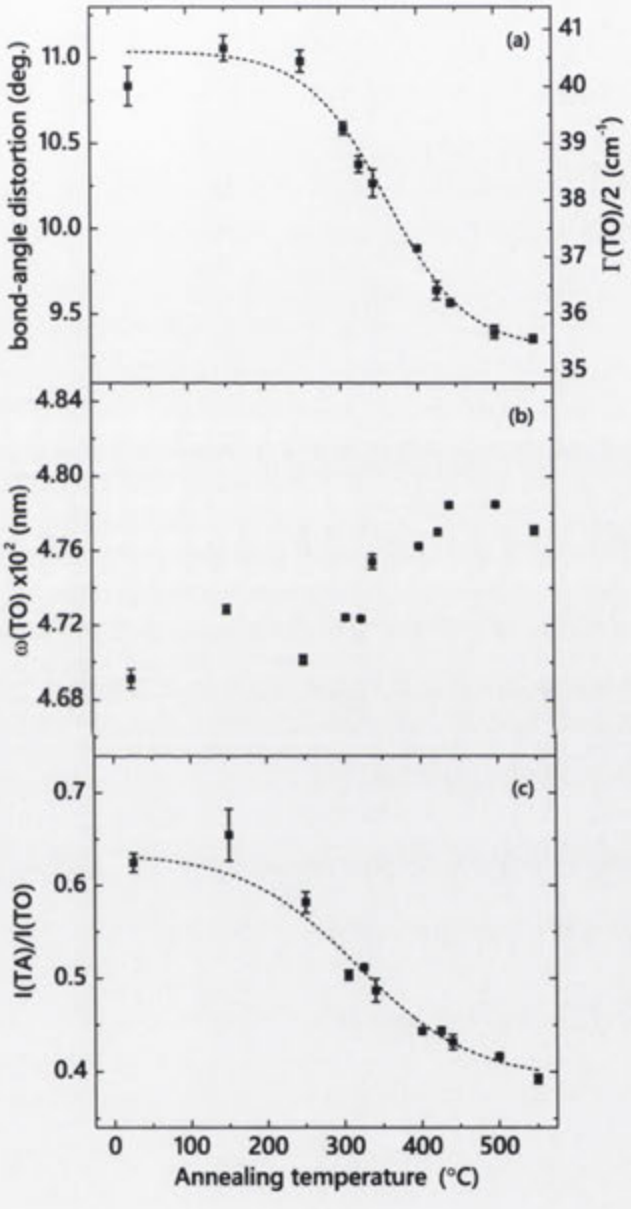

Figure 3.2: (a) The bond-angle distortion, (b) the position of the TO band, and (c) the ratio of the intensity of the TA to TO band of samples annealed at various temperatures. The dashed lines are guides for the eye only.

another study, Laaziri, *et al.* [15] measured a $\Delta\theta$ of $\sim$10.4° for as-implanted and $\sim$9.6° for fully relaxed a-Si (annealed at 600°C for 1 hour). The latter study was carried out using XRD on a-Si membranes (hence epitaxial crystallization did not occur during annealing at 600°C for 1 hour). Thus, the bond-angle distortion obtained in the present study falls within the range of previous works and is thus entirely consistent with what others have obtained.

Figures 3.2(b) and (c) confirm that the network is indeed progressing toward a more ordered structure. This is shown by a shift in ω(TO) to a higher wavenumber accompanied by a decrease in I(TA)/I(TO) as the annealing temperature is increased.

It is interesting to compare the progression of $\Delta\theta$ and I(TA)/I(TO) during relaxation. Despite sharing roughly the same onset temperature of 300°C, it is observed that I(TA)/I(TO) has a slower rate compared to $\Delta\theta$. This might indicate that short-range ordering (and thus reduction in $\Delta\theta$) takes place first, followed by ordering of the dihedral-angle (rearrangement of the Si atoms) during structural relaxation. Alternatively, the rearrangement of the Si atoms and the reduction in the bond-angle distortion occur simultaneously, but the rearrangement of the Si atoms takes a longer time compared with reduction in the bond-angle distortion.

In this study, The minimum bond-angle distortion of $\sim$9.3° appears to signify the maximum network relaxation which can be experimentally obtained for a 30 min anneal before epitaxial crystallization occurs at higher temperatures [137]. This raises the question as to whether a lower bond-angle distortion could be obtained by annealing the sample for a longer annealing time. An independent experiment was performed to answer this question. This is discussed in the following section.

3.4 The effect of annealing time on the bond-angle distortion

The progression of the bond-angle distortion with annealing time for samples annealed at various temperatures is shown in Fig. 3.3. For all annealing temperatures, it is observed that the major decrease in the bond-angle distortion occurs below 30 min of annealing time (see Fig. 3.3(b), then reaches its equilibrium and stays relatively constant for the remaining time. The results show that isothermal annealing for as long as 960 min is not able to lower the bond-angle distortion significantly at any annealing temperature.

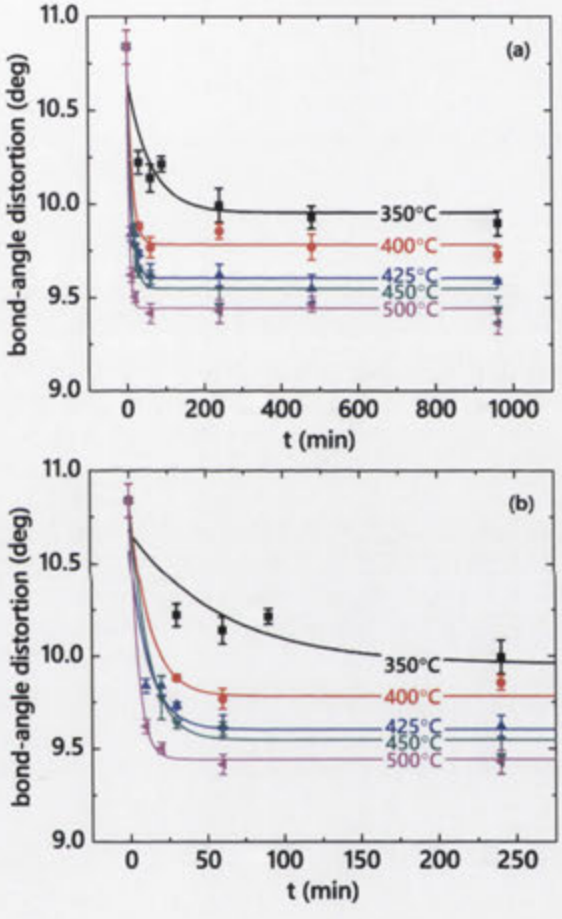

Figure 3.3: The progression of the bond-angle distortion from (a) 0 to 960 min, and (b) 0 to 250 min. The solid lines are guides for the eye only

3.5 Influence of hydrogen in the local ordering

As detailed in section 2.2.2, the concentration of in-diffused hydrogen in a-Si can be quantified using SIMS. Figure 3.4(a) shows SIMS depth profiles of the hydrogen concentration as a function of depth for five a-Si samples that were subjected to various annealing temperatures. SIMS data shows that, upon annealing at low temperature, such as 250°C, hydrogen starts to diffuse from the air into the sample and reaches a concentration in the order of 10^{20} cm^{-3} at the surface and decreases to 10^{19} cm^{-3} (which is the detection limit of the SIMS) by 250 nm. Interestingly, above 250°C the concentration of hydrogen decreases with increasing annealing temperature. This behavior is due to activation of defect annihilation (recombination) at higher temperatures, which reduces the trapping sites for hydrogen atoms in the network. The hydrogen completely diffuses out from the sample upon annealing at 450°C. This is shown at a depth of 25 nm in Fig. 3.4(b).

The effect of hydrogen on the structural order during the structural relaxation process was then investigated in detail by measuring $\Delta\theta$, ω(TO), and I(TA)/I(TO) before and after removal of the hydrogen-rich surface region from the sample.

T (°C)	a-Si un-etched $\Delta\theta$ (deg)	a-Si etched $\Delta\theta$ (deg)
no anneal	11.57±0.05	11.45±0.04
250	10.70±0.06	10.70±0.05
350	10.15±0.07	10.12±0.04
450	9.64±0.03	9.55±0.06
550	9.23±0.04	9.38±0.03

Table 3.3: The bond-angle distortion before and after removal of the hydrogen-rich surface region for sample annealed at various temperatures.

The comparison of the bond-angle distortion before and after removal of the hydrogen-rich surface region is summarized in table 3.3 and in Fig. 3.5(a). Interestingly, relatively small differences in the bond-angle distortion after removing the hydrogen-rich region are observed for all annealing temperature. Furthermore, it is clear from Fig. 3.5(b) that the position of the TO band stays roughly within the same value with the introduction of hydrogen into the network. This indicates that in-diffused hydrogen does not significantly induces local (short-range) ordering in the network. Indeed, it has previously been reported by Sokolov *et al.* [53] that the introduction of hydrogen atoms only has a weak effect on the short-range ordering but a significant influence on the structural order at intermediate-range scales [53]. This affect is investigated further by examining the intensity ratio of the TA to TO band. As detailed in 1.2.1, the TO band is affected by the bond-stretching vibrations, while the TA band is related to bond-bending modes which involves the entire tetrahedra of Si atoms. Therefore, the relative area of the TA and TO band could provide information on the role of hydrogen on bending and stretching modes of Si. Since the bond-angle distortion essentially does not change with annealing temperature with

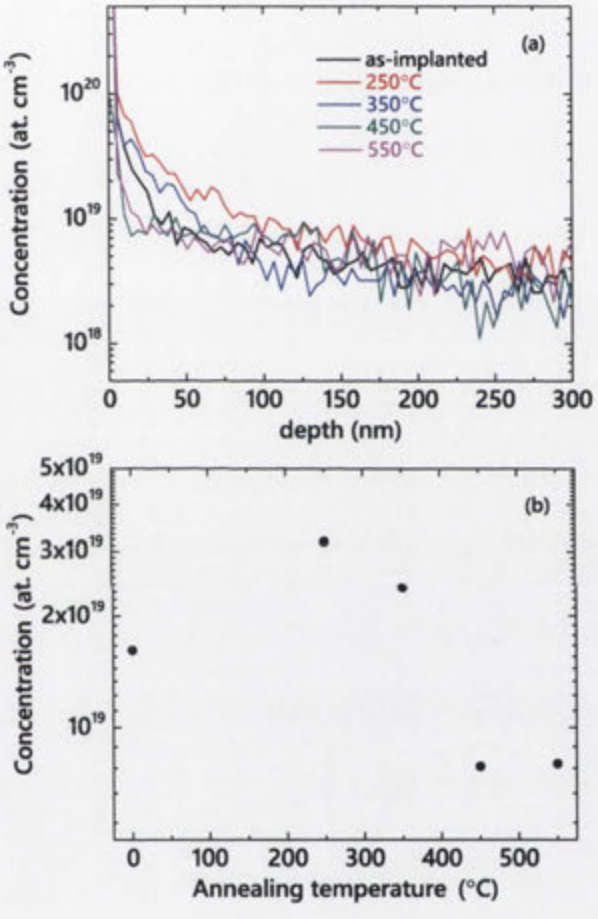

Figure 3.4: (a) The SIMS depth profile of the hydrogen concentration as a function of depth for five samples that were subjected to various annealing temperatures, and (b) hydrogen concentration as a function of annealing temperature at a depth of 25 nm.

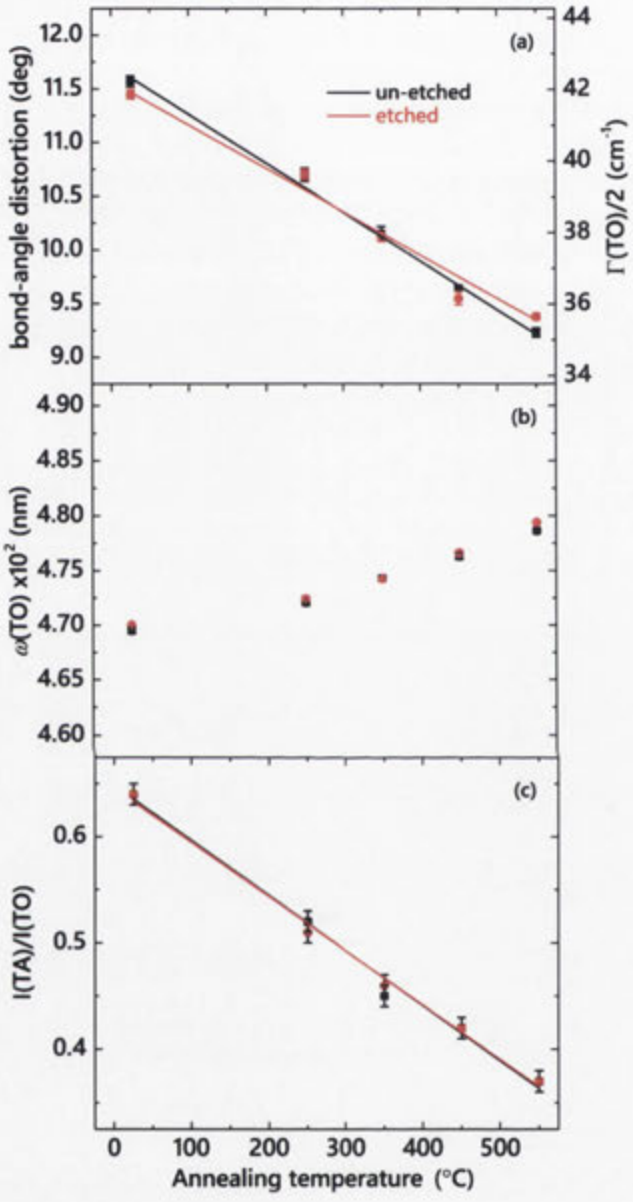

Figure 3.5: Comparison of the (a) bond-angle distortion, (b) position of the TO band, and (c) intensity ratio of the TA to TO band before (black solid square) and after (red solid circle) removal of the hydrogen-rich surface region. The solid lines are guides for the eye only.

the introduction of hydrogen, the effect of hydrogen on intermediate-range scale can be estimated from the intensity ratio of the TA to TO band. The calculated intensity ratio of the TA to TO band is plotted in Fig. 3.5(c). It is clear from the plot that there is no appreciable difference in the intensity ratio of the TA to TO band with the introduction of hydrogen. This suggests that in-diffused hydrogen during annealing does not significantly induces ordering in the network on an intermediate-range scale.

In general, the variation in the local ordering parameters obtained indicates clearly that short- and intermediate-range ordering in the a-Si network are not significantly modified by the addition of the hydrogen through thermal annealing.

3.6 Short-range ordering of PI a-Si

The local ordering parameters obtained by Raman spectroscopy for PI a-Si are presented below. The vibrational properties of as-indented a-Si and a sample annealed at 500°C (only these two temperatures are shown for clarity) are shown in Fig. 3.6. It is observed that the Raman active volume is deeper than the a-Si depth in the indent. Hence, a dc c-Si band appears in the PI a-Si spectrum. The intensity of the c-Si TO band increases with annealing temperature. This could be due to an increase in ordering of the a-Si network (and consequential decrease in absorption within a-Si) and/or a decrease in the volume of a-Si due to epitaxial regrowth.

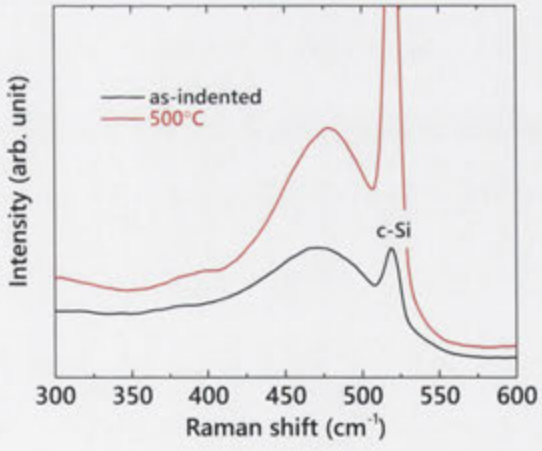

Figure 3.6: Typical TO bands for PI a-Si. Top spectrum is from a sample that has been annealed at 500°C, and the lower spectrum is from an as-indented (unannealed) sample.

Figure 3.6 shows that the TO band appears narrower after thermal annealing, indicating a decrease of Γ(TO). An increase in I(TO) and a shift of ω(TO) to a higher wavenumber with annealing temperature is also observed. This behaviour is investigated in detail by extracting $\Delta\theta$, ω(TO), and I(TA)/I(TO) from Fig. 3.6 (as detailed in section 2.2.3). The results are shown in Fig. 3.7 together with the local order parameters obtained from the

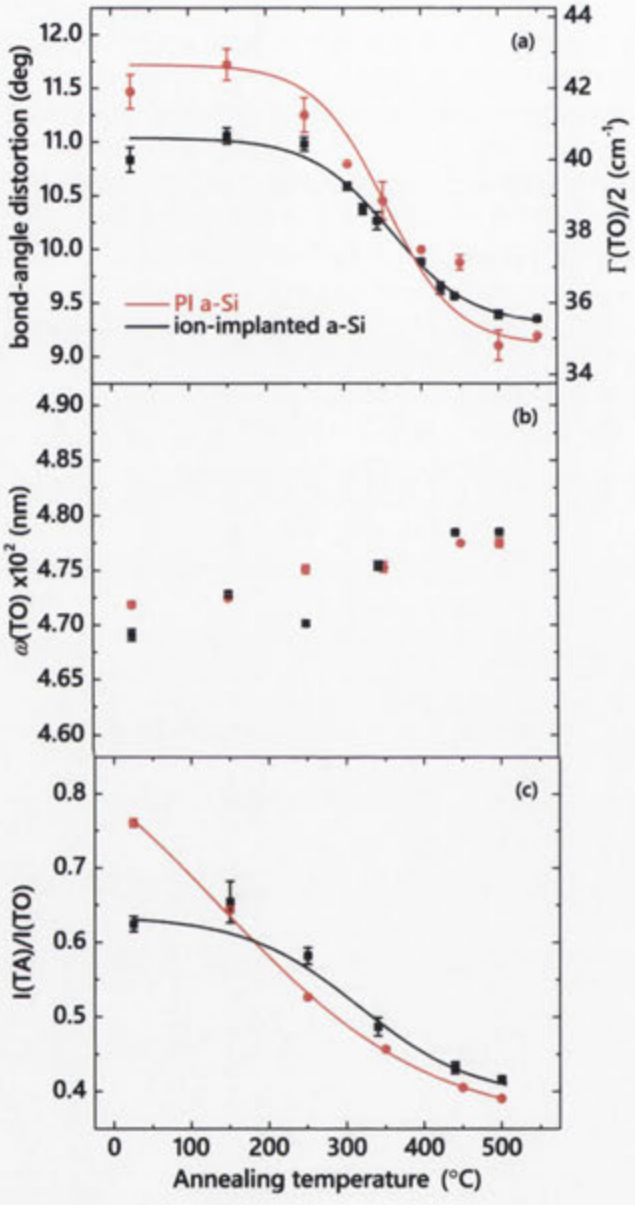

Figure 3.7: (a) The bond-angle distortion, (b) ω(TO), and (c) I(TA)/I(TO) of the PI a-Si sample (red solid circle) annealed at various temperatures. The variation of the local order parameters obtained from ion-implanted a-Si (black solid square) is also shown for comparison. The solid line are guides for the eye only.

ion-implanted a-Si in section 3.3 for comparison.

The thermally-induced behavior of PI a-Si from as-indented to relaxed states shows that different amorphous states also exist in this form of a-Si. Figure 3.7 shows that the bond-angle distortion only changes slightly up to an annealing temperature of 300°C before it decreases progressively until it reaches ~9.2° at a temperature of 500°C. The decrease in the bond-angle distortion indicates that the structure converging to a more ordered network (CRN). The progression of the structure to a more ordered network is also reflected by an increase in the ω(TO) and a decrease in the I(TA)/I(TO). This result bears a remarkable similarity to ion-implanted a-Si. They both follow the same trend and within experimental uncertainty they both reach the same $\Delta\theta$, ω(TO), and I(TA)/I(TO) after annealing at 500°C. This suggests that the short-range order of both forms of a-Si is the same in the fully relaxed state.

Measurements on as-prepared ion-implanted and PI a-Si, however, show intriguing differences. In comparison with as-implanted a-Si, as-indented a-Si has a higher $\Delta\theta$ and I(TA)/I(TO). These differences clearly reflect structural differences, which presumably arise from the different preparation method: one formed from ion disordering of crystalline Si and the other from the transformation of a dense metallic Si-II phase. The formation of the amorphous phase from the high density Si-II phase, which is 22% denser than dc-Si (c-Si), makes the formation of PI a-Si fundamentally different from the formation of ion-implanted a-Si. In the former case, the long-range order of the crystalline Si-II is lost due to rapid unloading, but the PI a-Si may retain a more compact structure with a slightly higher density to *normal* a-Si, as well as containing many strained bonds [133]. In the ion-implanted case, however, the long-range order of crystalline Si is lost due to collision cascades caused by energetic Si ions [90], a process that leads to a structure with a large number of defects, and defect complexes such as dangling bonds [28], and vacancy-type defects [67]. These defects may aid the formation of an amorphous structure with a lower energy state (and thus a lower bond-angle distortion).

A previous electron diffraction study [133] on both forms of a-Si shows that in the as-prepared state, PI a-Si has a larger spread in the bond-length than ion-implanted a-Si. This may suggests that PI a-Si has a larger fluctuation in the density of the dihedral-angle in the network compared to ion-implanted a-Si to compensate for having a larger bond-angle distortion; PI a-Si has less order than ion-implanted a-Si in the intermediate length scale. Hence, the I(TA)/I(TO) for PI a-Si is higher than ion-implanted a-Si as observed by Raman spectroscopy.

It is also interesting to link the reduction in the bond-angle distortion with I(TA)/I(TO) during annealing for both forms of a-Si. Figure 3.7 shows that in the ion-implanted a-Si, both bond-angle distortion and I(TA)/I(TO) only change slightly during low temperature anneals. For the PI a-Si, however, it is observed that I(TA)/I(TO) significantly decreases during low temperature anneal suggesting that ordering of the dihedral-angle takes places prior to a reduction in bond-angle distortion.

Regardless of the mechanism of structural relaxation, PI a-Si clearly undergoes ordering to the same disordered state as observed for fully relaxed ion-implanted a-Si and thus also converges to a CRN.

3.7 Short-range ordering of re-irradiated a-Si

The ideal CRN for ion-implanted a-Si is a fully four-fold coordinated, nonperiodic structure that is metastable with respect to c-Si and is constructed primarily from five-, six- and seven-membered rings [9]. It has been subsequently demonstrated that this model matches experimental diffraction data and is thus accepted as a good description of the structure of a-Si [12]. Alternatively, another model for a-Si, namely the paracrystallite model has also been proposed by Hosemann and Baggchi [41] and Treacy *et al.* [138]. In this model, a paracrystalline structure is a disordered network with topologically crystalline grains of length scales 1 to 2 nm (MRO).

The authors [35, 38] who propose a paracrystalline model for ion-implanted a-Si argue that paracrystallinity is a reasonable model since the starting structure is crystalline (before irradiation) and following amorphization the model suggests a *memory* of prior crystalline structure. In this section, this hypothesis will be addressed using a fully relaxed a-Si as a starting structure, which to most authors [35, 38] contain no significant paracrystallinity, and subsequently re-irradiating it. Hence the re-irradiated (of previously relaxed) sample might be expected not to exhibit paracrystalline behavior. This is examined by measuring the influence of thermal annealing in the local ordering using Raman spectroscopy to compare with irradiated c-Si.

The local order parameters for sample X and R (re-irradiated) annealed at various temperatures are shown in Fig. 3.8. Figure 3.8 shows that upon annealing at various temperatures both samples progressed toward a more ordered network. This is reflected by a decrease in the bond-angle distortion, and a shift in ω(TO) to a higher wavenumber accompanied by a decrease in I(TA)/I(TO) as annealing temperature is increased. A remarkable similarity in the local ordering (within experimental uncertainty), including dihedral-angle (I(TA)/I(TO)) which in some extent reflects the medium-range order, between re-irradiated a-Si and ion-implanted a-Si shows that re-irradiated a-Si was able to return to an equivalent amorphous state for all annealing temperatures.

The ability for the re-irradiated a-Si to return to its as-implanted state is indeed insufficient to eliminate the possibility of paracrystallinity, but it clearly disproves the hypothesis that the ordering in the ion-implanted a-Si is related to the starting Si crystal. If the starting structure was responsible for the symmetry in the as-implanted state, the ordering of ion-implanted a-Si and re-irradiated a-Si, as reflected by bond-angle distortion and dihedral-angle, would have been different. The similarity in the reduction of the bond-angle and dihedral-angle of ion-implanted a-Si and re-irradiated a-Si upon annealing indicates that the short-range order increases, which in turn implies that medium range

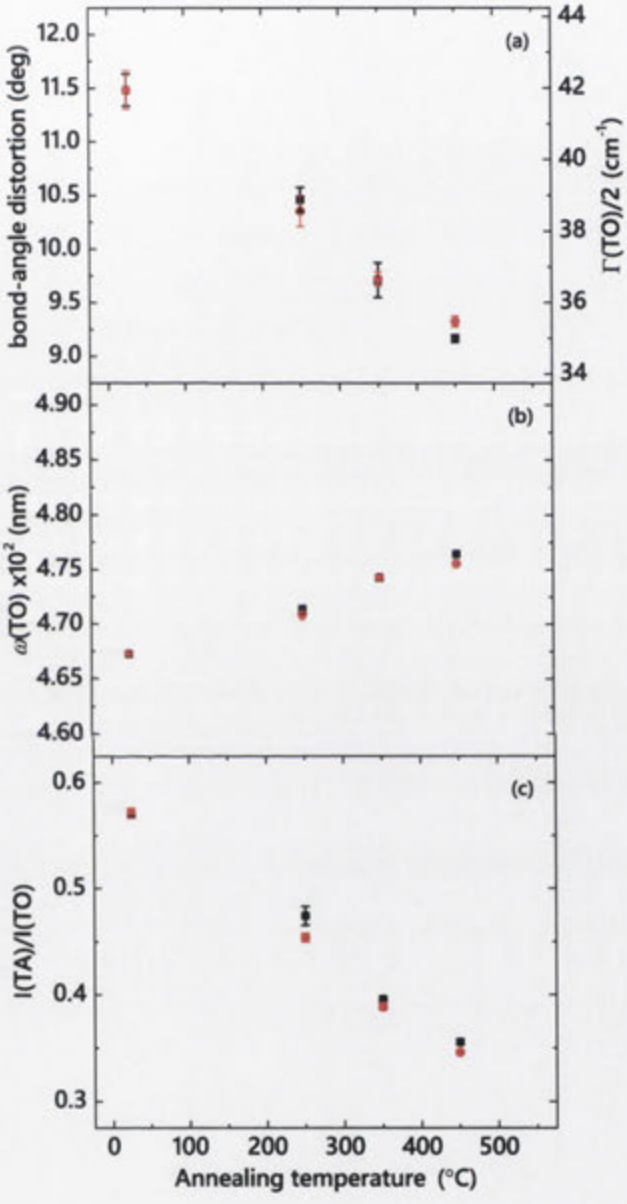

Figure 3.8: Comparison of the (a) bond-angle distortion, (b) position of the TO band, and (c) intensity ratio of TA to TO band for sample X (black solid square) and R (red solid circle).

order increases. Hence paracrystallinity may not be significant in the a-Si formed by irradiation of c-Si. However, techniques (such as FEM) that specifically probe MRO would be needed to verify this assertion.

3.8 Summary

Thermal annealing experiments reveal a decrease in the Si-Si network strain toward a more ordered network. The bond-angle distortion decreases from an as-implanted value of ~11 to ~9.3° at a temperature of 550°C. It was found that the bond-angle distortion changed significantly in a very narrow temperature range of 300 to 340°C.

Although hydrogen in-diffuses during annealing and will most certainly be responsible for passivating defects by the formation of $Si_{1-x}H_x$ bonds, Raman spectroscopy shows no significant contribution of hydrogen toward the relaxation processes in ion-implanted a-Si.

The local ordering PI a-Si has been investigated in some detail and comparison has also been made with ion-implanted a-Si. In comparison with ion-implanted a-Si, PI a-Si is a less ordered structure in its as-prepared form. However, both forms of a-Si result in the same short-range ordering (minimum bond-angle distortion) in the fully relaxed state. This indicates that regardless of the preparation techniques, thermal relaxation of impurity-free a-Si leads to the same amorphous state.

In contrast to ion-implanted a-Si, it is observed in PI a-Si that reduction in the fluctuation of the density of the dihedral-angle, I(TA)/I(TO), occurs without a significant change in the bond-angle distortion. This difference reflects a clear difference in the mechanism of the structural relaxation. It appears that, in PI a-Si, the ordering of the dihedral-angles takes places prior to ordering of the bond-angles.

The short-range ordering as obtained from Raman in the as-implanted a-Si is reproducible upon re-irradiation of previously relaxed ion-implanted a-Si. Indeed, the relaxation process from both sample sets appears to be similar and the re-irradiated sample is able to return to its original amorphous state at each annealing temperature. This clearly disproves the hypothesis that the medium-range order in the ion-implanted a-Si is related to the starting Si crystal.

The implication of the Raman data in terms of the entire relaxation process of ion-implanted a-Si will be discussed later, following the presentation of other structural data.

4

Pressure-induced phase transformations

4.1 Introduction

Ion-implanted a-Si deforms in one of two methods, either via plastic deformation (simple plastic flow) or a series of phase transformations during indentation. Plastic deformation is facilitated by the presence of defects and broken bonds in the network [47,66,139]. During the structural relaxation process, such defects are removed and broken bonds (or dangling bonds) are repaired. The relaxed structure then forms a more rigid (4-fold-coordinated, covalently bonded) network which allows the pressure to increase sufficiently under the indenter tip to cause the a-Si to transform to the denser metallic Si-II phase.

Unrelaxed a-Si is known to deform via plastic flow if the material is unconstrained. It should be noted, however, that unrelaxed a-Si can be forced to phase transform if the material is confined in some way. This can be achieved under certain indentation conditions when the penetration depth of the tip approaches or exceeds the film thickness. In this case, the confinement of the layer between the indenter and underlying c-Si can lead to the phase transformation of the unrelaxed film [66]. In contrast, relaxed a-Si (annealed at 450°C for 30 min has been reported to deform readily via phase transformation to a metallic Si-II phase during loading, with further transformations occurring on pressure release to a mixture of high pressure crystalline phases Si-III (bc8) and Si-XII (r8). Notably, Haberl *et al.* [66] have reported that relaxed a-Si (which has transformed to Si-II on loading) undergoes a phase transformation to the crystalline phases Si-III/XII on unloading using a slow unloading rate, in a process that is almost identical to indentation-induced deformation of c-Si. These two very different deformation mechanisms of unrelaxed and relaxed

a-Si thus provide a relatively simple method to probe the state (whether the structure is unrelaxed or relaxed) of a-Si.

The distinct difference in the mechanical response of a-Si under indentation can be easily identified from the P-h curve due to the occurrence of a sudden discontinuity in the unloading segment of the P-h curve known as a pop-out event. It has been reported that the pop-out event is caused by a sudden transformation of Si-II to Si-III/XII due to the change in the density of these structures (Si-II is 22% denser than dc-Si, whereas Si-III/XII is only around 10%) [66]. However, the appearance of the pop-out in the P-h curves can be subtle and slightly ambiguous. Thus, in this study Raman spectroscopy is also used to detect the end phases within the residual indents.

In addition, the presence of impurities, such as hydrogen has been reported to affect the ability of ion-implanted a-Si to undergo phase transformations on unloading. This is thought to occur by inhibiting the growth rate of Si-III/XII during unloading [140].

In this chapter, the state (whether unrelaxed or relaxed) of a-Si is determined based on the material's ability to phase transform under applied pressure. The effect of in-diffused hydrogen on the phase transformation behavior is also investigated using similar methodologies.

4.2 Experimental

The deformation behavior of ion-implanted a-Si was investigated using the UMIS indentation instrument as detailed in section 2.2.4. Indentation was performed at room temperature on the 2.1 μm thick a-Si samples (set 1 as detailed in section 3.2), that were subjected to a series of various annealing temperatures for 30 min, using a 4.3 μm spherical diamond tip. Loading was performed to a maximum load of 80 mN with a constant rate of $\sim$0.9 mN s^{-1} for loading and unloading in a continuous load cycle. This set of parameters has a 100% probability of a phase transformation to Si-III/XII for fully relaxed a-Si (annealed at 450°C for 30 min. As the pop-out behavior is a stochastic event (based on the nucleation of the Si-III/XII on unloading), a statistically significant number of trials (between 49 to 100) was performed for each sample.

Raman spectroscopy with a x80 objective lens and excitation wavelength of 632 nm from a He-Ne laser was used to probe the residual indent impression following indentation, to detect the end phases and to confirm the relation between phase transformation and pop-out event. The recording time of a single Raman spectrum was 30 s.

As detailed in section 3.5, upon annealing, the in-diffused hydrogen in the sample has a concentration in the order of 10^{20} cm^{-3} at the surface, decreasing to 10^{19} cm^{-3} at a depth of 250 nm. The hydrogen-rich surface region was chemically removed from the surface of the samples using a chemical etch solution (HNO_3+HF+H_2O) for 15 to 20 s. The effect of in-diffused hydrogen during annealing on the phase transformation behavior was investigated by performing indentation (on the 2.1 μm thick a-Si samples

set 2 as detailed in section 3.2) before and after removing the hydrogen-rich surface region from the samples. The same indentation condition as detailed above was used. Raman spectroscopy was again performed to detect end phases beneath the indents in both cases.

4.3 Probability of phase transformation

Figure 4.1 shows typical examples of P-h curves obtained from indentation tests in a-Si. The tip penetrated less than a quarter of the film thickness, thus the deformation behavior of the a-Si film is not influenced by the underlying c-Si substrate [141]. The results presented are for samples that have been annealed at 300 and 340°C.

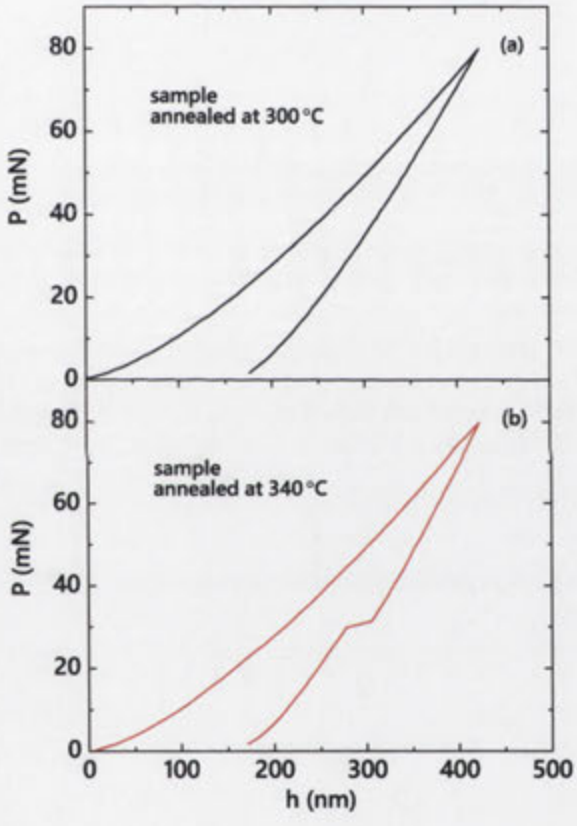

Figure 4.1: Load-depth (P-h) curves of indentation performed on an ion-implanted sample annealed at (a) 300°C, and (b) 340°C.

The absence of a pop-out event in the unloading segment for the sample annealed at 300°C almost certainly indicates that no phase transformation has occurred; therefore deformation took place via a simple plastic flow mechanism. In this case, out of 49 indents measured, none showed any pop-out event. However, a pop-out event appears in the unloading segment for the sample annealed at 340°C, indicating that the a-Si underwent a phase transformation. In this case, the appearance of a pop-out event was observed in the unloading segment of **all** of the 49 indents studied. Indeed, unlike the sample that has

been annealed at 300°C, Raman spectra of the indents in the sample annealed at 340°C show additional Raman bands at 163 cm^{-1}, 350 cm^{-1}, 382 cm^{-1}, 395 cm^{-1}, and 434 cm^{-1}, as shown in Fig. 4.2. These bands are attributed to the presence of Si-III/XII [142]. This confirms that phase transformation occurs in the 340°C sample but not the 300°C sample.

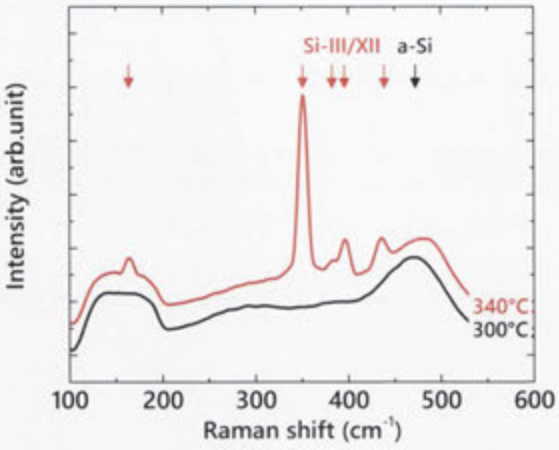

Figure 4.2: Raman spectra of an indent in ion-implanted a-Si annealed at 300°C, and 340°C.

Interestingly, as shown in Fig 4.3, samples annealed at 325°C display both types of deformation behaviors, with 10 out of 49 indents deforming via plastic flow and the remaining 39 via phase transformation. Thus, there exists a temperature regime where the state of partly relaxed a-Si may either deform plastically or undergo phase transformation.

The state of a-Si was statistically determined from the portion of indents that had phase transformed. This portion is stated as the probability of the formation of Si-III/XII (pt); a probability of 0 means that phase transformation never occurs and a probability of 1 means that phase transformation occurs in all indents. Raman spectroscopy was used to confirm the end phases following indentation in all cases. Note that there was a perfect correlation between the observation of pop-out events in the unloading curves and the presence of the Si-III/XII phases in the indents.

The probability of phase transformation for samples annealed at various temperatures is shown in Fig. 4.4. Two clear regimes are observed. (1) At temperatures up to 300°C, the probability for a pop-out event and hence pt is 0. Thus, up to 300°C the sample always deforms via plastic flow under the indentation conditions used in this study, (2) For 340°C and above, indentation always induces a pop-out event and the probability of pt is therefore 1 in this case. At annealing temperatures between 300 and 340°C, the probability of phase transformation is between 0 and 1. For instance, at 315°C 0.18 of the indents examined had phase transformed, and this portion increases with annealing temperature.

The ability of a-Si to undergo phase transformation from Si-II to Si-III/XII under

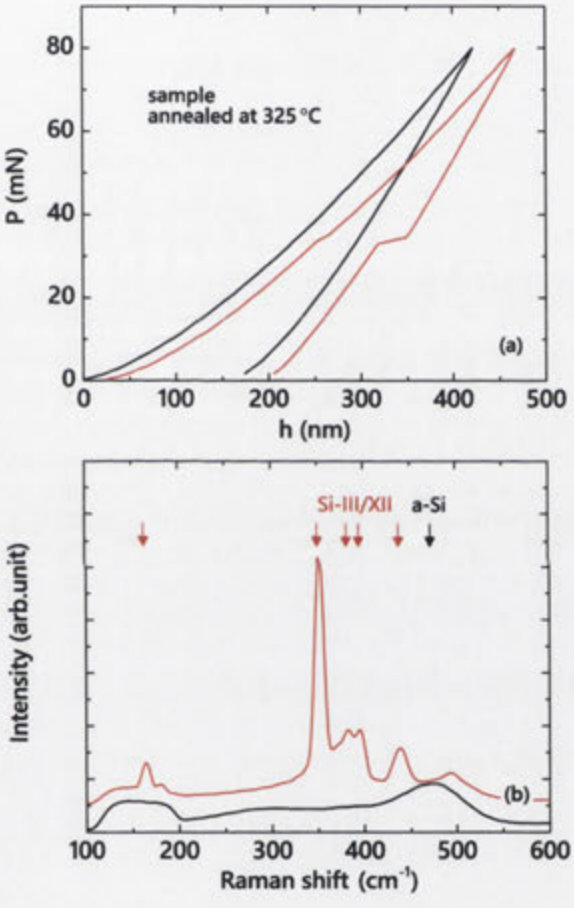

Figure 4.3: a) load-depth (P-h) curves of indentation performed in ion-implanted a-Si annealed at 325°C, and (b) Raman spectra of the respective indents.

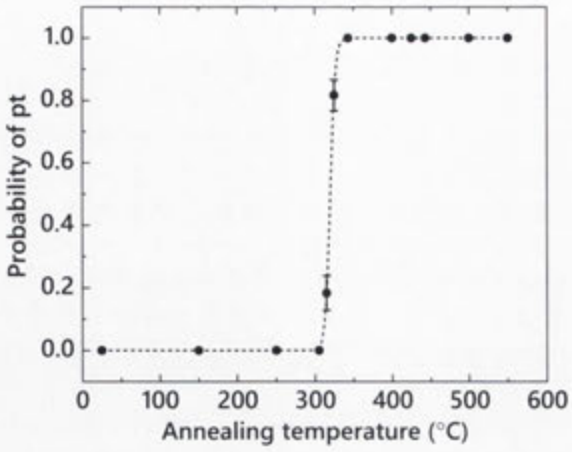

Figure 4.4: The probability of pressure-induced phase transformation in ion-implanted a-Si annealed at various temperatures using a 4.3 μm spherical diamond tip, and maximum load of 80 mN with a constant rate of $\sim$0.9 mN s^{-1} for loading and unloading in a continuous load cycle.

applied pressure, between 300 and 340°C, appears to indicate a transition point where the partially relaxed a-Si undergoes phase transformation.

4.4 Effect of loading/unloading rates

The previous section showed a correlation between the ability of the material to deform via a simple plastic flow mechanism during indentation and the annealing temperature (thus avoiding phase transformation). Therefore, it would be interesting to see if the anneal temperature where pop-outs begin to appear (i.e. 300°C) depends on the loading and/or unloading rate. If indeed the relation between plastic flow and no pop-out holds, it may be expected that slowing the loading rate down by a factor of 10 would lead to a higher or lower temperature transition where partially relaxed a-Si undergoes phase transformation.

Note that, since a pop-out is the result of a rapid phase growth, this process requires time to both generate sufficient nucleation sites and to allow the crystallites to grow. Therefore a lower (or slow) unloading rate is known to promote a pop-out event. The slow unloading rate chosen in this study was accordingly selected so that Si-II was guaranteed to phase transform to Si-III/XII upon unloading.

As shown in Fig. 4.4, the deformation mechanism of a-Si under applied pressure depends on its *degree* of relaxation. In the case of unrelaxed a-Si, a slow loading rate will provide enough time for the defects in the structure to become mobile and to promote plastic deformation. Thus, it seems reasonable to speculate that sufficiently fast loading rates may totally inhibit plastic flow thus always promoting phase transformation. Alternatively, if loading is extremely slow phase transformation may be inhibited. Therefore, it

was decided to alter the loading rate to confirm this hypothesis.

The loading rate was changed from 0.9 mN s^{-1} to 0.09 mN s^{-1} and 9 mN s^{-1}, while keeping the unloading rate constant. The indentation tests were performed on the sample annealed at 325°C. This sample was selected because it represents a partially relaxed state that has a probability of phase transformation between 0 and 1 for the loading rate of ~0.9 mN s^{-1} shown in Fig. 4.4.

The P-h curves and Raman analysis of these indents show that out of 49 indents, 100% deform via phase transformation at a higher loading rate. In contrast, under the slower loading rate, 0% phase transform. This result would seem to support the explanation that under fast loading, plastic flow cannot occur fast enough to prohibit the applied pressure from exceeding the transformation pressure needed for a-Si to phase transform. In contrast, slower loading rates provide sufficient time for defect mobility in the a-Si, and promotion of plastic deformation. Thus, it is clear that, for annealing temperatures where considerable bond angle distortion remains in the sample according to Fig. 3.2, the a-Si is still able to phase transform over a range of loading rates. However, it is worth noting that it may be possible that under a fast enough loading rate, a-Si would always transform to Si-II, and that Si-II would never form under slower loading rate. Thus, phase transition of a-Si from a partially relaxed state may not be identifiable if such extremes were used.

4.5 Effect of hydrogen on the phase transformation behavior

The effect of in-diffused hydrogen on the phase transformation behavior is investigated by comparing the ability of a-Si to undergo a phase transformation to Si-III/XII before and after removing a hydrogen-rich surface region from the sample, as detailed in section 4.2.

T (°C)	a-Si un-etched probability of p.t	a-Si etched probability p.t
no anneal	0	0
250	0	0.65±0.07
350	1	1
450	1	1
550	1	1

Table 4.1: The probability of phase transformation of ion-implanted samples annealed at various temperatures before and after hydrogen removal.

The probability of phase transformation for samples annealed at various temperatures before and after the removal of the hydrogen-rich surface region is summarized in table 4.1. This table shows that, for relaxed a-Si (annealed at temperature above 350°C), the removal of in-diffused hydrogen has no effect on the ability of the a-Si to phase transform to Si-III/XII. However, for the sample annealed at 250°C, the removal of hydrogen appears

to **increase** the probability of phase transformation, a somewhat surprising result.

The possible role of in-diffused hydrogen in this result is investigated, where, at first sight, it would appear that the removal of hydrogen increases the probability of phase transformation. On the other hand, the deformation mechanism of plastic flow in a-Si (as detailed in section 4.1) appears to be associated with the presence of a high density of dangling bonds in the structure. Are these two proposals compatible? This is explored below.

Upon subsequent thermal annealing at 250°C, as shown in Fig. 3.4, hydrogen is found to diffuse into the a-Si, probably via a trapping/detrapping mechanism associated with the OH/H_2 transformation of hydrogen bonds. For a concentration below 3 at.%., in-diffused hydrogen is expected to bond to Si in a monohydride configuration (Si-H) [129], thus decreasing the density of the dangling bonds in the structure. The formation of Si-H bonds results in a hydrogen-passivated structure and thus should increase its resistance to plastic deformation [143], thus promoting deformation via phase transformation over plastic flow. The fact that the un-etched sample annealed at 250°C before hydrogen removal has a phase transformation probability of 0 implies that the density of the dangling bonds in the structure that are not bonded to hydrogen is enough to facilitate the deformation of simple plastic flow.

The hydrogen-rich region of the sample annealed at 250°C was chemically removed from the surface using a dilute HF solution (HNO_3+HF+H_2O). The HF-etched silicon surface has been previously studied in detail under a variety of techniques, such as surface infrared spectroscopy [144, 145]. It has been shown that HF-etched Si surfaces are microscopically rough, a Si(100) wafer etched in 7:1 buffered HF solution for 10 min increased its root mean square (RMS) surface roughness from 0.2 nm to 0.5 nm [146], with coupled monohydride, dihydride, and trihydride termination. At room temperature, since all surface Si atoms are fully coordinated, the hydrogen termination surface is completely stable in clean gaseous environments even at atmospheric pressures [147]. This layer may also serve as a effective chemical barrier to prevent further hydrogen diffusion into the bulk [148]. A similar behavior for a-Si is thus expected.

Figure 4.5 shows the SIMS depth profile of the hydrogen concentration as a function of depth for as-implanted a-Si and the sample annealed at 250°C before and after hydrogen removal. The SIMS data show that chemically removing the hydrogen-rich region after annealing leads to a decrease in the concentration of the hydrogen by one order of magnitude. This value is even lower than the one for the as-implanted sample, suggesting that the hydrogen terminated surface is indeed preventing further hydrogen diffusion into the bulk, leading to a hydrogen-free (unpassivated dangling bond) bulk structure. Therefore, it should be expected that the etched sample contains a higher density of dangling bonds compared with the un-etched sample. Hence, deformation via plastic flow might be expected to be more favorable in the etched sample. However this proposition is in contrast to the result observed, with the etched sample under going higher probability of phase

transformation compared to the un-etched sample. Therefore, this does not support the simple explanation of hydrogen inhibiting phase transformation.

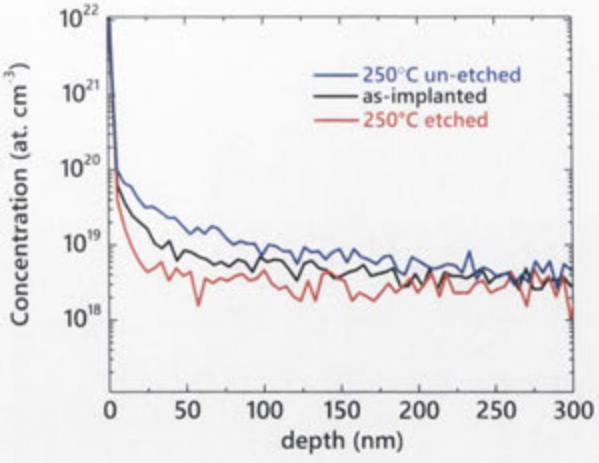

Figure 4.5: The SIMS depth profile of hydrogen concentration as a function of depth for for as-implanted a-Si and sample annealed at 250°C before and after hydrogen removal.

The discrepancy could instead be explained by considering the effect of the etching process on the surface morphology and roughness. As previously mentioned, hydrogen terminated c-Si surfaces are microscopically rough after being etched in a HF solution. This effect was further investigated in this study by performing roughness analysis on the a-Si surface using atomic force microscopy (AFM). The surface roughness was measured in contact mode. It was found that the RMS surface roughness of the sample increased from ~0.3 (un-etched) [149] to ~7 nm (etched). As illustrated in Fig 4.6, the contact area marked by arrows will experience higher pressures than other contact regions under the same (average) applied load due to surface roughness [150, 151]. This local pressure may tend to force the a-Si (in the contact area marked by arrows) to phase transform to metallic Si-II phase, which would then act as nucleation sites for further transformation to Si-III/XII during unloading.

It may be expected that the surface roughness will affect the ability of a-Si to phase transform for all annealing temperatures. However, this may only be manifested in temperature regions where the influence of surface effects is dominant over dangling bonds, such as 250°C.

In summary, the removal of hydrogen-rich regions from the samples has no significant effect on the ability of the a-Si to undergo phase transformation, except for the increased probability of phase transformation observed in the sample annealed at 250°C. This later result is more likely to be a result of substantially increased surface roughness.

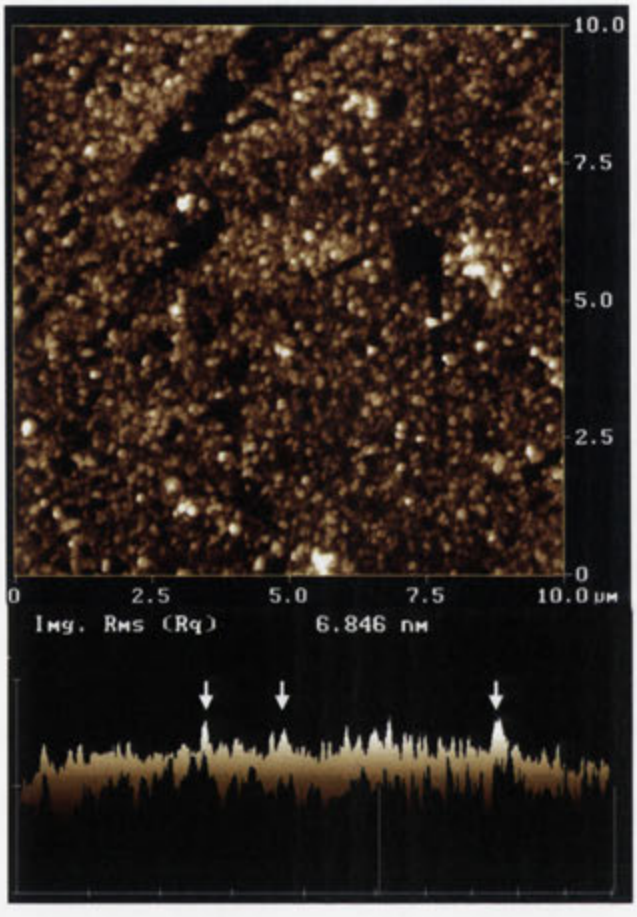

Figure 4.6: Roughness analysis using atomic force microscopy for etched ion-implanted a-Si annealed at 250°C. The root mean square (RMS) surface roughness obtained from the image is ~7 nm.

4.6 Summary

The state of a-Si annealed at various temperatures and the effect of in-diffused hydrogen on the deformation behavior of a-Si have been determined based on the ability of a-Si to phase transform during indentation. It was observed that, for annealing temperatures below 300°C, a-Si deformed plastically, and above 340°C, a-Si underwent phase transformations. There appears to be a transition point between 300 and 340°C where the partially relaxed a-Si undergoes phase transformation.

In chapter 3, it was shown that the bond-angle distortion is fully minimized at an annealing temperature of 500°C. The fact that the probability of phase transformation increases at temperatures before the bond-angle distortion is fully minimized suggests that the ability of a-Si to phase transform is related to defects, such as dangling bonds in the network, rather than full formation of a CRN with minimized bond-angle distortion.

In-diffused hydrogen through thermal annealing has no effect on the ability of a-Si to phase transform. The increased probability of a-Si to phase transform during indentation (at 250°C) is most likely caused by surface roughness from the chemical etching process.

Pressure-induced phase transformations clearly indicate that the determination of the probability of a phase transformation using indentation testing is sensitive to other processes of the structural relaxation rather than the bond-angle distortion alone (see chapter 3). However, in order to confirm whether these processes are indeed solely correlated to the dangling bond density, a characterization technique that is more directly sensitive to the dangling bond density is needed. This will be discussed in the next chapter.

5

Localized defect states

5.1 Introduction

The structural relaxation process in ion-implanted a-Si can be understood in terms of annealing of defect complexes accompanied by changes in the bond-angle distortion. As detailed in section 1.2, a structural defect in ion-implanted a-Si produces a local distortion in the covalent Si-Si network. Thus, the defect population increases the bond-angle distortion of the material [152] and these two processes are intrinsically linked together.

In this chapter, the presence and the density of defects produced in a-Si by ion implantation is determined by measuring changes in the electrical conductivity of a-Si. Thermal annealing is known to lead to a change in the electrical properties of a-Si [48], which is sensitively dependent on the *degree* of relaxation [153]. It is well accepted that the electrical conduction in a-Si occurs via variable-range hopping of charge carriers in the gap states (see section 2.2.5 for details). These localized states arise from dangling bonds in the network and are characterized by Mott's variable-range hopping relation [154]. Therefore, measurement of dynamic changes in electrical conductivity with annealing temperature can provide additional information on the contribution of defect recombination in the relaxation process.

The electrical conductivity measurements rely on the fact that structural imperfections, such as dangling bonds, introduce localized defect states near the Fermi level [28]. These dangling bonds create localized states near the middle of the band gap that pins the Fermi level. Electrical conduction is then characterized by different mechanisms, depending on the measurement temperature. In the low temperature region, the conduction mechanism

is dominated by variable-range hopping of charge carriers in the gap states, while in the high temperature region, conduction occurs via thermally assisted tunneling in the band tails. [122, 154] As thermal annealing is known to reduce the number of localized defect states, it is expected that defects and their contribution to the relaxation process can be probed by measuring the temperature dependent conductivity as a function of annealing temperature.

5.2 Experimental

A set of samples with dimensions 5×4 mm were prepared from 100 nm thick p-type silicon on insulator (SOI) wafers (for preparation details see section 2.1.4). The surface area of the samples was divided into two equal parts of 1.5×4 mm (to be used as contact) separated by 2×4 mm strips (which is to be amorphized) using photolithography and wet etching. The schematic of the device fabrication process is shown in Fig. 5.1. As illustrated, 200 nm of silicon dioxide (SiO_2) was deposited on the surface of the 2×4 mm (central) area. The contact areas of the samples were then doped with phosphorous to a fluence of 10^{15} ions cm^{-2} at an energy of 40 keV at room temperature in order to create an ohmic contact pad. This fluence was high enough to convert the low doped p-type Si into n-type Si. These samples were then annealed in a nitrogen environment at 850°C for 30 min in order to activate the dopants. [155] All samples were then measured using a four-point probe to ensure that the resistance of the n-doped (n-Si) regions was negligible compared to the sample resistance.

Chromium was deposited onto the sample to protect the n-Si regions during subsequent processing steps. The SiO_2 on the central region was then chemically removed using hydrofluoric acid (HF), which also removed the Cr layer sitting above it, thus exposing the c-Si area.

A continuous pure a-Si film was formed in the c-Si strips by implanting the area at liquid nitrogen temperature with Si ions using two energies of 25 and 55 keV with a fluence of 10^{15} ions cm^{-2} for each energy. The implantation slightly overlapped the contact regions in order to avoid the creation of p-n junctions at the (n-Si)-(a-Si) interface. Implantations were performed ~7° off to the beam direction to minimize ion channelling. 200 nm of SiO_2 was deposited on the sample to passivate the surface of the a-Si strips. The Cr layer was chemically removed from the top of the contact regions using $K_3Fe(CN)_6$+KOH, which also removed the deposited SiO_2 on top. Samples were then isochronally annealed for 30 min at various temperatures. For electrical contacts, 200 nm of aluminum was evaporated onto the contact regions under high vacuum using a thermal evaporator. The substrate temperature was kept below 100°C during deposition and the rate was controlled by a quartz crystal thickness monitor.

The samples were then mounted onto a side-brazed dual in-line ceramic package (DIP) using epoxy resin. In all cases, the DIPs were baked in an oven at 100°C for 10 min.

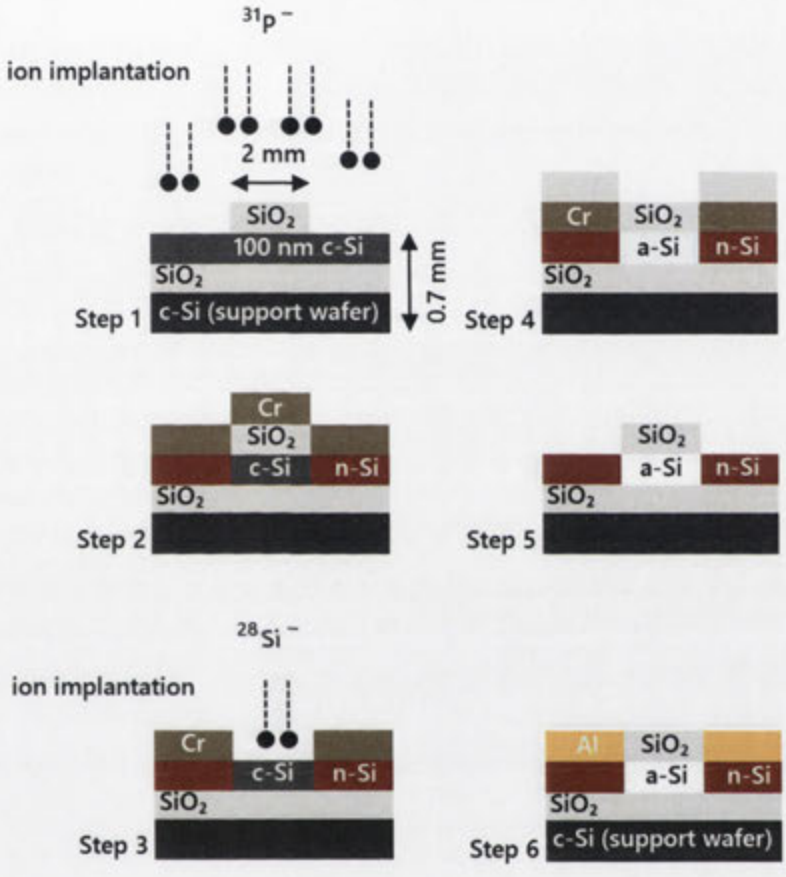

Figure 5.1: Schematic (not drawn to scale) of the device fabrication process for the electrical characterization of ion-implanted a-Si: Step 1. phosphorous (n-type) doping of the contact areas; Step 2. deposition of chromium onto the n-Si regions to protect them during subsequent processing steps; Step 3. removal of SiO_2 layer and Si strip amorphization via ion-implantation; Step 4. deposition of SiO_2 to passivate the a-Si region; Step 5. chromium removal; and Step 6. deposition of aluminum to create ohmic electrical contacts.

Contacts were verified to be Ohmic prior to use.

A n-type doping was used instead of p-type doping for convenience. It may be argued that this creates a p-n junction at the (n-Si)-(a-Si) interface. However, the 100 nm a-Si film was formed by Si ion implantation onto a lightly boron doped c-Si film: once amorphized, the conductivity is reduced by around 2-3 orders of magnitude and the conduction mechanism is dominated by hopping (defect) conduction rather than controlled by the dopant. Therefore, in this case neither light n-type or p-type doping of the starting material would affect the conduction mechanism in the a-Si.

The DIPs were mounted on a copper block in a vacuum liquid helium cryostat. Temperature control was achieved by a combination of helium flow control and power dissipated in an electrical heater on the copper block, regulated using a temperature controller. *In situ* conductivity for samples annealed at various temperatures (in *Celsius*) as a function of measurement temperature from 80 to 290 K (with an interval of 10 K between each measurement) was measured by applying a voltage from -5 to 5 V (in steps of 0.05 V) to the sample.

5.3 Density of localized states

The DC conductivity of a-Si annealed at various temperatures was determined by applying a voltage to the sample and measuring the sheet resistance of the sample from 80 to 290 K. It was observed, however, that annealing the sample above 450°C affected the measurement, i.e. a typical Schottky behaviour was observed when the sample was biased negatively while a positive bias resulted in tunneling. As a consequence, it is very difficult to calculate the sheet resistance from the current-voltage characteristic curves.

The kinetics of solid-phase epitaxial crytallization (SPE) have been extensively studied on a-Si [156–158], and Roth *et al.* [137] have observed ~18 nm of SPE growth from 2.2 μm thick a-Si heated to 500°C in vacuum for 30 min. This suggests that a small amount of SPE has occurred for samples annealed above 450°C and hence created an additional interface between n-Si and a-Si. Thus, electrical conductivity measurement for samples annealed above 450°C was not possible.

The variation of DC conductivity (σ) of a sample annealed at 250°C, for example, as a function of reciprocal temperature (T^{-1}) is shown in Fig. 5.2. As expected, the conductivity of the sample decreases as the measurement temperature decreases. At a temperature of ~180 K the conductivity plot starts to deviate from its linearity. This suggests that a-Si exhibits two distinct conduction mechanisms.

From 180 to 290 K, the conduction mechanism is dominated by the thermally assisted tunneling of charge carriers in the band tails. Below 180 K, conduction is dominated by variable-range hopping [122]. As previously mentioned, the structural defects in a-Si create localized states in the middle of the band gap that pins the Fermi level. Therefore the conduction mechanism in the low temperature region is sensitive to those defects as

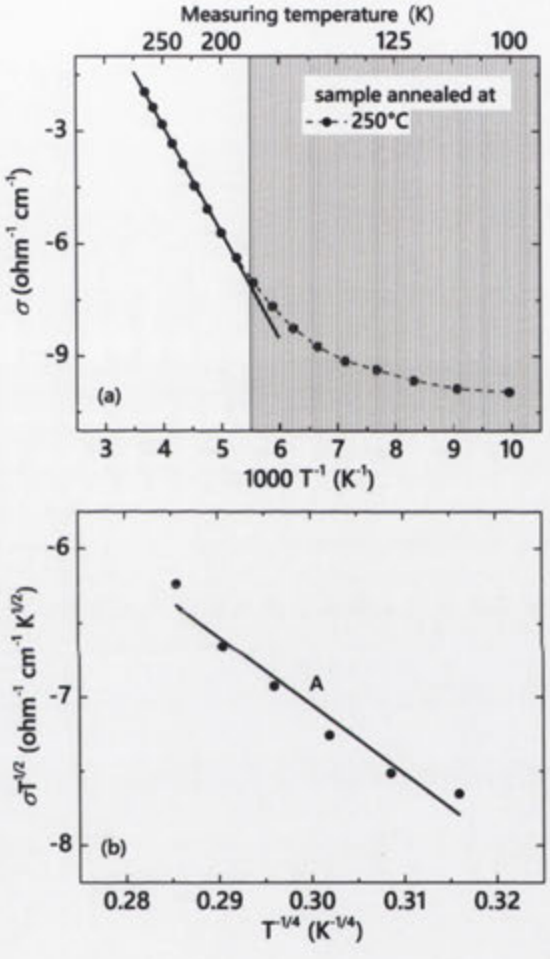

Figure 5.2: Semilog plot of (a) DC conductivity versus reciprocal measuring temperature, and (b) DC conductivity data at low temperature region (< 180 K) as ln $\sigma T^{1/2}$ versus $T^{-1/4}$ for ion-implanted a-Si sample annealed at 250°C. The solid lines in both plots are least-squares fits.

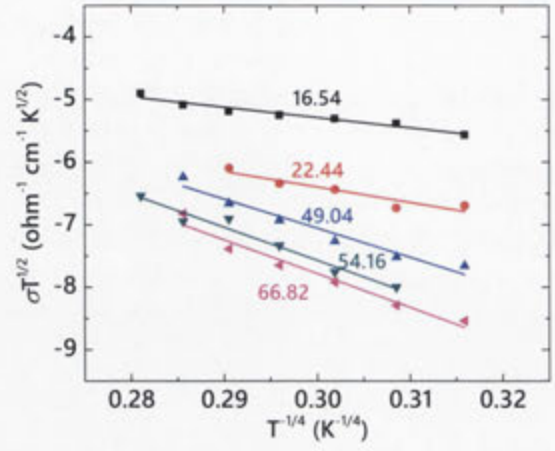

Figure 5.3: The conductivity data in the low temperature region (< 180 K) as ln $\sigma T^{1/2}$ versus $T^{-1/4}$ for ion-implanted samples annealed at various temperatures. The values of parameter A are calculated by taking the slope of the fit at each temperature.

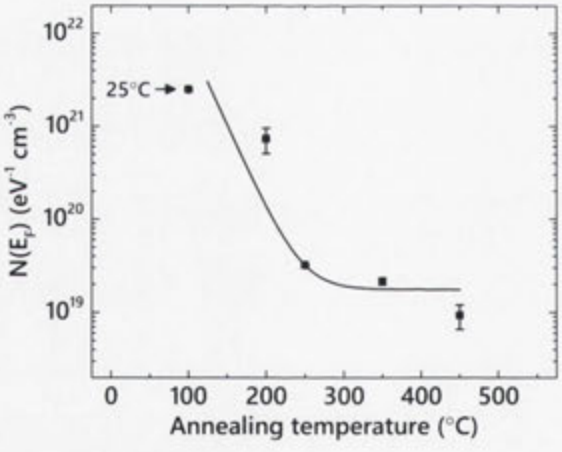

Figure 5.4: The density of localized states for ion-implanted samples annealed at various temperatures. Since all samples were pre-annealed at 100°C for 10 min during the device fabrication process, the as-implanted sample is thus shown at 100°C. The solid line is a guide for the eye only.

they introduce deep-lying states in the band gap. Hence, it is sensitive to the number of dangling bonds present in a-Si [121]. The conductivity in this low measuring temperature region is characterized by Mott's relation [122,154] and is given by Eq. 2.14.

The density of localized states at the Fermi level is calculated using Eq. 2.17, where the parameter A can be obtained from the conductivity data in the low temperature region ($<$ 180 K) from Fig. 5.2(a) as ln $\sigma T^{1/2}$ versus $T^{-1/4}$. This is shown in Fig. 5.2(b). Since the plot is now a linear function, the value of parameter A is simply the slope of the fit.

The conductivity data in the low temperature region for samples annealed at various temperatures is shown in Fig. 5.3. It is observed that the parameter A increases with increasing annealing temperature. As detailed in section 2.2.5, the parameter A and conductivity are inversely proportional to each other. A decrease in the number of dangling bonds (electrically active defect) in the sample due to thermal annealing leads to an increase in its sheet resistance. Hence, A increases with annealing temperature.

The calculated density of localized states, $N(E_F)$, for samples annealed at various temperatures is shown in Fig. 5.4. Since all samples were pre-annealed at 100°C for 10 min during the device fabrication process, the as-implanted sample is thus shown at 100°C. Starting from the as-implanted sample, it is clear that $N(E_F)$ decreases as the annealing temperature increases. A large fraction of defect (or dangling bond) recombination is observed to take place at low annealing temperatures, but this appears to be impeded for annealing temperatures above 300°C. The fact that different annealing temperatures yield different equilibrium values of $N(E_F)$, suggests the presence of defect recombination with a continuous spectrum of activation energies [159]. At a certain annealing temperature, defects can recombine or anneal out depending on the kinetics (activation energies) associated with the particular process.

T (°C)	$N(E_F)$(eV^{-1} cm^{-3}) present study	$N(E_F)$(eV^{-1} cm^{-3}) re-calculated	$N(E_F)$(eV^{-1} cm^{-3}) Coffa *et al.* [49]
100	$(2.48\pm0.04)\times10^{21}$	$(9.16\pm0.18)\times10^{22}$	1×10^{20}
200	$(7.33\pm2.25)\times10^{20}$	$(2.71\pm0.83)\times10^{22}$	9×10^{19}
250	$(3.22\pm0.02)\times10^{19}$	$(1.18\pm0.01)\times10^{21}$	7×10^{19}
350	$(2.16\pm0.18)\times10^{19}$	$(7.97\pm0.67)\times10^{20}$	6×10^{19}
450	$(9.33\pm2.75)\times10^{18}$	$(3.44\pm1.03)\times10^{20}$	3×10^{19}

Table 5.1: A direct comparison of the $N(E_F)$ and recalculated $N(E_F)$ of ion-implanted samples annealed at various temperatures obtained from the present study with those from Coffa *et al.* [49].

The density of localized states obtained in this study may be compared with those obtained by Coffa *et al.* [49]. For a direct comparison, the $N(E_F)$ are recalculated using the same Mott parameters as used by Coffa *et al.* [49] ($\alpha = 3.3\times10^7$ cm^{-1} and $\lambda = 16$). The comparison is shown in table 5.1. The recalculated $N(E_F)$, however, yield unreasonable results, such as $N(E_F) = \sim10^{23}$ eV^{-1} cm^{-3} for the as-implanted sample (shown at 100°C

in table 5.1) [160]. Nonetheless, the decrease of the number of defects during thermal annealing is consistent with that observed by Coffa *et al.* [49].

The discrepancy in the values for $N(E_F)$ might originate from the different methods used to create the a-Si and the measurement technique used. In their study, Coffa *et al.* [49] used 0.33 μm thick low-pressure chemical vapor-deposited a-Si layers. The samples were unrelaxed by irradiation of Si ions at an energy of 300 keV to a fluence of 5×10^{15} ions cm^{-2}. Upon irradiation the samples were annealed at 540°C for 1 hour. *In situ* conductivity measurements were performed during irradiation using 2 MeV Si ions with a fluence of 10^{11} ions cm^{-2}. The different structure (i.e. the deposited a-Si on thermally grown oxide), and different implantation and annealing conditions may have resulted in different in defect concentrations from present study. In particular, impurities and voids in the deposited a-Si would not be completely removed by annealing and re-irradiation. Hence, such a structure may well dramatically reduce the number of electrically active defects in the material. Alternatively, the overall defect level could be much higher but not probed by electrical measurements, i.e. non electrically active defects. Furthermore, rather than fabricating test structures for their measurements, Coffa *et al.* [49] used a two-point probe measurement. The simple two-point probe technique may not have been able to accurately measure the electrical conduction in a-Si as a result of alternative conduction pathways, such as at the surface.

It should be noted that Coffa *et al.* [49] used different Mott parameters that give unrealistic defect concentrations for the measurements in this thesis. In recent times, more refined Mott parameters [161] have been found to be in a good agreement with the results obtained by others studies [72, 162] in amorphous films and these were used in the present study. Although changing the Mott parameter does change the value of $N(E_F)$, such changes will not affect the main finding of this measurement, namely that the concentration of defect is reduced substantially after annealing at 250°C.

In summary, the electrical conductivity measurements in this study clearly show a decrease in the number of electrically active defects (through a reduction of $N(E_F)$ in the band gap) from 10^{21} to 10^{19} cm^{-3} upon annealing at 450°C. This implies that defect (such as dangling bonds) recombination contributes to the structural relaxation process.

5.4 Summary

It has been shown that the density of localized states at the Fermi level decreases with increasing annealing temperature. This clearly indicates that the structural relaxation process in ion-implanted a-Si is associated with a decrease in the number of electrically active defects caused by the reduction in number of localized defect states in the band gap, i.e. the density of localized states near the Fermi level is a function of the *degree* of relaxation.

Since the localized states near the Fermi level are assumed to have been created by

electrically active defects, that is, dangling bonds, the density of localized defect states should be associated with the density of dangling bonds in the material.

The experimental observation that the substantial decrease in the $N(E_F)$ (i.e. the defect reduction) observed at annealing temperatures of 250°C implies that defect annihilation (recombination) plays an important role in the structural relaxation process, specifically at low temperatures.

The relative contribution of defect annihilation in the structural relaxation process will be discussed in the next chapter in conjunction with the Raman spectroscopy and indentation data.

6

An extended model of structural relaxation

6.1 Existing models in prespective

On the basis of a *defective* CRN model, structural relaxation has been generally interpreted as a process predominantly due to a rearrangement of Si-Si bonds [163] versus defects removal [14]. Alternatively, the paracrystalline model interpreted structural relaxation as a dissolution of paracrystallites.

As previously mentioned in chapter 1, there are three models of the structural relaxation process, which will now be revisited in detail. Subsequently the results of this thesis will be contrasted with the existing models. An alternative model arising from results of this thesis will be proposed.

The first model by Stolk *et al.* [75] resulted from an investigation into the interrelation between defect annihilation, as probed by photocarrier lifetime, and network strain, as probed by Raman spectroscopy, in the structural relaxation process. These measurements were performed on as-implanted a-Si that was brought into various structural states by furnace annealing for 1 hour and heating by 32 ns laser irradiation. Figure 6.1(a) shows that the carrier lifetime (τ) in a-Si increases with annealing temperature from 0.8 ps for as-implanted sample to 10 ps for sample annealed at 500°C, while the half-width of the TO band (and thus bond-angle distortion) gradually decreases from 42.5 cm^{-1} for as-implanted to 36 cm^{-1} for sample annealed at 500°C. These results indicate that the bond-angle distortion and the defect density in a-Si are reduced **simultaneously** during thermal annealing.

Figure 6.1(b) shows that the carrier lifetime (τ) of laser annealed a-Si remains at the

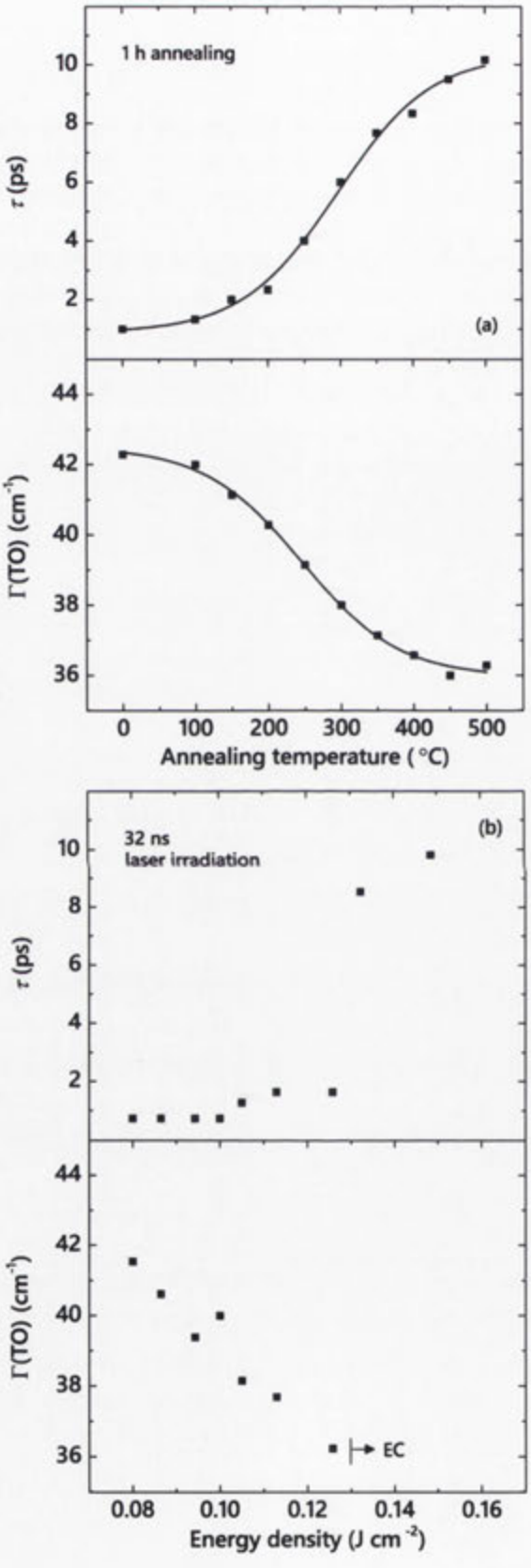

Figure 6.1: Carrier lifetime (τ) and Γ(TO)/2 as a function of (a) annealing temperature, and (b) energy density of the pulsed ruby laser as reported by Stolk *et al.* [75] (re-plotted).

level of as-implanted state up to energy densities of 0.125 J cm^{-2}. In contrast, the half-width of the TO band decreases continuously with increasing energy density. Furthermore, the half-width for sample irradiated with 0.125 J cm^{-2} is approximately 36 cm^{-1}, which is the level characteristic for fully relaxed a-Si as observed for furnace annealed sample at 500°C.

The two different behaviors in relaxation of annealed and laser irradiated a-Si were further investigated by reintroducing defects into relaxed sample by means of B, Si, and Xe ions implantation at liquid nitrogen temperature with various fluences. Stolk *et al.* [75] compared the carrier lifetime, and half-width of the TO band obtained from annealing, laser irradiation, and implantations. The authors observed that the degree of network strain in a-Si is not solely determined by the strain field associated with defects, i.e. for a-Si relaxed to a given intermediate value of bond-angle distortion, the density of defects was critically dependent on how that state had been reached (by furnace or pulsed-laser annealing). Thus, the relationship between defects and network strain in a-Si is strongly dependent on the dynamics of the annealing process involved.

The behavior of defects and structural ordering in a-Si is then modeled according to diffusion and defect kinetics. Defects in as-implanted a-Si are able to diffuse during laser annealing, but appreciable recombination has insufficient time to occur. Under this condition, **structural relaxation occurs without defect annihilation**. On the other hand, during furnace annealing, the diffusion length is long enough to enable both bond-angle relaxation and defect annealing. The model proposed by Stolk *et al.* [75] is not entirely consistent with results of this thesis. In this present study, a significant defect annihilation (reduction in dangling bond density) occurs before reduction in the bond-angle distortion. Hence the present study suggests that defect annihilation is an essential first step in structural relaxation, a point discussed further below.

Work by Roorda *et al.* [14] suggested a second model. This model was based on their observation from DSC that in addition to heat of crystallization, a-Si liberates low-temperature heat. This low-temperature heat release was attributed to structural relaxation. A careful analysis of the DSC data, as detailed in Ref. [14], showed that this low-temperature heat release consisted of a spectrum of processes with a continuous range of activation energies. By comparing the DSC data obtained from the defect annihilation process in ion-bombarded c-Si and identically treated relaxed a-Si, the authors observed that similar processes are occurring in these materials, i.e. the kinetics of the structural relaxation in a-Si appears to be similar to defect annihilation processes in c-Si. Roorda *et al.* [14] suggest that structural relaxation of a-Si is predominantly **defect annihilation**.

Figure 6.2 shows the relation between half-width of the TO peak and relaxation heat release upon annealing at temperatures up to 500°C, as reported by Roorda *et al.* [14]. Based on the assumption that the observed relaxation heat release in a-Si is point-defect annealing as it is in c-Si, a liner relation then exists between bond-angle distortion and relaxation heat release. This suggests that recombination of the point defects proceeds

with a reduction in the bond-angle distortion. The model proposed by Roorda *et al.* [14], again is not entirely consistent with the clearly separable processes of defect annihilation and reduction in the bond-angle distortion observed in the present study. This issue is further discussed below.

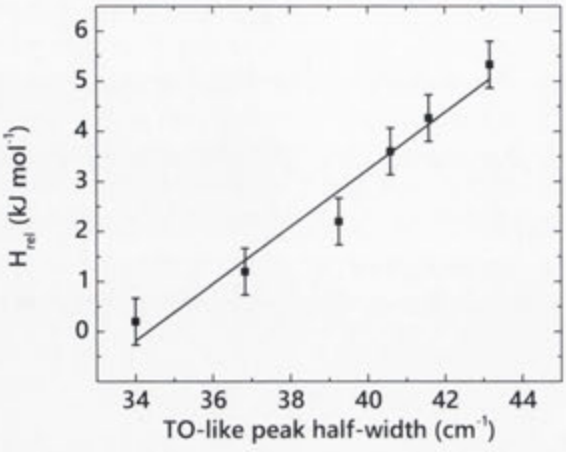

Figure 6.2: Relation between half-width ($\Gamma/2$) of TO band and relaxation heat release reported by Roorda *et al.* [14] (re-plotted). The solid line represent least-squares linear fit.

A the third model by Cheng *et al.* [42] was born from the observation of a decrease in the variance data (obtained from fluctuation electron microscopy) of ion-implanted a-Si on annealing at 500°C. The *degree* of medium-range order in a-Si is inferred from the variance peaks by taking the ratio of variance peak of annealed to as-implanted sample. The medium-range order is found to decrease with increasing annealing temperature [35,42,83]. However, the difference in medium-range order was only observed at annealing temperature above 450°C. Solely based on the premise that as-implanted a-Si is a paracrystalline structure on a medium-range order scale, Cheng *et al.* [42] suggest that structural relaxation of a-Si is a transient process. The annealed structure undergoes at least two transitions before re-crystallization. Although there is no experimental data supporting this idea, the first phase for structural relaxation at low temperature anneals is thought to be a short-range ordering, in which mobile defect and dangling bonds are reduced to increase short-range order. As the temperature increases, structural relaxation then moves to a second phase, that is medium-range disordering. This is a transition from a paracrystalline structure toward a continuous random network, possibly coupling with short-range ordering (if not finished).

The paracrystalline model does not adequately address the low temperature removal of defects observed in this thesis nor does the temperature range where bond-angle decreases agree with the temperature where *relaxation* is observed by medium-range ordering. Indeed, the data of this thesis are not consistent with a paracrystalline model as discussed below.

6.2 Comparison between previous studies and the results of the current study

It is apparent from the previous discussion that there is controversy in the nature of structural relaxation process in ion-implanted a-Si. In an attempt to resolve this controversy, the thermally-induced behavior of ion-implanted a-Si from as-prepared to relaxed states is investigated. As explored in detail in chapter 3, bond-angle distortion obtained from Raman spectroscopy was used to characterize the different disordered states of a-Si. The presence of these different states can also be mechanically probed using deformation (indentation) tests. This is the measurement of the ability of the material to withstand an applied pressure, and thus phase transform rather than plastically deform, as presented in detail in chapter 4. The ability of the material to withstand plastic deformation is indeed related to the number of structural defects in the structure. However, the indentation tests cannot establish a direct correlation between phase transformation and changes in the number of structural defects in the material. To recognize this relationship, electrical conductivity measurements were carried out. The conductivity measurement relies on the fact that structural defects create localized defect states in the band gap. Therefore, a change in the number of structural defects affects the electrical properties of the material. As presented in detail in chapter 5, the different disordered states of a-Si were correlated with the change of the electrical properties. In addition, a series of DSC measurements was performed to correlate the thermal properties of the material with structural changes.

The first result of the present study concerns the differences in bond-angle distortion of a-Si for various annealing temperatures. Result shows that different amorphous states exist in between as-implanted and relaxed states. The reduction in the bond-angle distortion with increasing annealing temperature is related to the structural relaxation process and this process clearly involves the rearrangement of Si bonds. In contrast to previous observations made by Stolk *et al.* [75] and Roorda *et al.* [14], this present study observed that the bond-angle distortion only changes slightly at the early stages of annealing; it begins to change significantly at temperatures above 250°C, and progressively reaches its minimum value at 550°C.

The present Raman spectroscopy data also demonstrate that the bond-angle distortion of ion-implanted and re-irradiated (of previously relaxed) a-Si is remarkably similar. Re-irradiated a-Si returns to an equivalent amorphous state as the original ion-implanted a-Si for all annealing temperatures. This eliminates the possibility that the ordering in the ion-implanted a-Si is related to the starting Si crystal, as proposed by the paracrystalline model [42].

PI a-Si is observed to have a higher bond-angle distortion in its as-prepared form in comparison with ion-implanted a-Si. However, both forms of a-Si result in the same minimum bond-angle distortion in the fully relaxed state.

The probability of phase transformation, the second result, indicates that under specific

loading and unloading conditions (chosen to favor ease of identification of phase transformation from unloading curves), three amorphous states exist in a-Si. The first is a state (below an annealing temperature of 300°C) where the material always deforms through simple plastic flow; the second is a state in which the material always phase transforms and the third is a transition state between these two states. The state of a-Si that is readily transforms is observed for annealing temperatures above 340°C. This implies that the annealing temperature of 300°C is the *cut-off* temperature where the partially relaxed a-Si can undergo phase transformations.

In addition to the above results, in-diffused hydrogen during annealing (as shown by SIMS data) was also considered. Raman spectroscopy and indentation tests show that in-diffused hydrogen does not significantly affect bond-angle distortion or the deformation mechanisms in ion-implanted a-Si.

The third result shows a decrease in the number of electrically active defects (conductivity) with increasing annealing temperature. The decrease in conductivity is related to a decrease in the number of localized defect states in the band gap created by structural defects (dangling bonds) in the material. The fact that different annealing temperatures yield different equilibrium values of localized defect states, suggests the defect recombination process has a continuous spectrum of activation energies [159]. At any given annealing temperature, defects may recombine or anneal out as determined by kinetics (activation energies) associated with the particular process. Although Stolk *et al.* [75] did not observe a decrease in electrically active defects for laser annealed a-Si, the furnace annealed a-Si clearly shows a decrease in the defect density along with bond-angle distortion upon annealing (see Fig 6.1). Roorda *et al.* [14], based on the similarity in the physical process between defect annihilation and structural relaxation of a-Si, assumed that defect annihilation was bound up with the reduction in bond-angle distortion.

In contrast to the previous two techniques that have been employed in this thesis, the hydrogen content of the a-Si sample used for electrical conductivity measurements was not measured. However, these samples were passivated with SiO_2 before being subjected to annealing. Thus, the possibility of the a-Si being affected by environmental factors such as in-diffused hydrogen during annealing is highly unlikely; if hydrogen does diffuse during annealing and reduces the number of defect states by forming $Si_{1-x}H_x$ bonds, the decreasing trend in the number of localized defect states with annealing temperature would have inversely mimicked the hydrogen profile as shown in Fig. 3.4. However, this is not the case.

6.3 An alternative model for the structural relaxation process

The different effect of thermal annealing on the bond-angle distortion, the ability of the material to phase transform, and localized defect states is shown in Fig. 6.3 along with the

data obtained from DSC. Figure 6.3 demonstrates that the temperature dependence of the ability of the material to phase transform and reduction in defect density suggest that the phase transformation behavior correlates with the state where most of dangling bonds have been repaired. It also indicates that the transition in the deformation mechanisms of the a-Si from plastic to phase transformation occurs before the bond-angle distortion is fully minimized. Thus, phase transformation can occur in a-Si that is not fully relaxed according to a minimum value of bond-angle distortion. This can be understood from the way this particular form of a-Si is created.

The structure of a-Si prepared by ion implantation contains a high concentration of structural defects. The presence of these defects promotes plastic deformation under applied stress. On annealing, these defects are removed and dangling bonds are repaired, hence phase transformation becomes the preferred mode of deformation in this fourfold coordinated structure. The observed increase in the probability of the material to undergo phase transformation before the minimization of bond-angle distortion is therefore suggesting the existence of an intermediate state. This intermediate state is related to the defect removal process and, as is shown below, to a reduction in the dangling bond density. Hence, removing such defects may result in a near-fourfold coordinated network that is only partially relaxed. Such a structure may increase its ability to inhibit plastic deformation, allowing the local pressure to increase sufficiently to undergo phase transition. Although the difference in the deformation mechanisms observed in a-Si can be well explained by defect removal in the structure, indentation tests are unable to directly establish the correlation between deformation behavior and defect removal.

The quantification of structural defects in a-Si is possible through electrical conductivity measurements. The results show that dramatic defect recombination occurs during annealing. Also, defects are mostly removed (or recombined) during low temperature anneals, i.e. below 250°C (see Fig. 6.3). This is in good agreement with indentation data; a substantial reduction in the dangling bond density occurs with the formation of a more rigid (fourfold-coordinated) structure, and thus its ability to inhibit plastic deformation is increased.

The contribution of defect removal in the structural relaxation process can be obtained by comparison of Raman spectroscopy data with electrical conductivity data. As shown in Fig. 6.3, at temperature ranges where significant defect annealing occurs, the bond-angle distortion is not significantly reduced. Thus, the rearrangement of Si bonds appears to commence only after most of the defects in the structure are annealed out. It should be noted, however, that this does not necessarily mean that the defect removal process stops when the rearrangement of the Si bonds takes place.

Results from Raman, indentation, and electrical conductivity measurements are in full agreement with the observation that the density of a-Si increased (0.1%) on heating from room temperature to 250°C, and then decreased (0.1%) on further increase of annealing temperature. [80] As shown in Fig. 6.3, a large fraction of defects (dangling bonds) are

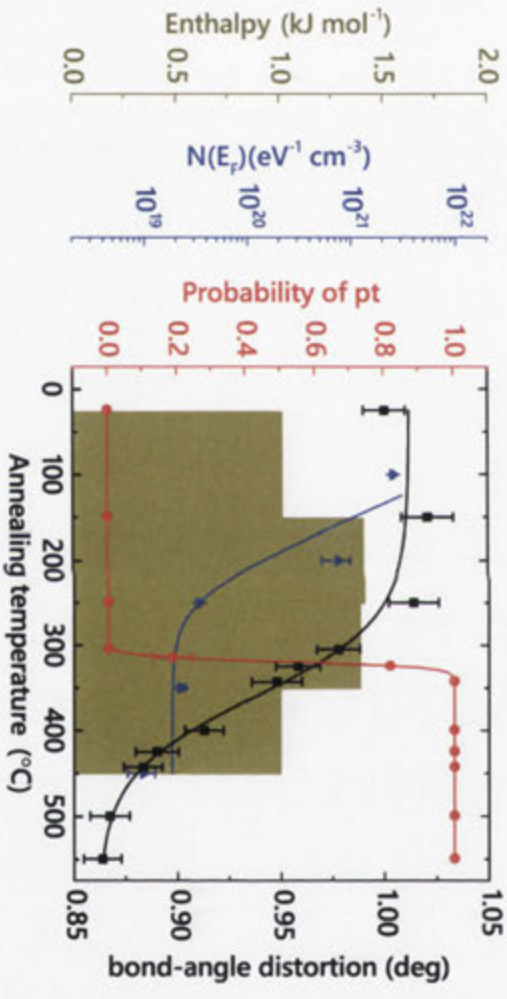

Figure 6.3: The structural relaxation mechanism in ion-implanted a-Si. This plot shows the different effect of thermal annealing on the bond-angle distortion (normalized) (black solid square), the ability of the material to phase transform (red solid circle), defect density (blue solid triangle), and heat release (yellow bar graph). The solid lines serve to guide the eye only.

recombined upon annealing at 250°C, since this process is not accompanied by changes in the structure of the network, i.e. a small reduction in the bond-angle distortion, it results in an increase in density.

In addition to the previous three main techniques that have been employed in this thesis, thermally-induced structural relaxation is also observed in differential scanning calorimetry measurements. The details of scan methods are shown in Fig. 2.17. As previously observed by Roorda *et al.* [14], this present study also observed that a-Si liberates heat during low temperature anneals, i.e. below 250°C. The experimental conditions of Roorda *et al.* [14] were quite different from those employed here, making direct comparison of annealing data difficult. However, in contrast to Roorda *et al.* [14], the bond-angle distortion only changes slightly in the low annealing temperature range (< 300°C). This is a clear indication that the heat release observed in the low annealing temperature range is mostly due to the defect removal process, while the contribution of the rearrangement of Si bonds is minimal. There is a further heat release up to 450°C that correlates with a decrease in bond-angle distortion.

As previously mentioned in section 2.2.6, in the DSC measurement, the heat release was measured by scanning the material from 25 to 150°C at 40 K min^{-1}; the instrument was held constant at the end of each step for 30 min and then cooled down to 25°C before repeating the scan for higher end temperatures, as shown detailed in Fig. 2.17. Thus, ideally the heat release from the second scan should correspond to structural changes from 150 to 250°C. However, it was observed that some heat is liberated at the temperature range of the first scan during the second scan. The most likely explanation for this phenomenon is that during the first scan, some of the dangling bonds in the network were repaired and this caused a partial rearrangement of surrounding atoms to create fourfold coordinated Si atoms. Consequently, the rearrangement of the Si bonds took place. Since the rearrangement of Si bonds involves reconstruction of the entire tetrahedral network, a significant amount of energy is required. Thus, the observed phenomenon could possibly be due to the derelaxation of partially relaxed Si bonds as a consequence of there being insufficient energy at certain annealing stages to maintain the stability of the network in its transient state.

The data presented in Fig. 6.3 demonstrates that:

1. In as-prepared (unrelaxed) state, ion-implanted a-Si is best described as a defective CRN with a high concentration of structural defects (leading to significantly undercoordinated material). Thus, it gives rise to the high distortion in the bond-angles.
2. Low temperature anneals provide enough atomic mobility to activate the recombination of dangling bonds, while the effect on the overall network strain (and thus bond-angle distortion) is minimal.
3. Once defects are mostly recombined and the structure becomes near-fourfold coordinated, the rearrangement of the Si bonds (thus reduction in bond-angle distortion) becomes the dominant process.

4. Impurities, such as hydrogen do not significantly affect the local ordering.

The structural relaxation process is thus described as a defect removal process accompanied by a small reduction in the bond-angle distortion followed by the rearrangement of Si bonds in which further reducing the bond angle distortion, as shown schematically in Fig. 6.4. The results obtained in this present study thus suggest that bond-angle minimization cannot occur without defect recombination first taking place.

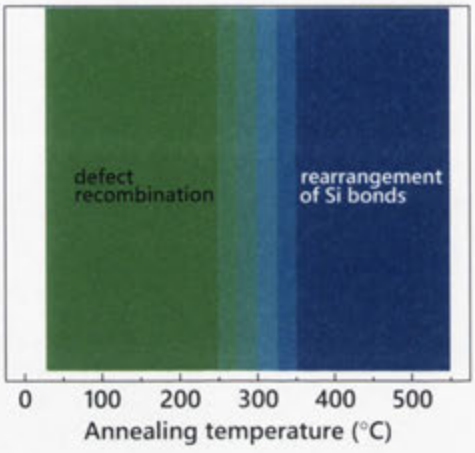

Figure 6.4: Schematic of an extended model of structural relaxation in ion-implanted a-Si.

Previous studies [14,42,75] of structural relaxation in ion-implanted a-Si have proposed that there are three possible models. This thesis proposes a modification of the previously model interpreted by Roorda *et al.* [14]. If electrical data (reduction in the density of dangling bonds) was available to Roorda *et al.*, they may not have attempted to couple the effect of defect annihilation and reduction in the bond-angle distortion. Otherwise, the data obtained from the present study is generally consistent with the observations of Roorda *et al.*

6.4 Summary

To summarize, the thermally-induced behavior of a-Si prepared by ion implantation has been extensively investigated from the as-prepared (unrelaxed) state to the relaxed state. This has allowed an understanding in the nature of the structural relaxation process of a-Si. This thesis interprets structural relaxation as a *multistage* process involving two main dominant steps: a reduction in defects followed by rearrangement of Si bonds.

7

Concluding remarks

The structural relaxation in pure a-Si has been investigated in some detail. Three types of a-Si: ion-implanted, pressure-induced, and re-irradiated (of previously relaxed) a-Si were prepared for studying the annealing-induced short-range ordering. However, the small (localized) volumes that can be created from pressure-induced amorphization places a limitation on the ability to characterize this form of a-Si. Therefore, at this stage, pressure-induced a-Si was not investigated in as much detail as the ion-implanted a-Si.

An extensive study of the variations in the deformation mechanism, optical (bond-angle distortion), electrical (density of localized states), and thermal (heat release) properties of ion-implanted a-Si caused by thermal annealing in the temperature from 25 to 550°C demonstrated that the properties of ion-implanted a-Si strongly depend on its annealing history. Importantly, results from present study provide quantitative information regarding the nature of the structural relaxation process in such material. It is found that there are two main dominant steps in structural relaxation: defect (dangling bond) removal at low temperatures up to 250°C, which is accompanied by a significant heat release, and predominantly rearrangement of Si bonds at higher temperatures, where the amount of heat release is smaller. There is no evidence in this present study to support the paracrystalline model.

7.1 Future directions

Although this study answers many questions pertaining to the structural relaxation process of pure a-Si, it also raises several new questions which require further experimental work.

The first proposed set of further experimental studies concerns the longer scale (medium-range) ordering of a-Si. This could be achieved by employing FEM, an electron microscopy technique that is sensitive to medium-range order in disordered materials. Indeed, previous studies [35, 133] have shown that structural relaxation was observable by FEM and the *degree* of medium-range ordering of ion-implanted a-Si is demonstrated to decrease significantly on annealing. However, these results were not reproducible and are inconsistent. In addition to a decrease in medium-range order due to annealing, some studies also showed a depth dependence of the medium-range order in the as-implanted samples that could not be explained [35].

It is clear from the previous discussion in chapter 3 that pressure-induced a-Si may undergo a different relaxation process to ion-implanted a-Si, although the final fully relaxed states appear similar. Thus, indentation and defect studies as performed for ion-implanted a-Si would be a second interesting experiments that could shed further light on the mechanism of structural relaxation from different starting forms.

Bibliography

[1] Encyclopedia, N. W. Glass – new world encyclopedia, (2013). URL \url{http://www.newworldencyclopedia.org/p/index.php?title=Glass&oldid=977085}. [Online; accessed 4-August-2014].

[2] Fleming, S. J. *Roman Glass: Reflections on Cultural Change* (University of Pennsylvania Press, Pennsylvania, 1999).

[3] Stern, E. M. Roman glassblowing in a cultural context. *American Journal of Archaeology* **103**, 441–484 (1999).

[4] Wuttig, M. & Yamada, N. Phase-change materials for rewriteable data storage. *Nature Materials* **6**, 824–832 (2007).

[5] Robertson, J. Properties of diamond-like carbon. *Surface and Coatings Technology* **50**, 185–203 (1992).

[6] Lifshitz, Y. Diamond-like carbon - present status. *Diamond and Related Materials* **8**, 1659–1676 (1999).

[7] Powell, M. J. The physics of amorphous-silicon thin-film transistors. *Electron Devices, IEEE Transactions on* **36**, 2753–2763 (1989).

[8] Carlson, D. E. & Wronski, C. R. Amorphous silicon solar cell. *Applied Physics Letters* **28**, 671–673 (1976).

[9] Zachariasen, W. H. The atomic arrangement in glass. *Journal of the American Chemical Society* **54**, 3841–3851 (1932).

[10] Reuter, H. Amorphous inorganic materials and glasses. von a. feltz vch verlagsgesellschaft, weinheim/vch publishers, new york, 1993. 440 s., geb. 198.00 dm. âĂŞ isbn 3-527-28421-4/ 1-56081-212-5. *Angewandte Chemie* **106**, 2442–2442 (1994).

[11] Pfaender, H. G. *Schott Guide to Glass* (Springer, 1995).

[12] Polk, D. E. Structural model for amorphous silicon and germanium. *Journal of Non-Crystalline Solids* **5**, 365–376 (1971).

[13] Fortner, J. & Lannin, J. S. Radial distribution functions of amorphous silicon. *Phys. Rev. B* **39**, 5527–5530 (1989).

[14] Roorda, S., Sinke, W. C., Poate, J. M., Jacobson, D. C., Dierker, S., Dennis, B. S., Eaglesham, D. J., Spaepen, F. & Fuoss, P. Structural relaxation and defect annihilation in pure amorphous silicon. *Phys. Rev. B* **44**, 3702–3725 (1991).

[15] Laaziri, K., Kycia, S., Roorda, S., Chicoine, M., Robertson, J. L., Wang, J. & Moss, S. C. High-energy x-ray diffraction study of pure amorphous silicon. *Phys. Rev. B* **60**, 13520–13533 (1999).

[16] Voyles, P. M., Gerbi, J. E., Treacy, M. M. J., Gibson, J. M. & Abelson, J. R. Absence of an abrupt phase change from polycrystalline to amorphous in silicon with deposition temperature. *Phys. Rev. Lett.* **86**, 5514–5517 (2001).

[17] Moss, S. C. & Graczyk, J. F. Evidence of voids within the as-deposited structure of glassy silicon. *Phys. Rev. Lett.* **23**, 1167–1171 (1969).

[18] Graczyk, J. F. & Moss, S. C. In *Proc. X Intern. Conf. Phys. Semicond.*, 658 (Cambridge, Mass., 1970).

[19] Graczyk, J. F. *On the Structure Analysis of Amorphous Materials*, vol. 20 of *Nato Science Series B: (closed)* (Springer, 1976).

[20] Saitoh, S., Sugii, T., Ishiwara, H. & Furukawa, S. Growth conditions of deposited Si films in solid phase epitaxy. *Japanese Journal of Applied Physics* **20**, L130–L132 (1981).

[21] Roorda, S., Doorn, S., Sinke, W. C., Scholte, P. M. L. O. & van Loenen, E. Calorimetric evidence for structural relaxation in amorphous silicon. *Phys. Rev. Lett.* **62**, 1880–1883 (1989).

[22] Hubler, G. K., Donovan, E. P., Wang, K.-W. & Spitzer, W. G. Thermal annealing behavior of hydrogen-free amorphous silicon and germanium. *Proc. SPIE* **0530**, 222–229 (1985).

[23] Tsu, R., Hernandez, J. G., Doehler, J. & Ovshinsky, S. R. Order parameters in a-Si systems. *Solid State Communications* **46**, 79–82 (1983).

[24] Tsu, R., Hernandez, J. G. & Pollak, F. H. Determination of energy barrier for structural relaxation in a-Si and a-Ge by Raman scattering. *Journal of Non-Crystalline Solids* **66**, 109–114 (1984).

[25] Beeman, D., Tsu, R. & Thorpe, M. F. Structural information from the raman spectrum of amorphous silicon. *Phys. Rev. B* **32**, 874–878 (1985).

[26] Sinke, W., Warabisako, T., Miyao, M., Tokuyama, T., Roorda, S. & Saris, F. W. Transient structural relaxation of amorphous silicon. *Journal of Non-Crystalline Solids* **99**, 308–323 (1988).

[27] Fredrickson, J. E., Waddell, C. N., Spitzer, W. G. & Hubler, G. K. Effects of thermal annealing on the refractive index of amorphous silicon produced by ion implantation. *Applied Physics Letters* **40** (1982).

[28] Spitzer, W. G., Hubler, G. K. & Kennedy, T. A. Properties of amorphous silicon produced by ion implantation: Thermal annealing. *Nuclear Instruments and Methods in Physics Research* **209-210, Part 1**, 309–312 (1983).

[29] Donovan, E. P., Spaepen, F., Turnbull, D., Poate, J. M. & Jacobson, D. C. Calorimetric studies of crystallization and relaxation of amorphous Si and Ge prepared by ion implantation. *Journal of Applied Physics* **57** (1985).

[30] Donovan, E., Spaepen, F., Poate, J. & Jacobson, D. Homogeneous and interfacial heat releases in amorphous silicon. *Applied Physics Letters* **55**, 1516–1518 (1989).

[31] Elliott, S. R. Medium-range structural order in covalent amorphous solids. *Nature* **354**, 445–452 (1991).

[32] Gibson, J. M. & Treacy, M. M. J. Diminished medium-range order observed in annealed amorphous germanium. *Phys. Rev. Lett.* **78**, 1074–1077 (1997).

[33] Treacy, M. M. J., Gibson, J. M. & Keblinski, P. J. Paracrystallites found in evaporated amorphous tetrahedral semiconductors. *Journal of Non-Crystalline Solids* **231**, 99–110 (1998).

[34] Voyles, P. M. *Fluctuation electron microscopy of medium-range order in amorphous silicon thin films.* Ph.D. thesis, University of Illinois at Urbana-Champaign (2001).

[35] Cheng, J. Y., Gibson, J. M. & Jacobson, D. C. Observations of structural order in ion-implanted amorphous silicon. *Journal of Materials Research* **16**, 3030–3033 (2001).

[36] Gerbi, J. E., Voyles, P. M., Treacy, M. M. J., Gibson, J. M. & Abelson, J. R. Increasing medium-range order in amorphous silicon with low-energy ion bombardment. *Applied Physics Letters* **82** (2003).

[37] Gibson, J. M., Treacy, M. M. J., Sun, T. & Zaluzec, N. J. Substantial crystalline topology in amorphous silicon. *Phys. Rev. Lett.* **105**, 125504 (2010).

[38] Treacy, M. M. J. & Borisenko, K. B. The local structure of amorphous silicon. *Science* **335**, 950–953 (2012).

[39] Voyles, P. M., Gibson, J. M. & Treacy, M. M. J. Fluctuation microscopy: a probe of atomic correlations in disordered materials. *Journal of Electron Microscopy* **49**, 259–266 (2000).

[40] Treacy, M. M. J., Gibson, J. M., Fan, L., Paterson, D. J. & McNulty, I. Fluctuation microscopy: a probe of medium range order. *Reports on Progress in Physics* **68**, 2899 (2005).

[41] Hosemann, R. & Bagchi, A. N. Direct analysis of diffraction by matter. *Journal of Polymer Science Part A: General Papers* **1**, 831–832.

[42] Cheng, J. Y., Gibson, J. M., Baldo, P. M. & Kestel, B. J. Quantitative analysis of annealing-induced structure disordering in ion-implanted amorphous silicon. *Journal of Vacuum Science and Technology A* **20** (2002).

[43] Cheng, J. Y. & Gibson, J. M. A damage model for disordered structures in ion irradiated silicon. In *Symposium O - Ion Beam Synthesis and Processing of Advanced Materials*, vol. 647 of *MRS Proceedings* (2000).

[44] Cheng, J. Y. & Gibson, J. M. Simple energy spike model for paracrystalline silicon in ion implantation. *Journal of Vacuum Science and Technology A* **22** (2004).

[45] Roorda, S. Comment on "Quantitative analysis of annealing-induced structure disordering in ion-implanted amorphous silicon", by Ju-Yin Cheng *et al.*, J. Vacuum Science and Technology A 20, 1855 (2002). *Journal of Vacuum Science and Technology A* **21** (2003).

[46] Lannin, J. S., Pilione, L. J., Kshirsagar, S. T., Messier, R. & Ross, R. C. Variable structural order in amorphous silicon. *Phys. Rev. B* **26**, 3506–3509 (1982).

[47] Haberl, B., Bradby, J. E., Swain, M. V., Williams, J. S. & Munroe, P. Phase transformations induced in relaxed amorphous silicon by indentation at room temperature. *Applied Physics Letters* **85**, 5559–5561 (2004).

[48] Roorda, S., Hakvoort, R. A., van Veen, A., Stolk, P. A. & Saris, F. W. Structural and electrical defects in amorphous silicon probed by positrons and electrons. *Journal of Applied Physics* **72**, 5145–5152 (1992).

[49] Coffa, S., Priolo, F. & Battaglia, A. Defect production and annealing in ion-implanted amorphous silicon. *Phys. Rev. Lett.* **70**, 3756–3759 (1993).

[50] Maley, N. & Lannin, J. S. Influence of hydrogen on vibrational and optical properties of a-$Si_{1-x}H_x$ alloys. *Phys. Rev. B* **36**, 1146–1152 (1987).

[51] Smith, Z. E. & Wagner, S. Band tails, entropy, and equilibrium defects in hydrogenated amorphous silicon. *Phys. Rev. Lett.* **59**, 1790–1790 (1987).

[52] Meek, P. E. Vibrational spectra and topological structure of tetrahedrally bonded amorphous semiconductors. *Philosophical Magazine* **33**, 897–908 (1976).

[53] Sokolov, A. P., Shebanin, A. P., Golikova, O. A. & Mezdrogina, M. M. Structural disorder and optical gap fluctuations in amorphous silicon. *Journal of Physics: Condensed Matter* **3**, 9887 (1991).

[54] Fortner, J. & Lannin, J. S. Structural relaxation and order in ion-implanted Si and Ge. *Phys. Rev. B* **37**, 10154–10158 (1988).

[55] Gupta, M. C. & Ruoff, A. L. Static compression of silicon in the [100] and in the [111] directions. *Journal of Applied Physics* **51** (1980).

[56] Clarke, D. R., Kroll, M. C., Kirchner, P. D., Cook, R. F. & Hockey, B. J. Amorphization and conductivity of silicon and germanium induced by indentation. *Phys. Rev. Lett.* **60**, 2156–2159 (1988).

[57] Callahan, D. L. & Morris, J. C. The extent of phase transformation in silicon hardness indentations. *Journal of Materials Research* **7**, 1614–1617 (1992).

[58] Gogotsi, Y. G., Kailer, A. & Nickel, K. G. Phase transformations in materials studied by micro-raman spectroscopy of indentations. *Material Research Innovations* **1**, 3–9 (1997).

[59] Gogotsi, Y. G., Domnich, V., Dub, S. N., Kailer, A. & Nickel, K. G. Cyclic nanoindentation and Raman microspectroscopy study of phase transformations in semiconductors. *Journal of Materials Research* **15**, 871–879 (2000).

[60] Ruffell, S., Bradby, J. E. & Williams, J. S. High pressure crystalline phase formation during nanoindentation: Amorphous versus crystalline silicon. *Applied Physics Letters* **89**, 091919 (2006).

[61] Imai, M., Mitamura, T., Yaoita, K. & Tsuji, K. Pressure-induced phase transition of crystalline and amorphous silicon and germanium at low temperatures. *High Pressure Research* **15**, 167–189 (1996).

[62] Daisenberger, D., Wilson, M., McMillan, P. F., Quesada Cabrera, R., Wilding, M. C. & Machon, D. High-pressure x-ray scattering and computer simulation studies of density-induced polyamorphism in silicon. *Phys. Rev. B* **75**, 224118 (2007).

[63] Hanfland, M. & Syassen, K. Raman modes of metastable phases of Si and Ge. *High Pressure Research* **3**, 242–244 (1990).

[64] Olijnyk, H. & Jephcoat, A. P. Effect of pressure on Raman spectra of metastable phases of Si and Ge. *Physica Status Solidi (b)* **211**, 413 (1999).

[65] Aji, L. B. B., Ruffell, S., Haberl, B., Bradby, J. E. & Williams, J. S. Correlation of indentation-induced phase transformations with the degree of relaxation of ion-implanted amorphous silicon. *Journal of Materials Research* **28**, 1056–1060 (2013).

[66] Haberl, B., Bradby, J. E., Ruffell, S., Williams, J. S. & Munroe, P. Phase transformations induced by spherical indentation in ion-implanted amorphous silicon. *Journal of Applied Physics* **100** (2006).

[67] van den Hoven, G. N., Liang, Z. N., Niesen, L. & Custer, J. S. Evidence for vacancies in amorphous silicon. *Phys. Rev. Lett.* **68**, 3714–3717 (1992).

[68] Polman, A., Jacobson, D. C., Coffa, S., Poate, J. M., Roorda, S. & Sinke, W. C. Defect states of amorphous Si probed by the diffusion and solubility of Cu. *Applied Physics Letters* **57**, 1230–1232 (1990).

[69] Falster, R. Gettering in silicon: fundamentals and recent advances. *This article appeared in Semiconductor Fabtech 13th edition.* 1–14 (2001).

[70] Coffa, S., Poate, J. M., Jacobson, D. C. & Polman, A. Impurity trapping and gettering in amorphous silicon. *Applied Physics Letters* **58**, 2916–2918 (1991).

[71] Pantelides, S. T. The electronic structure of impurities and other point defects in semiconductors. *Rev. Mod. Phys.* **50**, 797–858 (1978).

[72] Shin, J. H. & Atwater, H. A. Activation-energy spectrum and structural relaxation dynamics of amorphous silicon. *Phys. Rev. B* **48**, 5964–5972 (1993).

[73] Laaziri, K., Kycia, S., Roorda, S., Chicoine, M., Robertson, J. L., Wang, J. & Moss, S. C. High resolution radial distribution function of pure amorphous silicon. *Phys. Rev. Lett.* **82**, 3460–3463 (1999).

[74] Battaglia, A., Coffa, S., Priolo, F., Compagnini, G. & Baratta, G. A. Low-temperature modifications in the defect structure of amorphous silicon probed by in situ Raman spectroscopy. *Applied Physics Letters* **63**, 2204–2206 (1993).

[75] Stolk, P. A., Saris, F. W., Berntsen, A. J. M., Weg, W. F. v. d., Sealy, L. T., Barklie, R. C., Krotz, G. & MÃijller, G. Contribution of defects to electronic, structural, and thermodynamic properties of amorphous silicon. *Journal of Applied Physics* **75**, 7266–7286 (1994).

[76] Ishimaru, M. Atomistic simulations of structural relaxation processes in amorphous silicon. *Journal of Applied Physics* **91**, 686–689 (2002).

[77] Beardmore, K. M. & Grønbech-Jensen, N. Direct simulation of ion-beam-induced stressing and amorphization of silicon. *Phys. Rev. B* **60**, 12610–12616 (1999).

[78] Roura, P., Farjas, J. & Roca i Cabarrocas, P. Quantification of the bond-angle dispersion by Raman spectroscopy and the strain energy of amorphous silicon. *Journal of Applied Physics* **104** (2008).

[79] Crawford, J. H. & Slifkin, L. M. (eds.) *Point Defects in Solids: General and Ionic Crystals* (Plenum Press, New York, 1972).

[80] Volkert, C. A. Density changes and viscous flow during structural relaxation of amorphous silicon. *Journal of Applied Physics* **74** (1993).

[81] Custer, J. S., Thompson, M. O., Jacobson, D. C., Poate, J. M., Roorda, S., Sinke, W. C. & Spaepen, F. Density of amorphous Si. *Applied Physics Letters* **64**, 437–439 (1994).

[82] Urli, X., Dias, C. L., Lewis, L. J. & Roorda, S. Point defects in pure amorphous silicon and their role in structural relaxation: A tight-binding molecular-dynamics study. *Phys. Rev. B* **77**, 155204 (2008).

[83] Cheng, J. Y. *Fluctuation electron microscopy of medium-range order in ion-implanted amorphous silicon.* Ph.D. thesis, University of Illinois at Urbana-Champaign (2002).

[84] Roorda, S., Custer, J. S., Sinke, W. C., Poate, J. M., Jacobson, D. C., Polman, A. & Spaepen, F. Structural relaxation in amorphous silicon and the role of network defects. *Nuclear Instruments and Methods in Physics Research Section B: Beam Interactions with Materials and Atoms* **59-60, Part 1**, 344–352 (1991).

[85] Bean, J. C. & Poate, J. M. Evidence for void interconnection in evaporated amorphous silicon from epitaxial crystallization measurements. *Applied Physics Letters* **36**, 59–61 (1980).

[86] Brodsky, M. H., Kaplan, D. & Ziegler, J. Densities of amorphous Si films by nuclear backscattering. *Applied Physics Letters* **21**, 305–307 (1972).

[87] Manchester, K. E., Sibley, C. B. & Alton, G. Doping of silicon by ion implantation. *Nuclear Instruments and Methods* **38**, 169–174 (1965).

[88] King, W. J., Burrill, J. T., Harrison, S., Martin, F. & Kellett, C. Experience in fabricating semiconductor devices using ion implantation techniques. *Nuclear Instruments and Methods* **38**, 178–179 (1965).

[89] Armini, A. J., Bunker, S. N. & Spitzer, M. B. Non-mass-analyzed ion implantation equipment for high volume solar cell production. In *Proc. 16th IEEE Photovoltaic Specialists Conference*, 895–899 (1982).

[90] Williams, J. S. Materials modification with ion beams. *Reports on Progress in Physics* **49**, 491 (1986).

[91] Lindhard, J. & Scharff, M. Energy dissipation by ions in the keV region. *Phys. Rev.* **124**, 128–130 (1961).

[92] Jung, P. Atomic displacement functions of cubic metals. *Journal of Nuclear Materials* **117**, 70–77 (1983).

[93] Ishimaru, M., Harada, S. & Motooka, T. Transmission electron microscopy studies of crystal-to-amorphous transition in ion implanted silicon. *Journal of Applied Physics* **81**, 1126–1130 (1997).

[94] Schultz, P. J., Jagadish, C., Ridgway, M. C., Elliman, R. G. & Williams, J. S. Crystalline-to-amorphous transition for Si-ion irradiation of Si(100). *Phys. Rev. B* **44**, 9118–9121 (1991).

[95] Motooka, T., Kobayashi, F., Fons, P., Tokuyama, T., Suzuki, T. & N., N. Amorphization processes in ion implanted Si: temperature dependence. *Japanese Journal of Applied Physics* **30**, 3617–3620 (1991).

[96] Bierschenk, T. *Swift heavy ion irradiation of amorphous Ge, amorphous Si, and amorphous SiGe alloys.* Ph.D. thesis, Australian National University (2014).

[97] Motooka, T. & Holland, O. W. Amorphization processes in ion implanted Si: Ion species effects. *Applied Physics Letters* **61**, 3005–3007 (1992).

[98] Dennis, J. R. & Hale, E. B. Energy dependence of amorphizing implant dose in silicon. *Applied Physics Letters* **29**, 523–524 (1976).

[99] Bai, G. & Nicolet, M.-A. Defects production and annealing in self-implanted Si. *Journal of Applied Physics* **70**, 649–655 (1991).

[100] Ziegler, J. F., Ziegler, M. D. & Biersack, J. P. Srim - the stopping and range of ions in matter. *Nuclear Instruments and Methods in Physics Research B* **268**, 1818–1823 (2010).

[101] Wikipedia. Furnace anneal – wikipedia, the free encyclopedia (2013). URL `\url{http://en.wikipedia.org/w/index.php?title=Furnace_anneal&oldid=158425443}`. [Online; accessed 22-July-2014].

[102] Mack, C. A. *Fundamental Principles of Optical Lithography* (John Wiley & Sons, New York, 2007).

[103] Ponyatovsky, E. G. & Barkalov, O. I. Pressure-induced amorphous phases. *Materials Science Reports* **8**, 147–191 (1992).

[104] Williams, D. B. & Carter, C. B. *Transmission Electron Microscopy: A Textbook for Materials Science* (Springer, 2009).

[105] Rao, D. V. S., Muraleedharan, K. & Humphreys, C. J. Tem specimen preparation techniques. *Microscopy: Science, Technology, Aplications and Education, FORMATEX Research Center, Extremadura Es* 1232–1244 (2010).

[106] Benninghoven, A., RÃijdenauer, F. G. & Werner, H. W. *Secondary Ion Mass Spectrometry: Basic Concepts, Instrumental Aspects, Applications, and Trends* (John Wiley & Sons, New York, 1987).

[107] McPhail, D. Applications of secondary ion mass spectrometry (SIMS) in materials science. *Journal of Materials Science* **41**, 873–903 (2006).

[108] Settle, F. A. *Handbook of Instrumental Techniques for Analytical Chemistry* (Prentice Hall, New Jersey, 1997).

[109] Cowley, R. A. The theory of Raman scattering from crystals. *Proceedings of the Physical Society* **84**, 281 (1964).

[110] Lewis, I. A. & Edwards, H. *Handbook of Raman Spectroscopy: From the Research Laboratory to the Process Line* (CRC Press, New York, 2001).

[111] Ruffell, S., Haberl, B., Koenig, S., Bradby, J. E. & Williams, J. S. Annealing of nanoindentation-induced high pressure crystalline phases created in crystalline and amorphous silicon. *Journal of Applied Physics* **105** (2009).

[112] Marinov, M. & Zotov, N. Model investigation of the Raman spectra of amorphous silicon. *Phys. Rev. B* **55**, 2938–2944 (1997).

[113] OriginPro. *version 9.0.0* (OriginLab Corporation, Northampton, 2013).

[114] Tsu, R., Paesler, M. A. & Sayers, D. Phonon linewidth and bond angle deviation in amorphous silicon and germanium. *Journal of Non-Crystalline Solids* **114, Part 1**, 199–201 (1989).

[115] Roorda, S., Poate, J. M., Jacobson, D. C., Dennis, B. S., Dierker, S. & Sinke, W. C. Raman study of de-relaxation and defects in amorphous silicon induced by MeV ion beams. *Applied Physics Letters* **56**, 2097–2099 (1990).

[116] Lucazeau, G. & Abello, L. Micro-Raman analysis of residual stresses and phase transformations in crystalline silicon under microindentation. *Journal of Materials Research* **12**, 2262–2273 (1997).

[117] Morell, G., Katiyar, R. S., Weisz, S. Z., Jia, H., Shinar, J. & Balberg, I. Raman study of the network disorder in sputtered and glow discharge a-Si:H films. *Journal of Applied Physics* **78**, 5120–5125 (1995).

[118] Gupta, S., Katiyar, R. S., Morell, G., Weisz, S. Z. & Balberg, I. The effect of hydrogen on the network disorder in hydrogenated amorphous silicon. *Applied Physics Letters* **75**, 2803–2805 (1999).

[119] Mort, J. & Knight, J. Localization and electronic properties in amorphous semiconductors. *Nature* **290**, 659–663 (1981).

[120] Adler, D. Defects in amorphous chalcogenides and silicon. *J. Phys. Colloques* **42**, C4–3–C4–14 (1981).

[121] Fedders, P. A. & Carlsson, A. E. Defect states at floating and dangling bonds in amorphous Si. *Phys. Rev. B* **37**, 8506–8508 (1988).

[122] Mott, N. F. & Davis, E. A. *Electronic Processes in Non-Crystalline Materials* (Clarendon Press, Oxford, 1970).

[123] Schroder, D. K. *Semiconductor Material and Device Characterization* (John Wiley & Sons, New York, 2006).

[124] Hohne, G., Hemminger, W. & Flammersheim, H. J. *Differential Scanning Calorimetry: An Introduction for Practitioners* (Springer-Verlag, Berlin, 1996).

[125] J, O. M. & S, W. E. Differential microcalorimeter (1966). US Patent 3,263,484.

[126] Haines, P. J., Reading, M. & W., W. F. *Differential Thermal Analysis and Differential Scanning Calorimetry.* Handbook of Thermal Analysis and Calorimetry (Elsevier Science B.V., 1998).

[127] Sinke, W. C., Roorda, S. & Saris, F. W. Variable strain energy in amorphous silicon. *Journal of Materials Research* **3**, 1201–1207 (1988).

[128] Tsu, R. Structural characterization of amorphous silicon and germanium. *Solar Cells* **21**, 19–24 (1987).

[129] Acco, S., Williamson, D. L., Stolk, P. A., Saris, F. W., van den Boogaard, M. J., Sinke, W. C., van der Weg, W. F., Roorda, S. & Zalm, P. C. Hydrogen solubility and network stability in amorphous silicon. *Phys. Rev. B* **53**, 4415–4427 (1996).

[130] Lucovsky, G., Jing, Z., Lu, Z., Lee, D. R. & Whitten, J. L. Properties of bonded hydrogen in hydrogenated amorphous silicon and other hydrogenated amorphous silicon alloys. *Journal of Non-Crystalline Solids* **182**, 90–102 (1995).

[131] Malley, N., Lannin, J. S. & Scott, B. A. Raman scattering studies in dilute and concentrated a-$Si_{1-x}H_x$ alloys. *Journal of Non-Crystalline Solid* **59**, 201–204 (1983).

[132] Yehoda, J. E. & Lannin, J. S. Trilayer Raman scattering of variably ordered amorphous Ge. *Journal of Vacuum Science and Technology A* **1**, 392–394 (1983).

[133] Haberl, B. *Structural characterization of amorphous silicon.* Ph.D. thesis, Australian National University (2011).

[134] Muller, G. & Krotz, G. Amorphous silicon technology. In *MRS Symposia Proceedings Vol. 297* (Pittsburgh, PA, USA, 1993).

[135] Gonzalez-Hernandez, J., Chao, S. S., Martin, D. & Tsu, R. Characterization of amorphous and polycrystalline Si and Ge films. *Proc. SPIE* **0524**, 126–136 (1985).

[136] Tsu, R., Gonzalez-Hernandez, J. & Pollak, F. H. Determination of the energy barrier for structural relaxation in amorphous Si and Ge by Raman scattering. *Solid State Communications* **54**, 447–450 (1985).

[137] Roth, J. A., Olson, G. L., Jacobson, D. C. & Poate, J. M. Kinetics of solid phase epitaxy in thick amorphous Si layers formed by MeV ion implantation. *Applied Physics Letters* **57**, 1340–1342 (1990).

[138] Treacy, M. M. J. & Gibson, J. M. Variable coherence microscopy: a rich source of structural information from disordered materials. *Acta Crystallographica Section A* **52**, 212–220 (1996).

[139] Ruffell, S., Bradby, J. E., Williams, J. S., Munoz-Paniagua, D., Tadayyon, S., Coatsworth, L. L. & Norton, P. R. Nanoindentation-induced phase transformations in silicon at elevated temperatures. *Nanotechnology* **20**, 135603 (2009).

[140] Ruffell, S., Vedi, J., Bradby, J. E. & Williams, J. S. Effect of hydrogen on nanoindentation-induced phase transformations in amorphous silicon. *Journal of Applied Physics* **106**, 123511–6 (2009).

[141] Follstaedt, D. M., Knapp, J. A. & Myers, S. M. Mechanical properties of ion-implanted amorphous silicon. *Journal of Materials Research* **19**, 338–346 (2004).

[142] Kailer, A., Gogotsi, Y. G. & Nickel, K. G. Phase transformations of silicon caused by contact loading. *Journal of Applied Physics* **81**, 3057–3063 (1997).

[143] Danesh, P., Pantchev, B., Wiezorek, J., Schmidt, B. & Grambole, D. Effect of hydrogen on hardness of amorphous silicon. *Applied Physics A* **102**, 131–135 (2011).

[144] Burrows, V. A., Chabal, Y. J., Higashi, G. S., Raghavachari, K. & Christman, S. B. Infrared spectroscopy of Si(111) surfaces after HF treatment: Hydrogen termination and surface morphology. *Applied Physics Letters* **53** (1988).

[145] Chabal, Y. J., Higashi, G. S., Raghavachari, K. & Burrows, V. A. Infrared spectroscopy of Si(111) and Si(100) surfaces after HF treatment: Hydrogen termination and surface morphology. *Journal of Vacuum Science and Technology A* **7** (1989).

[146] Huff, H. *Into The Nano Era* (Springer, 2008).

[147] Zhang, X., Garfunkel, E., Chabal, Y. J., Christman, S. B. & Chaban, E. E. Stability of HF-etched Si(100) surfaces in oxygen ambient. *Applied Physics Letters* **79**, 4051–4053 (2001).

[148] Perrine, K. A. & Teplyakov, A. V. Reactivity of selectively terminated single crystal silicon surfaces. *Chem. Soc. Rev.* **39**, 3256–3274 (2010).

[149] Mori, H., Adachi, S. & Takahashi, M. Optical properties of self-ion-implanted Si(100) studied by spectroscopic ellipsometry. *Journal of Applied Physics* **90**, 87–93 (2001).

[150] Zhang, T. Y. & Zhao, M. H. The role of plastic deformation of rough surfaces in the size-dependent hardness. *Acta Materialia* **52**, 57–68 (2004).

[151] Jiang, W. G., Su, J. J. & Feng, X. Q. Effect of surface roughness on nanoindentation test of thin films. *Engineering Fracture Mechanics* **75**, 4965–4972 (2008).

[152] Roorda, S., Martin, C., Droui, M., Chicoine, M., Kazimirov, A. & Kycia, S. Disentangling neighbors and extended range density oscillations in monatomic amorphous semiconductors. *Phys. Rev. Lett.* **108**, 255501 (2012).

[153] Beyer, W. & Stuke, J. *in Amorphous and Liquid Semiconductors, Proceedings of the Fifth International Conference on Amorphous and Liquid Semiconductors* (Taylor and Francis, London, 1974).

[154] Mott, N. F., Davis, E. A. & Street, R. A. States in the gap and recombination in amorphous semiconductors. *Philosophical Magazine* **32**, 961–996 (1975).

[155] Trumbore, F. A. Solid solubilities of impurity elements in germanium and silicon. *B. S. T. J.* **39**, 205–233 (1960).

[156] Olson, G. L. & Roth, J. A. Kinetics of solid phase crystallization in amorphous silicon. *Materials Science Reports* **3**, 1–77 (1988).

[157] Licoppe, C. & Nissim, Y. I. Impurity-induced enhancement of the growth rate of amorphized silicon during solid-phase epitaxy: A free-carrier effect. *Journal of Applied Physics* **59** (1986).

[158] Park, W. W., Becker, M. F. & Walser, R. M. Ionization-enhanced solid phase epitaxy of amorphous silicon with boron impurities. *Applied Physics Letters* **52** (1988).

[159] Gibbs, M. R. J., Evetts, J. E. & Leake, J. A. Activation energy spectra and relaxation in amorphous materials. *Journal of Materials Science* **18**, 278–288 (1983).

[160] Berntsen, A. J. M. *Structural disorder in pure and hydrogenated amorphous silicon.* Ph.D. thesis, Utrecht University (1993).

[161] Fritzsche, H. *Amorphous and Liquid Semiconductors* (Plenum Press, 1974).

[162] Mehra, R. M., Kumar, H., Koul, S. & Mathur, P. C. Thickness dependence of DC conductivity of amorphous Se and binary amorphous Se-Te, Se-Ge, and Se-Sb films. *physica status solidi (a)* **83**, 341–347 (1984).

[163] Lannin, J. S. Structural order and dynamics of amorphous silicon and germanium. *Journal of Non-Crystalline Solids* **97-98, Part 1**, 39–46 (1987).